DEVELOPMENT OF GREEN ELECTROLUMINESCENT TERBIUM DOPED ZINC
SULFIDE THIN FILM PHOSPHORS

By

JONGPYO KIM

A DISSERTATION PRESENTED TO THE GRADUATE SCHOOL
OF THE UNIVERSITY OF FLORIDA IN PARTIAL FULFILLMENT
OF THE REQUIREMENTS FOR THE DEGREE OF
DOCTOR OF PHILOSOPHY

UNIVERSITY OF FLORIDA

2001

ACKNOWLEDGMENTS

I appreciate my father, mother and sisters (Sujin and Hyungjin). They are always the biggest supporters of mine.

Finally I want to thank my wife, Anna, and my lovely daughter, Stephanie (Jeesu). I cannot express how much I love them by any words I can say.

TABLE OF CONTENTS

CHAPTERS

LIST OF FIGURES

DEVELOPMENT OF GREEN ELECTROLUMINESCENT TERBIUM DOPED ZINC
SULFIDE THIN FILM PHOSPHORS

By

Jongpyo Kim

December, 2001

Chairman: Dr. Paul H. Holloway
Major Department: Materials Science and Engineering

Alternating current thin film electroluminescent (ACTFEL) phosphors based on

ZnS:Tb were fabricated by R.F. magnetron sputtering. The brightness and efficiency of

the devices were improved by controlling deposition parameters such as target

configuration and sputtering gas composition, in addition to codoping using Ag, Cu and

Ce. By using a ZnS:TbOF single pressed power target, the brightness at 40V above

threshold (B_{40}) was improved to 89 cd/m^2 compared to 44 cd/m^2 for films deposited from

two separate ZnS and TbOF targets. This increase of brightness is attributed to improved

crystallinity due to reduced negative ion resputtering (NIR) effects from O$^-$ and F$^-$.

Sputter-deposition of ZnS:TbOF films using Ar + He mixture (the He gas concentration

was changed from 0% to 70%) also improved the crystallinity of deposited film.

However, the brightness of the device decreases from 64 cd/m^2 for films deposited with

pure Ar atmosphere to 45-54 cd/m^2 for 60-70% He gas concentrations. This brightness

decrease is attributed to an increased dielectric constant (from 12 for pure Ar to 17 at 70 % He) and decreased RMS surface roughness (from 6.7 nm for pure Ar to 4.3 nm at 70 % He). To investigate the effects of oxygen incorporation, ZnS:Tb,F films were deposited from a ZnS:TbF$_3$ target with an oxygen flow. ZnS:Tb,F films show the best brightness (82 cd/m^2) at 3.6 at. % of oxygen concentration in the deposited film, with a very sharp drop off in brightness from either underdoping (56 cd/m^2 at 2.2 at. % oxygen) or overdoping (42 cd/m^2 at 8.1 at. % oxygen). The brightness improvement by oxygen incorporation can be attributed to an increased conduction charge. The brightness decrease by oxygen overdoping is attributed to both a decreased excitation and a decreased radiative efficiency. After annealing at 500°C for 60 minutes, Ce codoping increases the B$_{40}$ to 144 cd/m^2 compared to 86 cd/m^2 of uncodoped ZnS:TbOF films. This brightness improvement is attributed to an increased radiative efficiency. At V$_{20}$, the radiative efficiency of Ce codoped films is improved by $\approx$ 130%. The non-linear exponential decay of the electroluminescent emission for Ce codoped films is attributed to an energy transfer from Ce^{+3} to Tb^{+3} luminescent centers. After annealing at 500°C for 60 minutes, Ag + Cu codoped ZnS:TbOF thin film phosphor also showed increased brightness at 20V above threshold, B$_{20}$ of 67 cd/m^2 compared to 55 cd/m^2 for uncodoped ZnS:TbOF films. The increased brightness for Cu +Ag codoped ZnS:TbOF film is attributed to increased surface roughness and improved excitation efficiency caused by space charge modification due to Ag^{+1} and Cu^{+1} codoping.

CHAPTER 1
INTRODUCTION

Thin film electroluminescent display devices have been investigated for flat panel displays and ZnS:Mn yellow light emitting alternating current thin film electroluminescent (ACTFEL) devices are commercially available [1-6]. Even though ACTFEL devices have many advantages such as ruggedness, high contrast, wide viewing angle and good temperature range, the performance of primary colors such as green and blue still need to be improved for multicolor and full color devices [7-12].

ZnS:Tb is the most promising green color display material because it has the highest reported brightness among the green color emitting phosphors [13, 14]. Even though ZnS:Tb showed the highest reported brightness ($100cd/m^2$ at 40 volts over threshold voltage: B_{40}) among the green color emitting phosphors, it still showed much poorer brightness than yellow emitting ZnS:Mn ($300cd/m^2$ at B_{40}) [15]. The limited solubility of Tb^{+3} ions in ZnS due to large ionic size of the Tb^{+3} ($0.92Å$) compared to Zn^{+2} ($0.74Å$) and point defect due to charge mismatch of Tb^{+3} and Zn^{+2} were thought to limit the brightness of ZnS:Tb green phosphor. In this study, a new approach to improve the performance of ZnS:Tb green color phosphor will be discussed.

Chapter 2 will present the background and literature review of ACTFEL device. In chapter 3, the experimental methods and characterization methods used in this study will be presented. In chapter 4 and chapter 5, the effect of the processing parameters such as target condition and sputtering gas composition will be studied. Chapter 6 will present

the effects of codoping elements such as Ag^{+1}, Cu^{+1} and Ce^{+3} and their roles in the ZnS:Tb phosphor. In chapter 7, the conclusion will be presented.

CHAPTER 2
LITERATURE REVIEW

2.1 Introduction

Electroluminescence (EL) is the phenomenon in which electrical energy is converted to luminous energy with minimal thermal energy generation. This effect was observed in 1929 by Gudden and Pohl [16] who experimented with the change of photoluminescent decay of a ZnS:Cu phosphor by an electric field. There are two different types of EL devices. One is light emitting diodes (LED) from which light is generated by electron-hole pair recombination. The second types are EL devices in which light is generated by impact excitation of a light-emitting center by high-energy electrons. In general light is emitting from these centers in a state-to-state transition, in contrast to a band edge recombination event. The focus of this review will be the second type of EL devices, which have particular advantages as flat panel display devices [15]. These EL devices are further categorized according to the phosphor configuration and the drive voltage waveform into ac thin film EL, ac powder EL, dc thin film EL and dc powder EL [15]. Among them, ac thin film EL (ACTFEL) devices are most widely used for flat panel displays.

In this chapter, fundamental information will be given about ACTFEL devices, such as device structure, ACTFEL device physics, materials requirements and characterization methods. Additionally, a literature review for ZnS:Tb green light emitting phosphor, which is the topic of this study, will be given. This includes a review

of general properties, charge compensation, excitation mechanism, and ZnS:Tb phosphor deposition methods.

2.2 ACTFEL Device Structures

2.2.1 Monochrome Structures

For ACTFEL display devices, a double insulator structure, which is called a MISIM (metal – insulator - semiconductor (phosphor) – insulator – metal) structure, is most widely used for ACTFEL device. Inoguchi et al. [17] first reported on high-luminance, long lifetime EL device using this double insulating layer structure. A typical MISIM structure for ACTFEL device is illustrated in Figure 2.1.
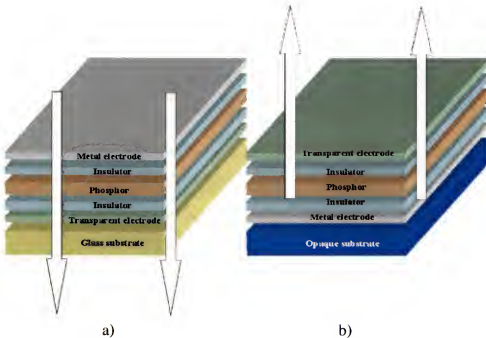
Figure 2.1 Typical structure of ACTFEL device, with a) conventional (light emitted through the substrate), or b) inverted structure.

Figure 2.1a shows the conventional device structure in which light is emitted through a transparent substrate, and figure 2.1b shows an inverted structure. The conventional structure consists of a metal electrode/top insulating layer /phosphor layer/bottom insulating layer/transparent electrode/glass substrate. The inverted structure consists of a transparent top electrode/top insulating layer/phosphor layer/bottom insulating layer/metal electrode/opaque substrate.

In the ACTFEL device, the phosphor layer in the center emits light when a large electric field is applied. The electric field is $\sim 10^8$ V/m. This high electric field can cause a short circuit at any defect in the phosphor and/or insulator layers, with a resulting catastrophic failure for the device. The thin film insulating layers are used as current limiting layers on both side of the phosphor layer to achieve a reliable device [15].

Conventional structure ACTFEL devices use transparent glass substrates and transparent bottom electrodes because light comes out through the bottom electrode and substrate. Glass substrates have the advantages of low cost and wide availability. However, some EL phosphors require a high post-annealing step to improve brightness and efficiency and low softening point glass limits the annealing temperature. The inverted structure makes it possible to use silicon substrates, which allows the drive electronics and the EL device to be manufactured on the same substrate [18]. Another advantage of the inverted structure is the use of color filters in multi-color or full color devices. In the conventional structure, color filter would need to be deposited before the phosphor layer. However, in the inverted structure, the color filter can be deposited on the top of the device after any high temperature post deposition annealing process [10]. However, the inverted structure loses the self-healing mechanism exhibited by Al

electrode. "Self-healing" means that any microscopic electrical breakdown in the phosphor layer does not propagate and lead to catastrophic failure because breakdown is limited to a very localized region by rapid fusing of the aluminum electrode by the high current flow from a short circuit [15].

Thick dielectric film EL (TDEL) devices also use the inverted structure [19]. TDEL devices use an opaque alumina substrate and thick screen-printed bottom dielectric layer as shown in figure 2.2. This structure may be cost efficient because it uses screen-printing instead of vacuum thin film deposition methods to form the bottom dielectric layer. Also the alumina substrate allows high temperature post-annealing processes. This device structure is adopted by iFire EL flat panel display devices [20].
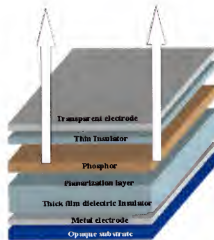
Figure 2.2 Typical TDEL structure.

2.2.2 Multicolor Structures

To achieve multicolor ACTFEL devices, many kinds of multicolor thin-film EL structure have been proposed and tested, but three types of thin film EL device structure

predominate [15]. They are stacked phosphor structure, patterned phosphor structure, and "color-by-white" filtered structures as shown in figure 2-3.

The stacked phosphor structure takes advantage of the transparency of the integrated layers in EL devices, and the light passing through another layer. This stacked structure has high resolution because it does not need to be separated into subpixels. In addition, stacked structure needs relatively simple lithographic patterning. However, stacked structure uses ITO electrode in the middle of the two insulators, which does not exhibit the "self-healing" ability of an Al electrode.
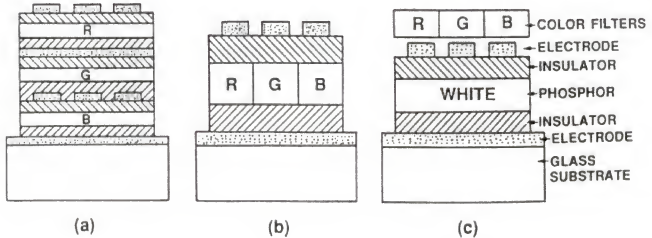
Figure 2.3 Schematic structure of multicolor thin film EL panels a) stacked phosphor structure b) patterned phosphor structure, and c) "color-by-white" filtered structure [15].

The patterned phosphor structure uses photolithographically patterned phosphor layers corresponding to three primary colors. Patterned structures can use the same drive circuitry as monochrome panels, which is simpler than for stacked structure. The deposition process is also simpler than for stacked structures. However, patterned structures have lower resolution and luminance because of smaller pixel fill factor.

"Color-by-white" filtered structures use color filters over a white-light-emitting phosphor having red, green and blue components. "Color-by-white" filtered structures have advantages such as no requirement for matching of the threshold voltages for multiple phosphors and simple device fabrication processes. However, it requires very high luminance, broad band phosphors.

2.3 Device Physics

Basic ACTFEL devices need a high electric field on the phosphor layer to generate transferred charge and to impact-excite or impact-ionize the luminescent centers [3, 21]. The EL emission process can be divided into several steps as shown in the schematic diagram in figure 2.4. Each step for EL emission is as follows:

1) Electron tunnel injection into the conduction band of the phosphor from phosphor/insulator interface states.

2) Tunnel-injected electrons are accelerated by high electric fields in the phosphor layer.

3) "Hot" electrons impact-excite or impact-ionize the luminescent centers.

4) Excited luminescent centers radiatively (photon generation) or non-radiatively (phonon generation) de-excite.

5) The generated photons escape from the thin film stack (are said to be "out coupled").

6) Electrons lose energy and are trapped at the phosphor/insulator anode interface.

7) The voltage is reversed and the process repeats itself.
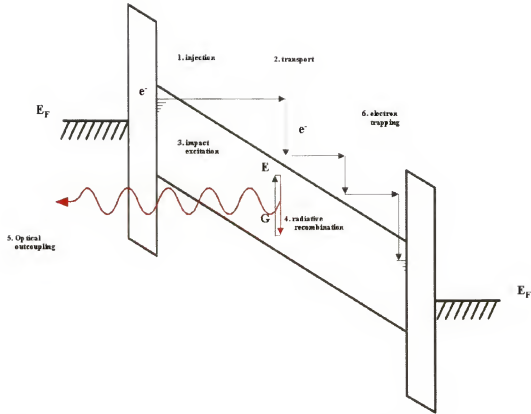
Figure 2.4 Schematic diagram for ACTFEL emission mechanism.

2.3.1 Electron Injection

In ACTFEL device, there are two possible carrier sources, i.e. bulk and the phosphor/insulator interface. However, it is generally accepted that electron injection in EL phosphors is dominated by tunneling from the interface [3, 21]. The important electronic characteristics at the interface are the trap depth and the density of energy states. The energy required to tunnel electrons out of the interface is controlled by the trap depth. If the trap depth is too deep, the EL device requires very high electric field. If the trap depth is too shallow, the electrons are ejected at low electric field and it is difficult to accelerate to high energy enough to impact excite the luminescent centers. It

is reported that the optimum trap depth is 1.0eV to 1.3eV [22]. The density of energy states is the number of energy states per unit energy. A high density of energy states is desirable for ACTFEL device.

There are two possible mechanisms for electron injection from phosphor/insulator interface by applied electric field [3]. One is thermionic emission and the second is tunneling. Thermionic emission occurs when the electron trapped at the interface obtains enough thermal energy to overcome the potential barrier. Therefore, thermionic emission is strongly temperature dependent. Tunneling is the quantum mechanical penetration of electron wave under sufficiently high electric field. Tunneling is not temperature dependent. However, a more accurate explanation for electron injection is the combination of thermionic emission and quantum mechanical tunneling, i.e. phonon-assisted tunneling [22] since the ACTFEL device current is reported to be slightly temperature dependent.

2.3.2 Charge Transport

The electrons injected from phosphor/insulator interface are accelerated by high electric field set up in phosphor layer with random collisions with luminescent centers. However, during transport, electron will experience inelastic scattering and energy loss. Therefore, it is important to understand how efficiently the electrons can be transported to excite the luminescent centers. There are currently two approaches to calculating this efficiency [15]. One is band-structure dependent and based on Monte Carlo simulation [23, 24] and the other is a "lucky-drift" model [25, 26].

The Monte Carlo method is a simulation of the trajectories of individual carriers as they move through a device under the influence of external forces subject to random

scattering events due to various electron-phonon interactions [15]. Brennan [27] performed an ensemble calculation by Monte Carlo simulation of steady-state hot electron transport in bulk ZnS. He concluded that very few carriers are available with sufficient energy to excite Mn luminescent centers in ZnS at a field of 10^8 V/m. This results can not explain the high luminescence and high luminous efficiency of ZnS:Mn EL device. Mach and Mueller et al. [23] used the assumption of parabolic conduction band and polar optical phonon scattering in Monte Carlo simulation. They concluded that electrons in ZnS thin film EL devices undergo ballistic or loss-free transport. This result is contrary to Brennan's result and neither simulations agree with experimental results. Bhattacharyya et al. [28] assumed a non-parabolic multivalley model for Monte Carlo simulation and this model gave steady-state electron energy distributions in reasonable agreement with experiment.

The lucky drift model uses the basic transport modes. The first is the ballistic mode, which is collision free and occurs before the electron's first collision. The other is the drift mode, which occurs after the electron experiences the first collision. After the first collision, the electron will be deflected and the probability of the other collisions is greatly increased. Bringuier [25] simulated the impact excitation luminescence in ZnS:Mn using this lucky drift model. These simulations using a Monte Carlo model combined with the lucky drift model helped the understanding of high field electron transport. However, the exact description of the electron acceleration by high electric field remains uncertain.

2.3.3 Impact Excitation and Ionization

After electrons are accelerated to sufficiently high energy, they can interact with luminescent centers to excite them from the ground state to excited state. There are several suggested excitation mechanisms. First is the direct impact excitation mechanism. It is considered to be a primary process in excitation of ZnS:Mn [29] or ZnS:Tb [30]. In this process, the intrashell emission of the luminescent center is excited by the impact of hot electrons [21]. Therefore, the process of impact excitation is treated as inelastic scattering of hot electron at the luminescent site. The probability of this process is determined by the impact cross section of the luminescent center. In the case of a rare earth (RE) luminescent centers like Tb, the impact cross section is the product of three factors, i.e. the screening of the RE ions from the hot electrons by the valence electrons, the inverse of the excitation energy, and the electric dipole excitation transition rate for the ion [21]. For RE activated materials, the electric dipole excitation transition rate is low because most of the RE ions have intrashell transitions in $4f$ shells, which is a parity-forbidden process, except for the small electric dipole transition rate. The parity selection rule is that the electric dipole transitions between levels with same parity, such as within the d shell and within the f shell, is forbidden. However, low symmetry electric field at the luminescent site may result in admixing of higher state ($4f^{n-1}5d^1$, $3d^{n-1}4s^1$) of the opposite parity to the ground state [31]. This breaks the selection rule and increases the probability of the excitation and de-excitation. Figure 2.5 presents a substantial fraction of the energy levels originating from the $4f^n$ configuration.

The second process is an indirect excitation mechanism. This is a multistep process involving first the excitation of another center that does not luminescence. The luminescent centers are excited by transfer of energy from the initially excited centers to

the luminescent centers. Energy can be transferred from an excited donor-acceptor pair
(DAP) or exciton state to the luminescent center.

Figure 2.5 Energy band levels of the $4f^n$ configurations of the trivalent lanthanide ions.
The thickness of the line indicates the predicted crystal field splitting of the different
energy levels [31].

The third excitation process is impact ionization. In this scheme, the luminescent center is ionized by the impact of hot electrons, and then an electron is recaptured in the excited state of the ionized luminescent center. Recapture is followed by radiative relaxation to the ground state. The impact ionization cross-sections are expected to be two to four orders of magnitude larger than those for the impact excitation mechanism [32]. It is reported that Pr doped sulfide [33, 34] and Eu doped sulfide [35] can change their oxidation state during excitation, which means that impact ionization mechanism is feasible.

2.3.4 Radiative Decay

There are several possible ways of returning the excited luminescent centers to ground state. The first is radiative relaxation. The second is the nonradiative relaxation, which is radiationless energy dissipation to crystal lattice. The third possible path of returning to ground state is transfer of the excitation energy from one ion to another. In the application to display devices, the radiative relaxation should be maximized and the nonradiative relaxation should be reduced to achieve high light output.

For the two-level system, the population of the excitation state decreases according to

$$\frac{dN_e}{dt} = -N_e P_{eg} \qquad (2\text{-}1)$$

where N_e gives the number of luminescent ions in the excited state after an excitation pulse, t is the time and P_{eg} is the probability for spontaneous emission from the excited to the ground state [31]. By integration

$$N_e(t) = N_e(0)\exp(-\frac{t}{\tau_R}) \qquad (2\text{-}2)$$

where $\tau_R \ (= P_{eg}^{-1})$ is the radiative decay time.

The lifetime of the excited state depends on whether the emission is allowed or forbidden. For allowed emission transitions, the lifetime may be as short as $10^{-7} - 10^{-8}$ sec. For strongly forbidden transitions, it is much longer at $\approx 10^{-3}$ sec.

Some RE ions, such as Gd^{+3}, Eu^{+3}, Tb^{+3}, Sm^{+3} and Dy^{+3}, have emission transition within $4f$ band where the parity does not change. Therefore, they have sharp emission lines in the spectra and long excited state lifetimes. However, several RE ions such as Ce^{+3} and Pr^{+3} have transitions between $5d$ orbitals and $4f$ orbitals. This $5d\rightarrow4f$ transition is parity allowed, broad emission band and short life time as a few tens of nanosecond [31].

2.3.5 Optical Outcoupling

Another important factor that affects the final luminescence in the direction of viewer is the light-trapping effect at the interface between the two different media with different optical indices. In the conventional EL device structure, the light generated in the phosphor layer meets several interfaces as shown in figure 2.6. Specifically, when light travelling in media 1 strikes the interface with media 2 at an angle θ_1, the light is refracted according to Snell's law

$$n_1\sin\theta_1 = n_2\sin\theta_2 \qquad (2\text{-}3)$$

where n_1 and n_2 are the indexes of refraction for each media and the θ_1 is the angle of the incidence light and θ_2 is the angle at which the light refracts. When medium 1 has a

higher index of refraction than medium 2, incident light from medium 1 onto the

interface is totally reflected above a critical angle (θ_C) defined by

$$\theta_C = \sin^{-1}(n_2/n_1) \qquad (2\text{-}4)$$

Typically, in the case of ZnS:Mn ACTFEL device, the index of the refraction of

phosphor layer is ~2.3, which is larger than the insulator layer such as Al_2O_3 (n=1.63) or

SiO_2 (n=1.46). Further, the refractive index of glass is 1.53, which is larger than the

refractive index of air (n=1.0). Therefore, a large part of the EL emissions from phosphor

layer cannot go through the glass substrate into air and instead is trapped in the EL device

by total reflection. The optical out-coupling efficiency (η_{opt}) can be estimated for smooth

surface by assuming that the index of refraction of the ZnS phosphor layer is 2.3 and light

is reflected at the rear metal electrode as follows:

$$\eta_{opt} = \int_0^{\arcsin(1/2.3)} \sin\theta \, d\theta = 1 - [1 - (1/2.3)^2]^{0.5} \approx 0.1 \qquad (2\text{-}5)$$

The optical out-coupling efficiency (η_{opt}) can be improved by an increase of

surface roughness which reduces internal reflection. However, the rough surface also

reduces the contrast ratio by increased diffuse scattering and may lead to increased

dielectric breakdown.
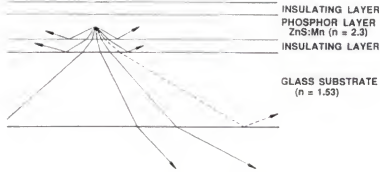
Figure 2.6 Schematic representation of internal reflection in ACTFEL devices [15].

2.4 Materials Requirement for ACTFEL Devices

In this section, the physical, optical and electrical characteristics of the substrate, dielectric layer, phosphor layer and electrode materials for ACTFEL devices will be reviewed.

2.4.1 Substrates

The requirement for the substrate depends on the device structure. In the conventional structure, the substrate should be transparent to the emitted (visible) light. In EL device fabrication, the device is exposed to high temperature annealing (~ 550 °C) to improve the brightness and stability. Therefore, the substrate should have high softening temperature and the thermal expansion coefficients of the substrate and deposited film should be matched to reduce stress during cooling from heat treatment temperatures. In addition, the substrate should have low or no alkali metal content because the diffusion of alkali-metal ions into the phosphor layer may deteriorate light emission property of

phosphor layer. For these reasons, Corning 7059 glass is used widely for conventional ACTFEL devices. It is a non-alkaline, phosphosilicate glass that has relatively high softening point of ≈ 600°C.

For inverted ACTFEL devices, silicon wafer or ceramic substrates such as alumina (Al_2O_3) are used. As mentioned in section 2.2, silicon substrates have the advantage of making possible the fabrication of the EL drivers on the same substrate. Ceramic substrates such as alumina have the advantage of high processing temperatures. However, ceramic substrate may need a planarization process to reduce the surface roughness.

2.4.2 Electrodes

The bottom electrode of conventional and the top electrode of inverted devices should have high transmittance in the visible light region in addition to high conductivity. The commonly used electrode for this application is indium-tin oxide (ITO : 90wt% In_2O_3 – 10wt% SnO_2). The typical sheet resistance of the ITO thin film is 5 – 10 $\Omega/$ and the resistivity is ~ $10^{-4}\Omega$cm. indium-tin oxide (ITO) has high conductivity because of a high concentration of shallow donors that lie only a few meV below the conduction band [3]. At room temperature, these donors are thermally activated into the conduction band and lead to high conductivity. There are two sources for these shallow donors, namely Sn^{+4} ion substituting the In^{+3} site and oxygen deficiencies. Another transparent electrode material is ZnO and ZnO:Al, In, Ga. The conduction mechanism of ZnO films is similar to that of ITO. For undoped ZnO, oxygen vacancies act as a shallow donor level, and for

doped ZnO, Al, In and Ga have +3 valence state and act as shallow donor when they substitute on the Zn^{+2} site [36].

The top electrode in conventional and bottom electrode in inverted structure does not need to be transparent. Therefore, generally metal films are used for these electrodes and have several typical requirements for ACTFEL devices [15]. First, they should have low resistivity. Common metal electrodes have lower resistivity than transparent electrode. Second, they should have good adhesion and wettability to the insulating layer. Third, they should be resistant to electromigration under high electric field. Aluminum (Al) ~200nm thick is typically used in conventional devices to satisfy these conditions. In addition, it is inexpensive and easy to deposit. . One drawback of aluminum electrodes is their high reflectivity which allows external light which is incident on the ACTFEL device to be reflected back and reduce the contrast. This can be suppressed with filters. On the other hand, the metal electrode for the inverted structure has additional requirements. First, resistance to changes during annealing is required because the device may need to be heated to above 550°C. Second, the thermal expansion coefficient should match the substrate. Therefore, refractory metals such as molybdenum (Mo) and tungsten (W) are suitable for metal electrode for inverted devices.

2.4.3 Insulators

The insulating layer in ACTFEL device plays an important role in protecting the phosphor layer from electric breakdown from fields of $>2 \times 10^{-8}$ V/m [15]. Therefore, the insulating layer should have high dielectric breakdown electric fields (E_{BD}) and be producible with zero pinholes and defects. The bottom-insulating layer is exposed to the

high temperature annealing process after the phosphor layer deposition. Therefore, it should be thermally and chemically stable at high temperatures with good adhesion. In addition, the dielectric constant ($\varepsilon_0 \varepsilon_r$: ε_0 and ε_r are the dielectric constant of vacuum and relative dielectric constant of insulator, respectively) is also important. The total electric field on the ACTFEL device is divided into the electric field in the phosphor layer and the electric field in the insulator layers. The fraction of the field across the phosphor is related to the capacitance of each layer as will be discussed below in section 2.6 2. The capacitance of the phosphor layer is determined as follows:

$$C = \varepsilon_0 \varepsilon_r \frac{A}{d} \qquad (2\text{-}6)$$

where A is area and d is thickness of the film. To increase the proportional of the voltage dropped across the phosphor layer, the capacitance of the insulator layer should be maximized. Therefore the dielectric constant of the insulating layer should be maximized and the thickness should be minimized to the extent that device reliability will allow.

Table 2.1 The relative dielectric constant (ε_r), breakdown field strength (E_{BD}), Figure of Merit defined by $\varepsilon_0\varepsilon_r E_{BD}$ (=the maximum trapped charge density), and breakdown mode of various insulating materials [15].

Material	Deposition Method*	ε_r	E_{BD} (10^8 V/m)	$\varepsilon_0\varepsilon_r E_{BD}$ ($\mu C/cm^2$)	Breakdown Mode**
SiO_2	Sputtering	4	6	2	SHB
SiON	Sputtering	6	7	4	SHB
SiON	PCVD	6	7	4	SHB
Al_2O_3	Sputtering	8	5	3.5	SHB
Al_2O_3	ALE	8	8	6	SHB
Si_3N_4	Sputtering	8	6-8	4-6	SHB
SiAlON	Sputtering	8	8-9	5-6	SHB
Y_2O_3	EBE	12	3-5	3-5	SHB
Y_2O_3	Sputtering	12	3-5	3-5	SHB
$BaTiO_3$	Sputtering	14	3.3	4	SHB
Sm_2O_3	EBE	15	2-4	3-5	SHB
$Ta_2O_5\text{-}TiO_2$	ALE	20	7	12	SHB
$BaTa_2O_6$	Sputtering	22	3.5	7	SHB
Ta_2O_5	Sputtering	23-25	1.5-3	3-7	SHB
$PbNb_2O_6$	Sputtering	41	1.5	5	SHB
TiO_2	ALE	60	0.2	1	PB
$Sr(Zr, Ti)O_3$	Sputtering	100	3	26	PB
$SrTiO_3$	Sputtering	140	1.5-2	19-25	PB
$PbTiO_3$	Sputtering	150	0.5	7	PB

*EBE : Electron beam evaporation, ALE : Atomic layer epitaxy
 PCVD : Plasma excited chemical vapor deposition
**SHB : Self-healing breakdown mode, PB : Propagating breakdown mode

Table 2.1 lists the relative dielectric constant (ε_r), breakdown field strength (E_{BD}), a Figure of Merit defined by $\varepsilon_0\varepsilon_r E_{BD}$ (which is equal to the maximum trapped charge density), and the breakdown mode for a variety of insulating materials as summarized by Ono [15]. Generally, amorphous oxides and nitrides such as Al_2O_3, SiO_2, Si_3N_4 and Y_2O_3 have small dielectric constants and high breakdown fields, while ferroelectric materials such as $BaTiO_3$ and $PbTiO_3$ have large dielectric constants and low breakdown fields. In addition, high dielectric constant materials such as $SrTiO_3$, $PbTiO_3$ exhibit a propagating breakdown mode that leads to catastrophic failure from small defects. Therefore, the dielectric materials are selected by a tradeoff of dielectric constant and breakdown

voltage. In addition, the self-healing breakdown mode should be chosen in insulating materials for ACTFEL devices.

<u>2.4.4 Phosphors</u>

Phosphor materials consist of a host material and luminescent centers. The light emission is from radiative relaxation to the ground state at the luminescent centers in the host. To get high luminescence and efficiency from phosphor film, there are several general requirements for host and luminescent materials.

<u>2.4.4.1 Host materials</u>

First, the host materials in phosphor should have a large enough band gap to emit visible light from the doped luminescent centers without significant absorption. This band gap should be at least 3.1eV for blue emission. Second, the host should have a high breakdown field, e.g. 10^8V/m. Below the breakdown field, the host must have insulating characteristics and after breakdown, the host materials should have good high field transport properties. Therefore, the host should have good crystallinity and a low phonon-coupling coefficient. Third, the host material should be stable at high post-annealing temperatures, e.g. 550-800°C. To date, the wide band gap II – VI semiconductors such as ZnS, CaS and SrS and alkaline-earth thiogallates ($CaGa_2O_4$, $SrGa_2O_4$ and $BaGa_2O_4$) [1-3, 15] satisfy these requirements. The basic properties of sulfides are given at Table 2.2. Among the many sulfide materials, ZnS and SrS are commercially used for ACTFEL devices. ZnS is the host materials for Tb green emitting luminescent centers in this study. In equilibrium, ZnS has the cubic zinc blende crystal structure at low temperature and

hexagonal wurtzite structure at temperature above 1024°C. The direct band gap of cubic

ZnS is 3.6 eV, which is wide enough to pass all the visual spectrum of light.

Table 2.2 The basic properties of sulfide hosts [15].

Item	IIb-VIb compound	IIa-VIb compound	
Materials	ZnS	CaS	SrS
Melting Point (°C)	1800-1900	2400	>2000
Band gap (eV)	3.6	4.4	4.3
Transition type	Direct	Indirect	Indirect
Crystal structure	Cubic zinc blende or Hexagonal wurtzite	Rock salt (NaCl type)	Rock salt (NaCl type)
Dielectric constant	8.3	9.3	9.4
Lattice constant (Å)	5.409	5.697	6.019
Ionic radius (Å)	0.74	0.99	1.13
Ionicity	0.623	>0.785	>0.785

Oxide or oxysulfide host materials used for cathode-ray tube (CRT) phosphor

have some limitations as host materials for ACTFEL phosphor. First, oxide host materials

have relatively large band gap (> 4.5 eV) and this large band gap limits the current

density of hot electrons. In addition, oxide phosphors need a higher temperature anneal

(>1000°C) to achieve acceptable crystallinity for charge transfer. A glass substrate limits

the annealing temperature to below the value where oxide host materials achieve good

crystallinity. Recently ACTFEL device using oxide host materials with moderate band

gaps, e.g. Ga_2O_3 (4.52 – 4.84 eV [37, 38]), $ZnGa_2O_4$ (~4.3 eV [39]), and Zn_2GeO_4:Mn

(4.68eV, [40]), have been studied. A refractory substrate material was used with high

temperature annealing to improve the crystallinity. Despite excellent thermal and

chemical stability, the brightness and efficiency of oxide phosphor have not been high

enough to compete with sulfide based phosphor materials.

2.4.4.2 Luminescent centers

While the host materials dominate the general electrical property of the phosphor, the luminescent centers dominate the optical properties. Luminescent centers can be categorized into two groups according to the their emission mechanism, such as donor-acceptor recombination. For example, ZnS phosphor doped with some combination of with Ag, Cu and Au, which are p-type, and Al and Cl, which are n-type, gives luminescence from the recombination of electrons and holes trapped in the deep donor and deep acceptor levels. However, these types of luminescent centers are not stable in ACTFEL device because electrons and holes in shallow acceptor and donor centers easily tunnel out of the levels under high electric field and are swept to the anode electrode.

Another type of the luminescent centers radiates from a relaxation between localized atomic quantum states. The luminescent centers in ACTFEL device are in this category. Transition metals such as Mn^{+2}, Cr^{+2}, Ti^{+4}, Cu^{+1} and Ag^{+1}, and rare earth ions such as Eu^{+3}, Ce^{+3}, Tb^{+3}, Tm^{+3} and Er^{+3} are suitable luminescent centers in ACTFEL device because they can form localized deep electronic state in some host materials. The general emission characteristics of these luminescent centers can be categorized by the electronic configuration of the ground and excited states. The possible transitions between the ground state and excited state are governed by selection rules. One of the rules is the spin selection rule, which forbids electronic transitions between quantum levels with different spin states. Another selection rule is the parity selection rule, mentioned earlier, which forbids electronic transitions between levels with the same parity, e.g. transitions only within the d or f shells, and between the d and s shells.

Transition metal ions have an incompletely filled d shell. Their electron configuration is d^n (0<n<10). Therefore, the radiative transitions on transition metal ions

are parity forbidden because all emission spectra are intra-shell d - d transition. However, the parity selection rule can be relaxed by coupling of the electronic transition with vibrations of suitable symmetry [21]. Also in tetrahedral coordination, the center of symmetry is lacking and the parity selection rule is relaxed by mixing small amounts of opposite-parity wave functions into the d wave functions [21].

As mentioned at section 2.3.3, the rare earth ions have incompletely filled $4f$ shell. The $4f$ orbital lies inside the quantum orbitals of the higher energy $5s^2$ and $5p^6$ valence electrons, and are therefore shielded from their surroundings. These rare earth ions can be divided further into two groups according to the transition characteristics. Intra-shell $4f$ - $4f$ transitions are observed in most trivalent rare earth ions such as Tb^{+3} and Eu^{+3}. These transitions are parity forbidden. Even though this intra-shell $4f$ - $4f$ transition is shielded by the outer electron orbitals, uneven components of the crystal field are still present when the rare earth ions occupies a crystallographic site. These uneven components mix small amount of opposite-parity wave functions ($5d$) into the $4f$ wave functions and result in significant oscillator strength. These spectra show narrow transition lines because they are insensitive to the surroundings and the decay time is typically of several milliseconds because they are parity forbidden.

Another type of emission transition in rare earth ions is $4f$ - $5d$ transition. In luminescent centers such as Ce^{+3} and Eu^{+2}, the electronic configuration in the ground state is $4f$. However, electrons can occupy the $5d$ state in the excited state. Therefore, this transition is parity allowed. The decay time of Ce^{+3}, which is spin allowed, is a few tens of nanoseconds, and the decay time of Eu^{+2}, which is spin forbidden, is several microseconds. When the transition is from a $5d$ state, the emission spectrum is affected

by the surrounding atoms and their symmetry. For example, Ce^{+3} emission ranges from ultra-violet to green depending upon the host materials [41].

2.4.4.3 Luminescent centers and host materials interactions

In addition to the electronic state modification of luminescent centers by the surrounding atoms and their symmetry, effective doping of luminescent centers into host materials requires compatibility with each other. For the luminescent centers to be active in the host material, they should dissolve in significant quantities either substitutionally or interstitially into the lattice without introduction of defects which can act as scattering centers for hot electrons, or act as nonradiative centers. Large ion size differences and valence mismatch between the luminescent center and host materials create difficulties for uniform incorporation into the lattice at the high concentrations required ($\approx 10^{21}$ cm^{-3}). To overcome this difficulty, charge compensators [42] or different deposition methods can be used [43,44]. Table 2.3 summarizes the optical properties of the most common sulfide-based EL materials and the ionic radii of host and luminescent materials are compared in Table 2.4.

2.5 Device Characterization of EL Devices

2.5.1 Optical Characterizations

The luminescence of ACTFEL device is strongly dependent on the applied voltage characteristics such as drive voltage, wave or pulse form, and frequency [15]. Therefore, these conditions should be explicitly mentioned when comparing the luminance. Generally used waveforms are sinusoidal waves or square pulses of alternate

polarity with a frequency of 60 Hz or 1kHz. The voltage pulse should be specified in zero to peak values, rather than RMS (root mean square) value. When square pulse waves of alternating polarity are used, the pulse width is defined by the full width at the half maximum of the actual pulse drive wave form and the rise time and fall time are defined by the time period corresponding to 10% - 90% value and 90% - 10% value of the actual voltage as shown in figure 2.7. The important optical parameters of ACTFEL device are luminance as a function of voltage, threshold voltage, CIE color coordinates and luminous efficiency [15].

Table 2.3 Optical properties of the most common sulfide-based EL phosphors [13].

Phosphor layer material	Emission color	CIE color Coordinates		Luminance L (cd/m^2)		Luminous efficiency η(lm/W) (1 kHz)
		X	Y	1 kHz	60 Hz	
ZnS:Mn	Yellow	0.5	0.5	5000	300	2-4
ZnS:Sm,F	Reddish-orange	0.60	0.38	120	8	0.05
ZnS:Sm,Cl	Red	0.64	0.35	200	12	0.08
CaS:Eu	Red	0.68	0.31	200	12	0.05
ZnS:Mn/Filter	Red	0.65	0.35	1250	75	0.8
ZnS:Tb,F	Green	0.32	0.60	2100	125	0.5-1
ZnS:Mn/Filter	Yellow-green	0.45	0.55	1300	80	-
Cas:Ce	Green	0.27	0.52	150	10	0.1
ZnS:Tm,F	Blue	0.11	0.09	2	<1	<0.01
SrS:Ce	Blue-green	0.19	0.38	900	65	0.44
ZnS/SrS:Ce	Bluish-green	0.26	0.47	1500	96	1.3
ZnS/SrS:Ce/Filter	Greenish-blue	0.10	0.26	220	14	0.2
CaGa$_2$S$_4$:Ce	Blue	0.15	0.19	210	13	-
SrS:Ce,Eu	Eggshell-white	0.41	0.39	540	32	0.4
SrS:Ce/CaS:Eu	Paper-White	0.35	0.36	280	17	-
ZnS:Mn/SrS:Ce	Yellowish-white	0.42	0.48	2450	225	1.3

Table 2.4 The ionic radii of host and luminescent materials [15].

Ion	Radius (Å)	Ion	Radius (Å)	Ion	Radius (Å)
Zn^{+2}	0.74	Mn^{+2}	0.80	Eu^{+2}	1.09
Ca^{+2}	0.99	Ce^{+2}	1.034	Tb^{+3}	0.923
Sr^{+2}	1.13	Sm^{+2}	0.964	Tm^{+3}	0.869
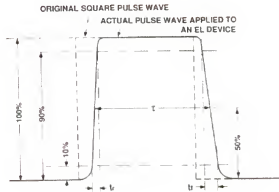
Figure 2.7 Definition of pulse width τ, rise time τ_r and fall time τ_f of the actual waveform [15].

2.5.1.1 Luminance

Electromagnetic radiation can be detected by the human eye over the range of 410nm to 720nm. Therefore, to characterize light, photometric values based on the luminous flux (Φ_v) are used rather than a radiometric values based on the radiant flux (Φ_e). The photometric value is the radiometric value convoluted with the eye sensitivity

factor. The relationship between the luminous flux (Φ_v) and the radiant flux (Φ_e) is expressed using the standard spectral luminous efficiency, $V(\lambda)$, where λ is wavelength, as follows:

$$\Phi_v = K_m \int \Phi_e(\lambda) V(\lambda) d\lambda = K \Phi_e \qquad (2\text{-}7)$$

where $\Phi_e(\lambda)$ is the spectral density of the radiant flux in the range of wavelengths from λ to $\lambda + \Delta\lambda$, and K_m (=680 lm/W) is the maximum spectral luminous efficiency in photopic vision [45] indicating the average luminous efficiency over the wavelength range. Figure 2.8 shows the standard spectral luminous efficiency curves for photopic vision under bright environment and scotopic vision under dark environment. Normally the photopic vision is used for standard luminous efficiency for evaluation of display devices.
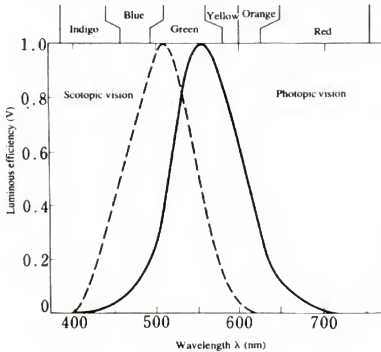
Figure 2.8 The standard spectral luminous efficiency curves for photopic and scotopic vision [45].

Luminance is generally the measure of the strength of light emitted by an active display device, and photometric terms indicate the radiated power in terms of the human eye sensitivity, while brightness is generally used in the case of a passive display. In some literature, luminance and brightness are not distinguished and used with the same meaning. The physical measure of luminance is luminous intensity per unit area, generally cd/m^2. Another frequently used unit is fL (foot-Lambert) defined by

$$1\,fL = \frac{1}{\pi} \times \frac{cd}{(ft)^2} = 3.426\,cd\,/\,m^2. \qquad (2\text{-}8)$$

The device luminance is generally measured as function of the peak voltage of the applied pulse and frequently compared at 40V above threshold voltage (L_{40}).

2.5.1.2 Threshold voltage (V_{th})

Threshold voltage is dependent on the dielectric property and thickness of the insulator and phosphor materials. There are several ways to define the threshold voltage of ACTFEL device. The first common method is to extrapolate the highest slope of L-V curve back to the voltage axis, and the intercept is the threshold voltage (V_{th}). The second method is to define the threshold voltage as that voltage corresponding to a luminance of 1cd/m^2. A third way is to define the threshold voltage from the electrical turn-on of the charge transfer versus a voltage (Q-V) curve. In this study, the threshold voltage will be defined by the voltage of the intercept of the highest slope of the L-V curve onto the voltage axis (first method).

2.5.1.3 CIE color coordinates

The CIE (Commission Internationale de l'Eclairage) colorimetric system is a standard of colorimetry which represent the attributes of color in a three dimensional diagram [45]. This CIE coordinates system uses three values (x, y, z) to represent color. This diagram can be plotted on a two-dimensional graph by the relationship of x + y + z = 1. The CIE system uses three idealized primary parameters (x(λ), y(λ), z(λ)) which are not monochromatic as shown in figure 2.9. The x, y and z in the figure 2.9 show the spectral tristimulus value used in CIE standard system. In the CIE colorimetric system, the tristimulus values X, Y, Z of the color of a light source can be expressed as:

$$X = K_m \int_{380}^{780} \Phi_{e\lambda} x(\lambda) d\lambda \qquad (2\text{-}9)$$

$$Y = K_m \int_{380}^{780} \Phi_{e\lambda} x(\lambda) d\lambda \qquad (2\text{-}10)$$

$$Z = K_m \int_{380}^{780} \Phi_{e\lambda} x(\lambda) d\lambda \qquad (2\text{-}11)$$

where K_m is 680 lm/W, $\Phi_{e\lambda}$ is the spectral output of the source, λ is wavelength and x(λ), y(λ), z(λ) are isochromatic functions of the CIE standard colorimetric system as shown in figure 2.9. The x, y, z coordinates in the CIE colorimetric system are calculated by:

$$x = \frac{X}{X + Y + Z} \qquad (2\text{-}12)$$

$$y = \frac{Y}{X + Y + Z} \qquad (2\text{-}13)$$

$$z = \frac{Z}{X + Y + Z}. \qquad (2\text{-}14)$$

The standard CIE chromaticity diagram using the x and y two-dimensional projection is given in figure 2.10.
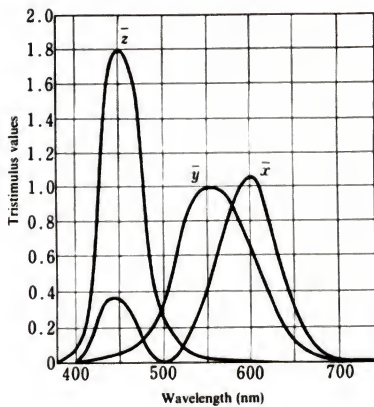
Figure 2.9 Isochromatic functions for the CIE standard colorimetric system [45].
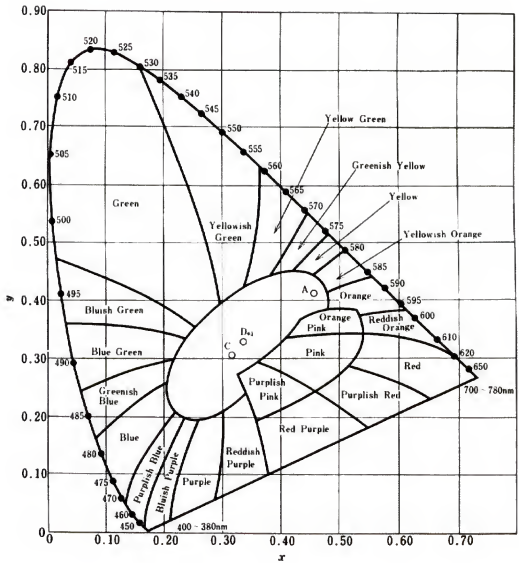
Figure 2.10 CIE xy chromaticity diagram [45].

2.5.1.4 Device efficiency

There are two methods to define the device efficiency. One is the measure of

luminance (lm/m^2) per input power density (W/m^2) consumed in the device. The

luminous efficiency can be given as follows under the assumption of a perfectly diffuse EL emission surface:

$$\eta[lm/W] = \pi \times \frac{L[cd/m^2]}{P_{in}[W/m^2]} . \tag{2-15}$$

The efficiency of individual phosphor is shown in Table 2.1. For ACTFEL devices, it is in the range of $0.3 - 1.5 \ lm/$W [15].

The other definition of device efficiency includes the concept of physical processes of electroluminescent device and is given by Mach et al. [46] as follows:

$$\eta = \frac{\text{photon flux} \ [\frac{\text{photons}}{\text{cm}^2\text{s}}]}{\text{transferred charge}[\frac{\text{electrons}}{\text{cm}^2\text{s}}]} . \tag{2-16}$$

This efficiency of device can be separated into several components as follows:

$$\eta = \eta_{exc}\eta_{lum}\eta_{opt} \tag{2-17}$$

where each term is involved in the main processes of the electroluminescent mechanism. η_{exc} is the efficiency of impact excitation of centers by ballistic electrons and given by

$$\eta_{exc} = \frac{\text{centers excited (cm}^{-3})}{\text{electron transfered (cm}^{-2})} . \tag{2-18}$$

Even though the measurement of the excitation efficiency of an EL device is not straightforward, the relative excitation efficiency can be measured by the procedure given by Zeinert et al. [47, 48]. By assuming that the initial brightness of a phosphor after an

excitation pulse that is much shorter than the decay time is proportional to the number of the excited states generated during that pulse, the following relationship is given :

$$\eta_{exc} = \frac{\text{concentration of excited centers}}{\text{numbers of electrons transported}} \propto \frac{B_{max}}{Q_{int}} . \qquad (2\text{-}19)$$

η_{lum} is the radiative efficiency of the excited centers and given by

$$\eta_{lum} = \frac{\text{centers decaying radiatively (cm}^{-3})}{\text{centers excited (cm}^{-3})} . \qquad (2\text{-}20)$$

η_{opt} is the outcoupling efficiency of the photons emitted from the phosphor layer and given by

$$\eta_{opt} = \frac{\text{photons emitted through the surface (cm}^{-3})}{\text{photons generated (cm}^{-3})} \qquad (2\text{-}21)$$

where "photons generated" are equal to "centers decaying radiatively" and therefore, the product of these three separate efficiencies will be overall efficiency, η. The excitation efficiency (η_{exc}) and outcoupling efficiency (η_{opt}) are affected by the thickness of phosphor layer. The thickness of films in this study is constant to $\pm 10\%$. Therefore the thickness effect will be ignored in the following discussions.

2.5.2 Electrical Characterizations

2.5.2.1 Circuit model of ACTFEL device

It is necessary to understand the electrical model in order to interpret the electrical characteristics of the ACTFEL device. As described in section 2.2, the typical ACTFEL device has the double insulating layer structure and the phosphor layer is sandwiched between the two insulating layers. Therefore in an early model by Smith [49], the
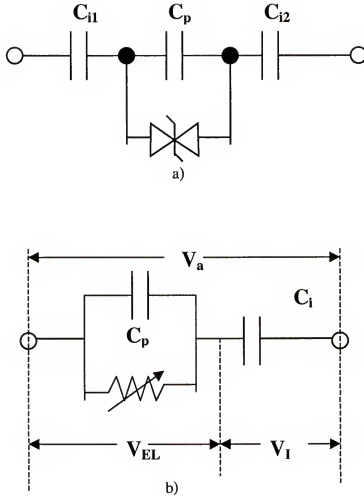
Figure 2.11 Equivalent circuit model of double insulating layer type ACTFEL device (C_p : Capacitance of phosphor layer. C_i : Total capacitance of insulating layer. C_{i1} and C_{i2} : Capacitance of the first and second insulating layer. V_a : Total applied voltage. V_{EL} : Voltage across the phosphor layer. V_1 : Voltage across the insulating layer).

ACTFEL equivalent circuit was as shown in figure 2.11a. This model treats the two insulator layers as perfect capacitors and phosphor layers as a capacitor shunted by two back-to-back Zener diodes. Another early model was proposed by Alt [50] and is shown in figure 2.11b. Alt modeled the phosphor layer as a capacitor shunted by a voltage-controlled current source that turns on sharply at the threshold voltage. This simple model

accurately predicts the most significant characteristics of an ACTFEL device. Ono [15] summarized the relation between the applied voltage and the capacitance of each layer as follows.

The total capacitance of the insulating layer can be calculated by the capacitance of the first and second insulating layer (C_{i1} and C_{i2}) by

$$C_i = \frac{C_{i1} C_{i2}}{C_{i1} + C_{i2}} . \qquad (2\text{-}22)$$

As shown in figure 2.11b, the total applied voltage (V_a) on the device is equal to the voltage across the insulating layers (V_I) plus the voltage across the phosphor layer (V_{EL}):

$$V_a = V_I + V_{EL} . \qquad (2\text{-}23)$$

Below the threshold voltage, the voltage ratio on the phosphor layer and the insulating layer is decided by the capacitance of each component such that

$$V_{EL} = \frac{C_I}{C_I + C_{EL}} V_a , \qquad (2\text{-}24)$$

$$V_I = \frac{C_{EL}}{C_I + C_{EL}} V_a . \qquad (2\text{-}25)$$

However above the threshold voltage, current starts to flow through the resistor branch as shown in figure 2.11b and keep the voltage across the phosphor capacitor at the threshold level. The current through the resistive branch charges up the insulating layer capacitor to maintain a constant voltage across the device. Therefore, the final voltage values across the phosphor and insulating layers are

$$V_{EL,f} = \frac{C_I}{C_I + C_{EL}} V_{th} \qquad (2\text{-}26)$$

$$V_{I,f} = V_a - V_{EL,f} = \frac{C_{EL}}{C_I + C_{EL}} V_{th} \, . \qquad (2\text{-}27)$$

This equation shows field clamping, i.e. the voltage across the phosphor layer is maintained at the threshold regardless of the actual applied voltage. In addition, transferred charge and luminance of ACTFEL device at a given over-voltage can be estimated from the equivalent circuit shown at figure 2.11b. Douglas and Wager [51] modified the ACTFEL device equivalent circuit by adding parallel resistor and capacitor combination, C_T and R_T, in series with the Zener diode, as shown in figure 2.12. This model more accurately describes the dependence of the turn-on voltage and relaxation charge on the applied voltage waveform. However, the physical origin of this parallel RC network is not entirely yet clear.
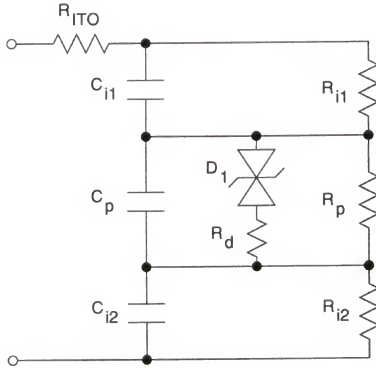
Figure 2.12 Modified equivalent circuit model of an ACTFEL device, as suggested by Douglas and Wager [51].

2.5.2.2 Electrical characteristics

It is important to understand the electrical characteristics of the ACTFEL, which is an electrooptic device whose performance is determined by its' electrical properties. In this section, the predictions from the model by Wager, et al. [52-54] will be discussed in terms of the parameters such as charge – voltage (Q-V), capacitance – voltage (C-V), internal charge – phosphor field (Q_{int} – F_p) and maximum charge – maximum applied voltage (Q_{max} – V_{max}). The Sawyer-Tower circuit normally used for two terminal electrical characterization of ACTFEL device is shown in Figure 2.13 [55].
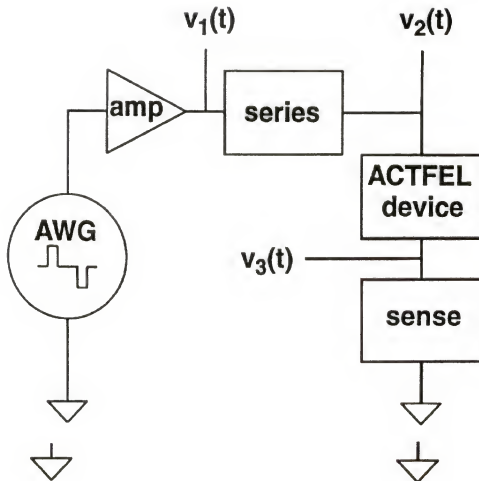
Figure 2.13 Sawyer-Tower circuit used for two terminal electrical characteristics of an ACTFEL device (AWG : Arbitrary waveform generator. Amp : High voltage amplifier. Series : Series resistor normally between 100Ω and 1kΩ. Sense : Sense capacitor with value C_s) [55].

In this circuit, the desired ac signal is generated by arbitrary waveform generator and voltage amplifier. Typically, 100Ω - $1k\Omega$ resistor is used as the series element, which acts as a current-limiter to protect the ACTFEL device from catastrophic breakdown. However, as this series resistor increases, the RC time constant of circuit increases and the dynamic response of the device is delayed. Normally capacitance is used as the sense element and the value of the sense capacitance is much larger than the ACTFEL device to make most of applied field to drop across the device. As shown in figure 2.13, the transient voltage drop across each element is monitored by oscilloscope. The standard waveform, which is typically used for electrical characterization, is a bipolar trapezoidal pulse, with rise time and fall time of 5μs, and pulse width of 30μs. A-J labels are used to indicate certain important points in the applied voltage. B and G in the figure 2.14 indicate the point of the initiation of conduction in the phosphor layer. Except for B and G, the significance of the labeled points is obvious.
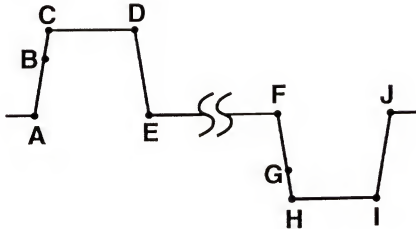
Figure 2.14 Standard applied voltage waveform used for electrical characterization of ACTFEL device [52].

The current passing through each series element in the circuit is constant and can be calculated using the series resistor by

$$i(t) = \frac{V_1(t) - V_2(t)}{R_{series}}$$ (2-28)

where $V_1(t)$, $V_2(t)$ and $V_3(t)$ are the voltages monitored at points as shown in figure 2.13.

The external charge also can be calculated by integrating the current over time as follows :

$$Q_{ext}(t) = \int_0^t i(t)dt.$$ (2-29)

When a sense capacitor is used, the external charge can be calculated by

$$Q_{ext}(t) = C_s V_3(t)$$ (2-30)

where C_s is the sense capacitor shown at Figure 2.13.

The voltage across the ACTFEL device can be obtained directly from the voltage drop by

$$V_{EL}(t) = V_2(t) - V_3(t).$$ (2-31)

Therefore, the external charge – voltage curve can be plotted using $Q_{ext}(t)$ versus $V_{EL}(t)$ [56,57]. An ideal Q-V plot shown in figure 2.15. Q_{cond} is the conduction charge transported across the phosphor layer during the voltage pulse. This is the charge which is responsible for impact excitation of the luminescent centers. Q^ε_{pol} is the polarization charge stored at the phosphor/insulator interface right before the opposite polarity pulse is turned on. Q^ε_{leak} is the charge which has leaked off during the time between pulses (8.3

msec at 60 Hz) by electron emission from shallow interface. Q_{relax} is the relaxation charge that flows across the phosphor layer during the time that the voltage is held at it's maximum value during the pulse. The power dissipated in a device is proportional to the area inside the curve and used to define the power efficiency of the device.

Figure 2.15 Idealized Q-V curve of ACTFEL device (V_{to} : the electrical turn-on voltage. Q_{cond} : Conduction charge. Q_{pol}: Polarization charge. Q_{leak} : Leak charge. Q_{relax} : Relaxation charge) [52].

The capacitance – voltage (C-V) data are complementary method to charge – voltage (Q-V) data [58-62]. The dynamic capacitance can be obtained simply by the derivative of Q-V as follows:

$$C(V_{EL}) = \frac{dQ_{ext}(t)}{dV_{EL}(t)}.$$ (2-32)

Another method to assess the C-V curve is to use the current through the ACTFEL device and the voltage derivative across the ACTFEL device with respect to time as follows:

$$C(V_{EL}) = \frac{i(t)}{\dfrac{dV_{EL}(t)}{dt}} . \qquad (2\text{-}33)$$
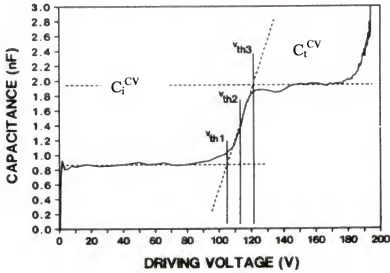
Figure 2.16 Typical C-V curve for ZnS:Mn ACTFEL device (V_{th1} : the onset of electron emission from the shallowest interface traps. V_{th2} : average turn-on voltage. V_{th3} : the field-clamping regime. C_i^{CV} : Capacitance after turn-on obtained from C-V plot. C_t^{CV} : Capacitance before turn-on obtained from C-V plot) [58].

Based on this expression for C, the C-V curve can be plotted as C versus V_{EL}. Figure 2.16 shows the C-V curve of a ZnS:Mn ACTFEL device. The C_t^{CV}, which is the capacitance before turn-on, corresponds to the total capacitance of the ACTFEL device (C_t^{phys}). Usually C_t^{CV} and C_t^{phys} show good agreement. C_i^{CV} is the capacitance after turn-on, and it corresponds to the series combination of two insulators (C_i^{phys}). However, in

the real case, C_i^{CV} value can deviate from C_i^{phys}. If the conduction charge is not enough to

completely shunt the phosphor capacitance, C_i^{CV} will be lower than C_i^{phys}. If there is

dynamic space charge, C_i^{CV} will saturate at larger than C_i^{phys} values, sometimes with

overshoot in C-V curve as shown in 2.17 [62]. If sufficient conduction charge is

generated and no space charge exists, the dynamic space charge after the turn-on (C_i^{CV})

will be approximately the same as the insulator capacitance (C_i^{phys}).
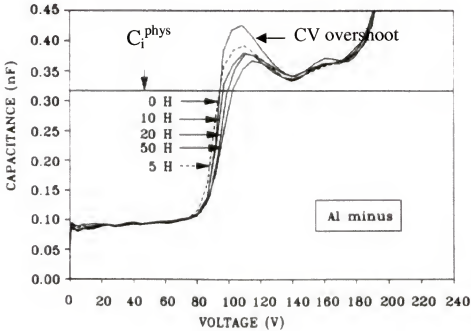
Figure 2.17 Real C-V overshoot in ALE grown ZnS:Mn ACTFEL device as aging time (C_i^{phys} : total capacitance of insulating layers. 0H, 5H, 10H, 20H and 50H represent aging time) [62].

As shown in figure 2.16, the threshold voltage of ACTFEL device is not defined

sharply but has a transition region. V_{th1} is attributed to the onset of emission of electron

from shallow interface traps and V_{th3} corresponds to the initiation of field clamping, while V_{th2} is the average turn-on voltage.

Even though $Q_{ext}(t)$-$V_{EL}(t)$ data give direct measurements of the charge as shown in figure 2.15, it has limitation in the information because the capacitive displacement charge is not separable in $Q_{ext}(t)$-$V_{EL}(t)$ data. Therefore the $Q_{int} - F_p$ technique was developed to provide the internal electrical characteristics of the ACTFEL device rather than a combination of internal and external characteristics given by the Q-V and C-V techniques [63-68]. The internal charge in the phosphor layer (Q_{int}) can be obtained as follows:

$$Q_{int}(t) = \frac{C_i + C_p}{C_i} C_s V_3(t) - C_p(t)[V_2(t) - V_3(t)] \qquad (2\text{-}34)$$

where C_i and C_p are insulator and phosphor capacitors, respectively, and C_s is the sense capacitance. $V_2(t)$ and $V_3(t)$ are the voltages as shown in the figure 2.13. Therefore, $V_3(t)$ is the voltage across the sense capacitor and $V_2(t)$-$V_3(t)$ is the voltage across the ACTFEL device. The internal electric field $F_p(t)$ is given by

$$F_p(t) = \frac{1}{d_p}(\frac{C_s V_3(t)}{C_i} - [V_2(t) - V_3(t)]) \qquad (2\text{-}35)$$

where d_p is the thickness of the phosphor layer. The internal charge versus phosphor field ($Q_{int} - F_p$) curve can be obtained by plotting $Q_{int}(t)$ versus $F_p(t)$ and an idealized $Q_{int} - F_p$ curve is given at figure 2.18.

Various fields and charges can be evaluated from these $Q_{int} - F_p$ data. In figure 2.18, F_{ss} is the steady –state phosphor electric field which results in the emission of

electrons from a large density of interface states. Q_{cond} is the conduction charge transported across the phosphor during a voltage pulse, which is the charge responsible for impact excitation of the luminescent centers. Q_{pol} is the polarization charge stored at the phosphor/insulator interface right before the onset of the subsequent pulse of opposite polarity. Q_{leak} is the leakage charge by emission of electrons from the shallow interface states during the zero applied voltage region between pulses. Q_{relax} is the relaxation charge that flows across the phosphor when the voltage pulse is held at a constant maximum. While the charge in the Q_{ext}-V_{EL} plot is the charge which has been transported in the ACTFEL device including the insulating layers, the charge displayed in the $Q_{int} - F_p$ plot is the charge which has been transported in the phosphor layer.
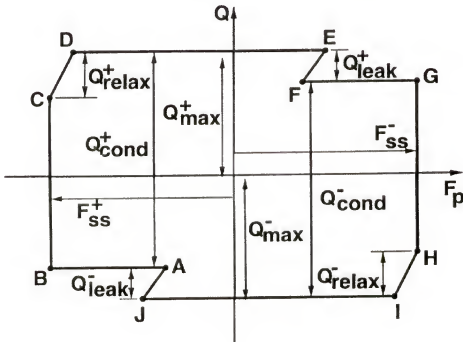
Figure 2.18 An idealized $Q_{int} - F_p$ curve of ACTFEL device (F_{ss} : Steady-state phosphor electric field. Q_{cond} : Conduction charge. Q_{pol} : Polarization charge. Q_{leak} : Leak charge. Q_{relax} : Relaxation charge) [52].

Another electrical characterization method for ACTFEL devices is maximum charge – maximum voltage (Q_{max}-V_{max} or Q^e_{max}-V_{max}) [69,70]. The Q^e_{max}-V_{max} curve of evaporated ZnS:Mn ACTFEL device and its' derivative ($\partial Q^e_{max}/\partial V_{max} - V_{max}$) are given at figure 2.19a and b. The maximum charge is the charge stored on the sense capacitor during one cycle of the voltage waveform, and the maximum voltage is the amplitude of the applied voltage pulse leading to the corresponding maximum charge. There are two types of maximum charge. One is internal charge that can be obtained from $Q_{int} - F_p$ data, and the other is the external charge that can be obtained from the Q_{ext}-V_{EL} plot. For Q_{max}-V_{max} plots, the capacitance value of the device should be known accurately because Q_{int} (t) is calculated using the capacitance values of the phosphor and insulating layers as shown in equation (2-34). In contrast, Q^e_{max}-V_{max} is more reliable than Q_{max}-V_{max} because Q^e_{max} is a directly measured value [69]. The slope of the Q^e_{max}-V_{max} plot shows the charge transfer efficiency of the ACTFEL device. If the slope of Q^e_{max}-V_{max} is larger than the C_i^{phys}, more charge than emitted from the cathode interface arrives at the anode interface due to charge multiplication from electron hole pairs generated by energetic electrons. This electron multiplication can occur by either bulk phosphor trap ionization (involved in the creation of dynamic space charge) or band-to-band impact ionization (not involved in the creation of dynamic space charge). The bulk phosphor trap ionization and other dynamic space charge generation can result in overshoot in Q-V or C-V plots. If the slope of Q^e_{max}-V_{max} is smaller than the C_i^{phys}, this means that the transferred charge is not sufficient for field clamping or pseudo-field clamping [69]. The derivative versus voltage curve ($\partial Q^e_{max}/\partial V_{max} - V_{max}$) as shown in figure 2.19b gives better insight than

does the Q^e_{max}-V_{max} plot because $\partial Q^e_{max}/\partial V_{max}$ is a capacitance and this capacitance correlates with the insulator capacitance of the ACTFEL device.
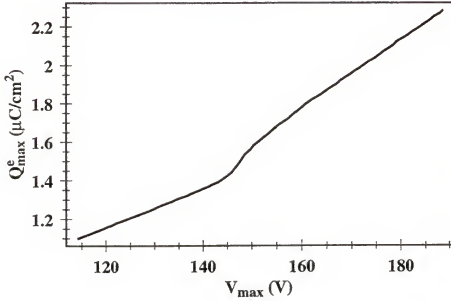
a)

b)
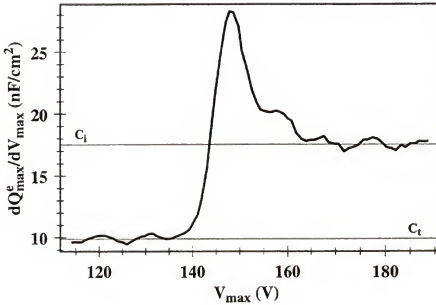
Figure 2.19 The Q^e_{max}-V_{max} curve a) of evaporated ZnS:Mn ACTFEL device and its derivative ($\partial Q^e_{max}/\partial V_{max}$ − V_{max}) b) (C_i: Actual capacitance of the insulator layer. C_t: Actual capacitance of total ACTFEL device) [69].

2.6 ZnS:Tb as ACTFEL Phosphor

2.6.1 Optical Property of ZnS:Tb Phosphor

As mentioned in the section 2.3.3 and 2.4.4.2, Tb has a parity forbidden $4f$ intrashell transition. The $4f$ shell is shielded by the $5d$ and $6s$ shells and therefore the Tb^{+3} ion transition is not affected significantly by the crystal field of the host. As a result, the radiative decay of the Tb^{+3} ion shows relatively slow decay ($\tau \approx$ several msec) and the emission spectrum of Tb^{+3} ion transition is almost the same and independent of the host material. Figure 2.20 shows the EL emission transitions of Tb^{+3} in ZnS and the corresponding emission peaks.
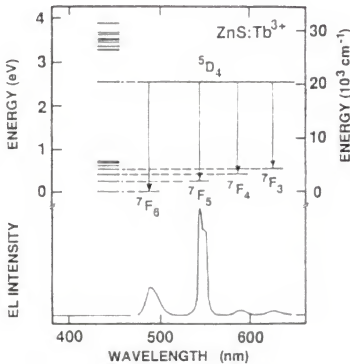
Figure 2.20 The EL emission spectrum of ZnS:Tb^{+3} and the corresponding radiative transitions [15].

2.6.2 Deposition Methods

The use of ZnS:Tb,F phosphor film for EL was originally proposed by Kahng [71] in 1968 and is called LUMOCEN (LUminescent from MOleculer CENter) because the luminescent centers were doped in the form of TbF$_3$ molecules. The fabrication methods for ZnS:Tb,F film were co-evaporation of ZnS and TbF$_3$ from two sources [72, 73]. Coevaporation was used because Tb^{+3} has an ionic radius of 0.923Å, which is 25% larger than that of the Zn^{+2} ion. This size mismatch makes thermal diffusion of Tb ions into the ZnS lattice difficult. To achieve higher doping levels, the sputtering process [74-77] was used since it imparts a kinetic energy of several eVs to the nucleating atoms during the film growth. Ion bombardment during sputtering influences both the crystal growth of the ZnS and the Tb dopant incorporation site in such a way that the Tb dopant is more effectively incorporated into the thin film phosphor [15]. However, the crystallinity of the film also is critical to its performance in EL. Mita et. al. [73] reported that the F/Tb ratio remained equal to three and the EL spectra for electron beam evaporated films was not affected by annealing temperatures up to 450°C. Figure 2.21 shows the F/Tb ratio dependence upon the annealing temperature for EL devices fabricated using electron-beam evaporation or rf magnetron sputtering. The value of the F/Tb in the as-deposited electron beam evaporated film is around 3, but decreases slightly to 2 ~ 2.5 after annealing at 600°C. However, the F/Tb ratio for sputter deposited films decreased remarkably, compared with that for the electron beam evaporated film. They postulated that for electron beam evaporated film, Tb and F ions substitute on the Zn and S sites with two Zn vacancies being required for TbF$_3$ center. For sputter deposited films, interstitial F ions are released from the ZnS film and Tb-F complex centers are formed upon annealing.

Hirabayashi et al. [78] reported on the photoluminescent and electroluminescent properties of $ZnS:TbF_X$ grown by metal organic chemical vapor deposition (MOCVD). According to this report, there is no difference in EL characteristics between $ZnS:TbF_X$ EL devices with various x values. This result does not agree with the results reported above for sputter deposited films. Presumably this is because the sites of F ions in sputter deposited films are different from those in MOCVD-prepared films. Atomic layer deposition (ALD) also has been used to grow ZnS:Tb films. Kong et al. [79] reported that it is difficult to substitutionally introduce a large concentration of Tb into ZnS because of the size and charge mismatch of Zn^{+2} and Tb^{+3}. So even at 2 at.% Tb, the brightness decreased as doping concentration increased.
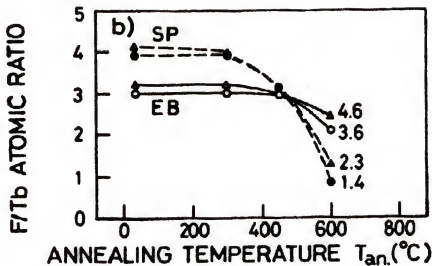
Figure 2.21 The F/Tb ratio versus the annealing temperature for ZnS:Tb,F films fabricated by electron-beam evaporation or rf magnetron sputter deposition [73].

2.6.3 Charge Compensators and Excitation Mechanisms

As mentioned in section 2.6.1, the EL brightness of ZnS:Tb,F is dependent on the F/Tb ratio [80-83]. This dependence of the electroluminescent brightness (in fL) on x for ZnS:TbF$_X$ is plotted in Figure 2.22.
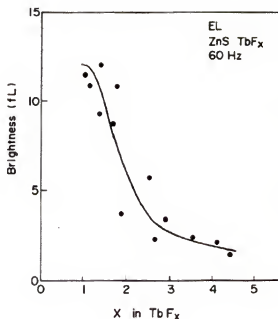
Figure 2.22 Dependence of electroluminescence brightness on the x value in ZnS:TbF$_X$ film. The brightness is measured at 30V above the threshold voltage with 60 Hz excitation (E/Tb ratio was measured by electron probe microanalyzer (EPMA) [81].

The brightness increases as x decreases, implying that the F dissociation from TbF$_3$ is beneficial for EL emission. Okamoto et al. [81] proposed that the TbF complex center is composed of Tb at the Zn site surrounded by interstitial F in a luminescence complex in which F acted as the charge compensator for Tb^{+3}. The lattice constant of the film from X-ray diffraction data from ZnS:TbF (x=1) was 5.44-5.45Å, which is larger than the 5.42 Å for ZnS single crystals [81]. Also they compared the EL spectra from the

$^5D_4 - {}^7F_5$ transitions in Tb^{+3} ions for films with values of x=3 or 1 with the PL spectra of

TbF_3 and a ZnS:Tb crystal. (Figure 2.23)
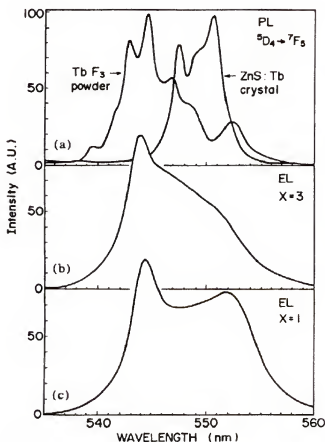
Figure 2.23 Photoluminescence (PL) spectra for a) TbF_3 powder and a ZnS:Tb_x crystal versus the EL spectra for b) x=3, and c) x=1 [81].

The envelope of the PL spectrum for TbF_3 powder is quite similar to the EL

spectrum from the film with x = 3. On the other hand, the EL spectrum for the film with

x=1 appears to be consistent with a mixture of the PL spectra for TbF_3 and the ZnS:Tb

crystal. Okamoto, et al. [81] concluded that Tb exists as the TbF_3 molecule in ZnS for

x=3, and that the crystal field of ZnS does not affect the spectrum due to a shielding

effect of the three F atoms around the Tb core. In the case of x=1, Tb is believed to substitute for the Zn site with F on a site very close to the Tb because the TbF$_3$ peak at 544nm is still observed in the spectrum.

The EL excitation [84-87] and emission mechanism [88-93] of ZnS:Tb,F has been well studied. Okamoto et al. [94] reported that the excitation mechanism of the Tb center involves resonant energy transfer from the ZnS host to the $4f^8$ electronic level in the Tb^{+3} ions based on time-resolved PL and EL spectra from ZnS:TbF thin films.

Okamoto et al. [95] also studied the effect of oxygen doping in ZnS:TbF electroluminescent (EL) thin films. They obtained the highest brightness when S/Zn, F/Tb and O/Tb atomic ratios are around unity. So they suggested that the Tb and O acted as substitutional impurities with Tb assuming Zn sites and O assuming S sites in the ZnS lattice and the F occupying the interstitial site. Based on this assumption, they concluded that the Tb-O-F complex centers are responsible for the high EL brightness. They suggested two mechanisms [81] for the improved brightness due to the presence of O in ZnS:TbOF. One mechanism is reduced nonradiative transition rates as indicated by the fact that the host-excited photoluminescence intensity increased by about 10% with the addition of oxygen. The other mechanism is improvement of the excitation efficiency of the Tb center because O distortion increased the impact ionization cross section of the host.

Okamoto et al. [96] developed a two target rf-magnetron sputter deposition system with independent ZnS and TbOF or TbSF targets with motion of the substrate between these sources. They reported that this resulted in good controllability of both ZnS thickness and Tb doping concentration, and that TbOF gave better results than TbSF.

They also report that the crystallinity of the ZnS film increased when an Ar and He mixture was used for sputtering, presumably because He reduced sputter damage in the ZnS lattice. Reduced crystalline damage was postulated to result in hotter electron energies due to less scattering and therefore increased excitation probability of Tb centers.

CHAPTER 3
EXPERIMENTAL PROCEDURE

3.1 Introduction

In this section, the procedure and conditions for sputtering deposition of ZnS:TbOF thin films and characterization methods will be described. The characterization methods include the microstructural, compositional, optical and electrical analyses, which are used in this study.

3.2 Device Fabrication

3.2.1 Substrates

Corning 7059 glass substrates, 0.04 inch thick, coated with 360nm of indium tin oxide (90wt% In_2O_3 + 10wt% of Sn_2O_3 (ITO)) as a transparent conducting electrode and 160nm of aluminum titanium oxide (Al_2O_3/TiO_2 (ATO)) as a bottom insulator layer, were supplied by Planar Systems. The bottom dielectric layer (ATO) was deposited using atomic layer deposition (ALD). The X-ray diffraction (XRD) pattern of the Corning 7059 glass substrate coated with ITO or coated with ITO and ATO are shown in Figure 3.1a and b, respectively, and XRD peaks are evident from the polycrystalline ITO layer. The Corning 7059 glass substrate coated with ATO in addition to the ITO show no additional XRD peaks since ATO is amorphous. Every substrate is cleaned for 6 minutes by UV(Ultraviolet) photons in air which generates ozone. This treatment removes organic contamination from the substrate surface.
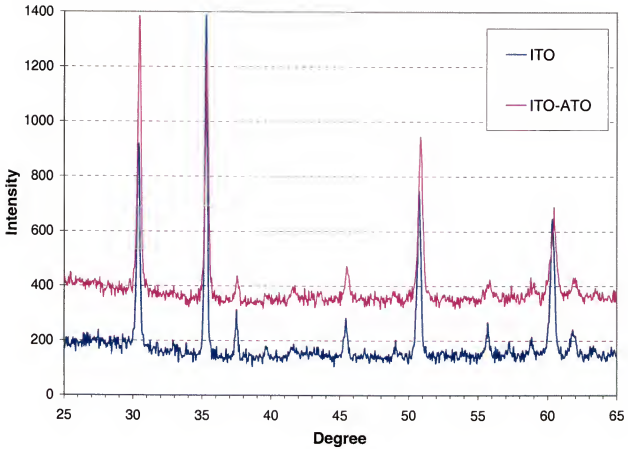
Figure 3.1 The X-ray diffraction patterns of the Corning 7059 glass substrate coated with ITO (a) and coated with ITO and ATO (b).

3.2.2 Film Deposition

ZnS:TbOF thin films were deposited onto these ATO/ITO/glass substrates by R.F. planar magnetron sputtering. The schematic of the sputter deposition system is shown in Figure 3.2.
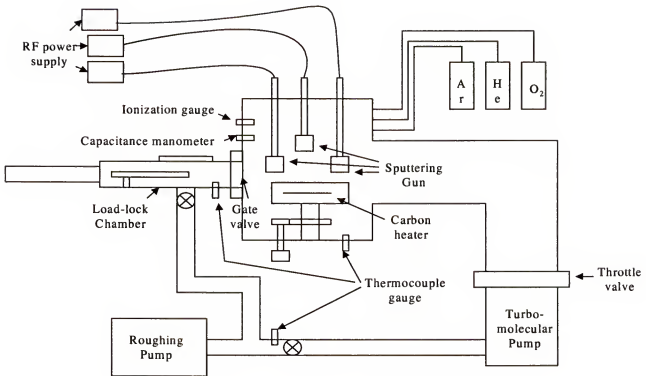
Figure 3.2 Schematic of the sputter system used for RF planar magnetron deposition of ZnS:Tb,O,F thin films and co-dopants including Cu, Ag, and Ce_2O_3.

This sputter deposition system is designed to simultaneously operate 3 RF-sputter guns, which makes possible co-sputtering of additional codoping elements from separate targets. The substrate holder has the capability to hold four 2 × 2″ substrates or eight 1 × 2″ substrates. This substrate holder rotates at a constant speed driven by a stepping motor. In this study, the rotation speed is constant at 11 seconds per revolution for all depositions. Also substrates can be heated up to 300°C by a carbon heater. The load-locked chamber is pumped down to 10 mTorr by a wet rotary vane pump (Leybold

Trivac D65B) through the right angle valve. For high vacuum pumping of the main

chamber, a turbomolecular pump (Leybold Turbovac 450) backed by the rotary roughing

pump is used. The ultimate pressure of this deposition system is $< 1 \times 10^{-6}$ Torr. As

sputtering gas, ultra high purity Ar, ultra high purity He and also ultra high purity O_2 can

be used simultaneously or separately. Sputtering gas pressure can be controlled by the gas

flow rate and a throttle valve, which is installed between the main chamber and the turbo

molecular pump. The vacuum pressure is measured by thermocouple gauges (in the load-

lock chamber, foreline and main chamber), an ionization gauge (in main chamber) and a

capacitance manometer (in the main chamber). The capacitance manometer gauge is used

to monitor chamber pressure during deposition. Total sputter gas pressure is kept at 20

mTorr for all deposition even if using mixed gases. The target to substrate distance is

about 5cm.

3.2.3 Film Annealing

Sputter-deposited films are annealed using halogen lamps, which are cooled by

water and nitrogen. A schematic of the annealing furnace is shown in Figure 3.3. A set of

three halogen lamps are located above and below the quartz tube. The quartz tube is

purged for 40 minutes by high purity nitrogen gas (99.99999%) to remove residual

oxygen before annealing. Nitrogen purging continues during the anneal. The samples are

located in the graphite susceptor, which is in the middle of the quartz tube. Two pieces of

silicon wafer cover the bottom and top of the samples to protect them from contamination

by the graphite. A thermocouple is placed on a dummy glass sample to control the

temperature. A typical ramping time to 500°C is 2 minutes and cooling time to < 100°C is about 15 minutes.
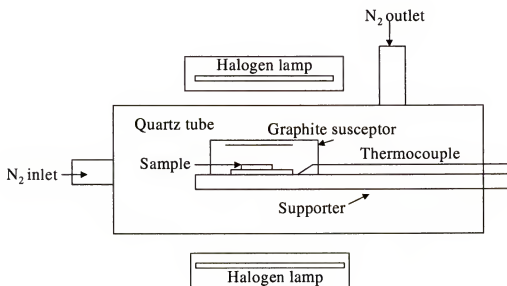
Figure 3.3 Schematic of the "rapid thermal" annealing furnace showing the lamp heaters and nitrogen flow.

3.2.4 Top Dielectric Layer

For most samples in this study, half cell data are collected instead of full cell data. In a half cell structure, the top dielectric layer was not deposited; only the top Al dot contacts were deposited directly onto the ZnS:Tb films. The device brightness is changed by the capacitance of the top dielectric layers. Therefore, a more direct comparison of phosphor properties is given by a comparison of half cell brightness and efficiency. For full cell samples, $BaTa_2O_6$ (BTO) is used for the top dielectric layer and was deposited

using RF diode sputter deposition in a mixed Ar/O_2 (77%/23%) at 30mTorr from a $BaTa_2O_6$ target. Typical baseline gas pressure is $< 5 \times 10^{-6}$ Torr. A typical dielectric constant for BTO is about 26 and a typical thickness is about 2500nm ± 10%.

3.2.5 Electrode Deposition

Electrodes on the both sides of the phosphor film are required to apply an electric field across the device. The top electrode (Al) is formed by thermal evaporation through a shadow mask that has a circular diameter of 0.1″. The typical base pressure is $< 5 \times 10^{-6}$ Torr and a typical thickness is 200nm. Electrical contact to the bottom electrode (ITO) for testing is achieved by scratching through the upper insulating layers with a diamond scribe and melting pure indium onto the scratched area. The molten indium wets the bottom ITO electrode for electrical contact.

3.3 Characterization

3.3.1 Thickness Measurement

The thickness of each film is measured using the optical interferometry method [98] for the film deposited on a dummy glass substrate. The index of refraction of the film and substrate are known and they are transparent. The incident visible beam is reflected at the different interface (the air-film and film-substrate) creating interferences versus wavelength that depend on the thickness of the films.

3.3.2 EL Performance Measurement

The primary optical properties such as brightness, chromaticity and emission spectrum are measured routinely for all deposited films. A typical a.c. trapezoidal wave is applied at a frequency of 60 Hz. The pulse rise and fall times are each 5µs and the pulse duration is 30µs. Figure 3.4 shows the typical a.c. trapezoidal waveform used to drive the ACTFEL devices. The EL brightness, CIE color coordinates and emission spectrum is measured by PhotoResearch a PR-650 spectra colorimeter.
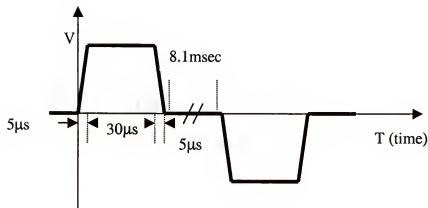
Figure 3.4 Alternating current trapezoidal voltage waveform used to drive ACTFEL devices at a frequency of 60 Hz.

3.3.3 Photoluminescence (PL) Measurement

He:Cd laser with a wavelength of 325nm was utilized to excite PL from the phosphor layers in this study. The PL measurement is carried out at room temperature in a dark room. The emission spectrum is collected from 350nm to 800nm. In this study,

films for PL measurement were mounted in air by using metal clip without backing plates to avoid luminescent "noise" emitted or reflected from the backing plate and mounting tape.

3.3.4 X-ray Diffraction (XRD)

X-ray diffraction (XRD) is widely used to generate information about the crystallography of materials. In this study, a Philips APD 3720 X-ray diffractometer is used. Typically the scan range is from 25° to 65° and the scan rate is 0.05°/sec. For the full width at half maximum (FWHM) measurement, the scan range is from 27° to 30° and the scan rate is 0.005°/sec. The X-ray wavelength is 1.54056Å, which is generated from a Cu target bombarded by a 40KeV, 20mA electron beam. X-rays incident on the specimen may be diffracted according to Bragg's law:

$$n\lambda = 2d_{hkl} \sin \theta$$

where n is a integer, λ is the wavelength of the incident X-ray, d_{hkl} is the spacing of the (hkl) plane, and θ is the angle between the incident or detection directions and the surface normal. The sampling depth for XRD is a few micrometers depending on the X-ray absorption coefficient of the diffracting material. From the diffracted beam intensity versus the diffraction angle 2θ, valuable information such as crystallographic structure, preferred crystallographic orientation, internal stress, crystallite size and crystallinity of the materials can be obtained [97]. Among these properties, the crystallinity of the materials can be measured by FWHM. Figure 3.5 shows an XRD peaks for a real a and ideal case b. In the ideal case, the incident rays that have only a slightly different angle from the precise Bragg angle should be completely destroyed by interference. However,

imperfection in crystal such as defects, dislocations and grain boundary plus divergence in the non-monochromatic X-ray beam makes this destructive interference incomplete. So as shown in Figure 3.5a, the peak is broadened, and the breadth can be an indicator of the crystallinity of the film.
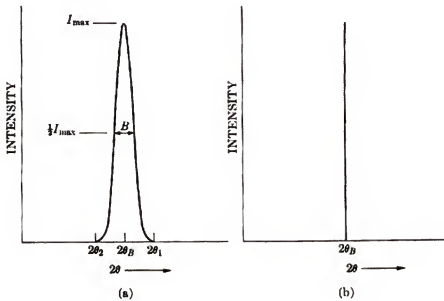
Figure 3.5 XRD peaks from a real sample (a) and an ideal condition (b) [97].

3.3.5 Energy Dispersive Spectrometry (EDS)

Quantitative detection and analysis of the codoping elements is accomplished with energy dispersive spectroscopy (EDS Tracor System II EDS System) with a 15keV beam energy in a JEOL 6400 scanning electron microscope (SEM). EDS detects the X-rays produced as a result of the inner shell ionization of an atom by high-energy electrons. To return the ionized atom to its ground state, an electron from a higher energy outer shell fills the vacant inner shell hole and, in the process, an amount of energy equal

to the potential energy difference between the two quantum states is released. This excess energy, which is unique for every atomic transition, will be emitted by the atom either as an X-ray photon or as an Auger electron. Emitted X-rays pass through the EDS window protecting the detector and are absorbed by the detector crystal. The detector generates a charge pulse proportional to the X-ray energy. This pulse is converted to voltage and amplified by a field effect transistor (FET). The amplified signal is processed into a digital signal by an analog-to-digital converter (ADC) of the multichannel analyzer (MCA). Even though EDS has poor energy resolution and relatively high detection limit (0.1 wt %), [98] it is used as reference for quantification of codopants.
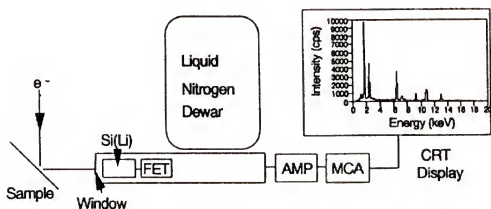
Figure 3.6 Schematic of EDS system. The incident electron interacts with the specimen with the emission of X-rays. These X-rays pass through the window protecting the Si(Li) and are absorbed by the detector crystal. The X-ray energy is transferred to the Si(Li) and processed into a digital signal that is displayed as a histogram of number of photons versus energy [98].

3.3.6 Secondary Ion Mass Spectrometry (SIMS)

SIMS is one of the most sensitive analytical techniques with elemental detection limits in the ppm to sub-ppb range, depth resolution as good as 2nm and lateral resolution between 50nm and 2μm [98]. SIMS can be used to measure any elemental impurity, from hydrogen to uranium and any isotope of an element. Therefore, SIMS is almost always the analytical technique of choice when ultrahigh sensitivity with simultaneous depth or lateral information is required for a thin film. In this technique, primary ions (oxygen or cesium) having energies between 1 and 20keV impact a solid surface, transferring energy to atoms in the surface through direct or indirect collisions. The energy and momentum transfer process results in the ejection of neutral and charged particles from the surface. The depth of the mixing zone which limits the depth resolution of SIMS analysis is typically 2 – 30nm, and is a function of the energy, angle of incidence, and mass of the primary ions as well as the sample materials. There are three kinds of primary ion beams typically used in SIMS analyses, namely oxygen (O_2^+ or O^-), cesium (Cs^+) or argon (Ar^+). The use of an oxygen beam can increase the ion yield of positive ions while the use of a cesium beam can increase the ion yield of negative ions, in both cases by as much as four orders of magnitude. A simple model qualitatively explains this observation by postulating that the M-O bonds are formed in an oxygen-rich mixing zone, created by oxygen ion bombardment [98]. When these bonds break in the ion emission process, oxygen tends to become negatively charged due to its high ionization potential, and its counterpart M dissociates as a positive ion. Conversely, the enhanced ion yields of the cesium ion can be explained using a work function model, which postulates that because the work function of a cesiated surface is dramatically reduced, there are more secondary

electrons excited over the surface potential barrier to result in enhanced formation of negative ions. In this study, secondary ion mass spectrometry (Physical Electronics PHI 6600) with a 5 to 7keV O_2^+ or Cs^+ beam is used to measure codoping elements such as Ce and Cu, plus S, O and F. To quantify these data, the relative intensity of the codoping elements to the matrix element (Zn^+) is normalized to the concentration measured by EDS.

3.3.7 Auger Electron Spectroscopy (AES)

Auger electron spectroscopy (AES) is another method employed for quantitative detection of the elemental composition. The basic Auger process involves the production of an atomic inner shell vacancy usually by electron bombardment. The energy given by the transition of electrons from the excited state to the inner shell vacancy is transferred to the outer shell electrons and ejects energetic Auger electrons. These Auger electrons are detected by an energy analyzer. AES can be combined with ion-beam sputtering to remove materials from the surface and to continue to monitor the composition and chemistry of the remaining surface as this surface moves. The sampling depth varies between 5 and 100Å depending upon the energy of the Auger electrons measured and the signal to noise ratio of the spectrum. The acquired primary data is presented in differential mode, i.e. $d[E \cdot N(E)]/dE$ versus E, where N(E) is the energy distribution of the secondary electrons being detected and E is their energy. This differential mode gives an improved signal to noise ratio. In this study, Auger electron spectroscopy was accomplished with a PHI model 660 scanning Auger microprobe with 5keV beam energy.

3.3.8 Atomic Force Microscopy (AFM)

Surface morphology and roughness are characterized by atomic force microscopy (Digital Instruments Nanoscope III) in the tapping mode (1 to 3 Hz). Figure 3.7 shows the schematic of the AFM in which a sharp tip is mounted on a flexible cantilever. When the tip comes within a few Å of the sample's surface, repulsive van der Waals forces
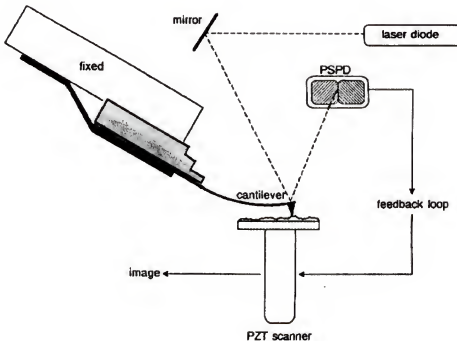
Figure 3.7 Schematic of AFM. Light from a laser diode is reflected from the back of the cantilever onto a position-sensitive photodiode. Piezoelectric transducer is employed to scan the tip across the sample and a feedback loop operates on the scanner to maintain a constant separation between the tip and the sample. The image is generated by monitoring the position of the scanner in three dimension [98].

between the atoms on the tip and those on the sample cause the cantilever to deflect. The magnitude of the deflection depends on the tip-to-sample distance d. The most common method for monitoring the deflection is with the beam bounce detection system. In this

system, light from a laser diode is reflected from the back of the cantilever onto a position-sensitive photodiode. A given cantilever deflection corresponds to a specific position of the laser beam on the position-sensitive photodiode. The position-sensitive photodiode can detect about 0.1Å displacements.

3.3.9 Electrical Characterization

A detailed review of electrical characterization was given in section 2.5.2.2. In this chapter the electrical measurement set-up is shown (Figure 3.8) and described. The applied voltage is the 60 Hz trapezoidal pulses (5 μsec rise time, 30 μsec dwell, 5 μsec fall time) described in section 3.3.2. A Tektronix TDS 510A digitizing oscilloscope is used to measure the voltage at each point indicated as V_1, V_2, V_3 and V_4 in figure 3.8. And the voltage drop across each element can be calculated, i.e. V_2-V_1 is the voltage drop across the resistor, V_3-V_2 is the voltage drop across the sense capacitor and the V_4-V_3 is the voltage drop across the EL device. The current passing through the EL device can be calculated by dividing the voltage drop across the sense resistor by the resistance of the sense resistor, such that

$$i(t) = \frac{V_2(t) - V_1(t)}{R_{series}}$$

where R_{series} is the series resistance. (In this study, 100Ω.)

And the external charge ($Q_{ext}(t)$) values are determined by integrating the current over time as discussed in section 2.5.2.2.

For time dependent EL emission (L(t)), luminance versus time data are collected on the Tektronix 510A oscilloscope from an Si-diode photomultiplier tube(PMT) manufactured by Oriel with 1KΩ bridge resistor.

The electrical measurement and the time dependent EL emission (L(t)) are alternately done for both aluminum and ITO electrode sides to collect data for both polarities.
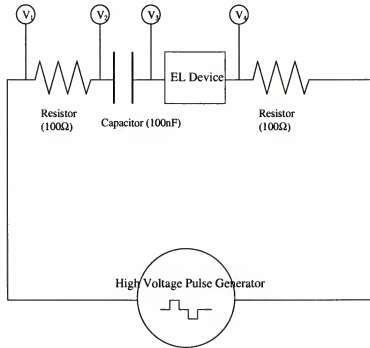
Figure 3.8 The electrical measurement set-up showing sense resistor (100Ω), sense capacitor (100nF), EL device and high voltage pulse generator.

CHAPTER 4
RF MAGNETRON SPUTTERING DEPOSITION FROM SINGLE ZnS:TbOF TARGET VERSUS TWO SEPARATE ZnS and TbOF TARGETS

4.1 Introduction

This chapter presents the results of RF magnetron sputtering deposition from two separate ZnS and TbOF targets and comparison between the films deposited from two separate ZnS and TbOF targets and the films deposited from a single ZnS:TbOF target. Okamoto et al.[96] used two separate ZnS and TbOF targets and reported good reproducibility and uniformity for sputter deposited thin films. The purpose of this study is to investigate the effects of a single ZnS:TbOF target versus two separate ZnS and TbOF targets on the EL and microstructural properties.

4.2 Experimental

To form a single target, ZnS powder (99.99 % purity) was mixed with TbOF powder at a concentration of 1.5 mole %. TbOF powder was synthesized by mixing and heating TbF_3 (99.99 % purity) and Tb_4O_7 (99.99 % purity). The mixed powder was hot pressed to make a consolidated 2" diameter target (Target Materials Inc.). Films from the single target were sputter deposited with a power of 120 W (power density $\approx$ 6 W/cm^2) in 20 mTorr of Ar gas at a substrate temperature between 150°C and 220°C.

To sputter deposit from two separate ZnS and TbOF targets, a 2" diameter dense ZnS disk (99.99+ % purity) grown by chemical vapor deposition at Morton International

Inc. was used along with a 2" diameter hot pressed powder TbOF target. The two sources were operated simultaneously with the substrate being continuously rotated under them at a speed of 11 seconds per revolution. The ZnS source was operated at 120W (power density ≈ 6 W/cm^2) in 20mTorr Ar. The TbOF source was operated in a pulsed mode from 30 to 100W (typically 40 - 60W, power density typically $\approx 2 - 3$ W/cm^2) in 20mTorr of Ar with a variable duty cycle (typically 30 - 60%) to change the concentration of TbOF in the deposited thin films. As for films from a single target, the substrate temperature was varied between 150 $^\circ$C and 250 $^\circ$C.

<div align="center">4.3 Results</div>

4.3.1 Deposition from Two ZnS and TbOF Targets

4.3.1.1 EL properties

The spectral distribution as well as the effect of terbium concentration on the electroluminescent emission of ZnS:TbOF films deposited from two targets is shown in Figure 4.1. The four emission peaks in the spectrum agree with those reported for terbium doped ZnS film. The largest peak at 544 - 548nm originates from a $^5D_4 \rightarrow {}^7F_5$ transition. The other peaks originate from $^5D_4 \rightarrow {}^7F_6$ (492nm), $^5D_4 \rightarrow {}^7F_4$ (588nm), $^5D_4 \rightarrow {}^7F_3$ (620nm) transitions, respectively. There was no significant change in the emission spectrum between 0.8 mole % and 7.2 mole % terbium doped films, except for a small shift of the 544nm peak at higher Tb concentrations.
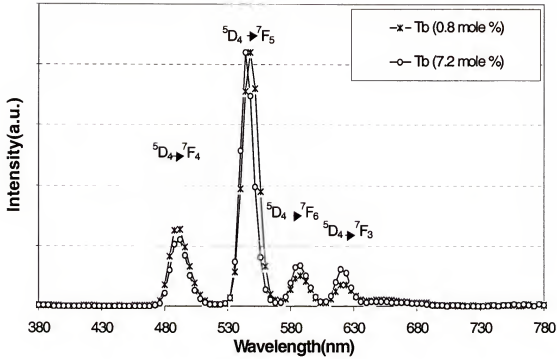
Figure 4.1 Emission spectrum of ZnS:TbOF with 0.8 or 7.2 mole % Tb^{+3} concentration. The emission spectra were largely unchanged by different Tb concentrations.

4.3.1.2 Tb concentration

The effect of terbium concentration on the electroluminescent brightness, B_{40}, of half stack devices is shown in Figure 4.2. Brightness increased in the low terbium concentration range (1 - 3 mole %), passed through a maximum at about 4 mole %, then decreased at higher terbium concentrations.
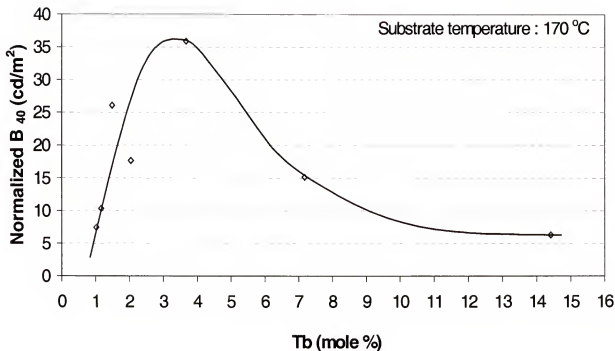
Figure 4.2 Normalized B_{40} versus Tb^{+3} concentration at a deposition temperature of 170 °C. Note the maximum B_{40} for a substrate temperature of 170°C occurs at about 4 mole % Tb.

4.3.1.3 Substrate temperature

The effects of changing the substrate temperature between 170 °C and 250 °C are shown in Fig.4.3. The brightness of films deposited at a substrate temperature of 250 °C was lower than that for films deposited onto 170 - 180°C substrates, with the higher brightness being obtained at 170°C. For films deposited from a single ZnS:TbOF target, the highest brightness was obtained at 160 °C.
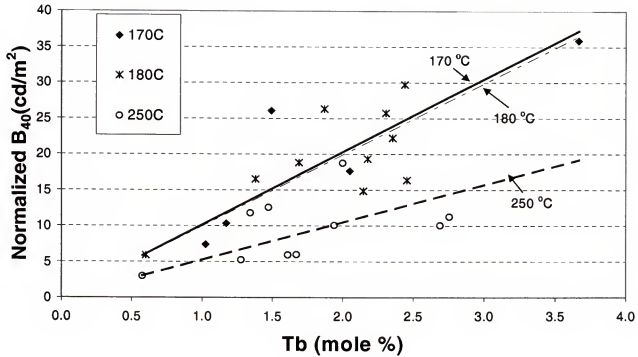
Figure 4.3 Normalized B_{40} versus Tb^{+3} concentration at a deposition temperature of either 170°C, 180°C, or 250°C.

4.3.2 Comparison from Single ZnS:TbOF Target

4.3.2.1 EL properties

The brightness versus voltage for sputter deposited films from a single target versus two targets is shown in Figure 4.4. As described above, the brightness values have been normalized for a ZnS:TbOF layer thickness of 1μm since the films deposited from two separate ZnS and TbOF targets versus a single target were 9000Å and 10400 Å thick, respectively. The data in Figure 4.4 showed that the as deposited EL brightness of films sputter deposited from a single target was much larger than that from a film deposited from two separate targets. The B_{40} for the film from a single target was 89 cd/m², while the comparable value for films deposited from separate targets was 44 cd/m². The Tb^{+3}

concentration in the deposited films was ~4 mole %, i.e. much higher than that of the

target (1.5 mole % of Tb) due to the lower sticking coefficient for ZnS versus Tb.
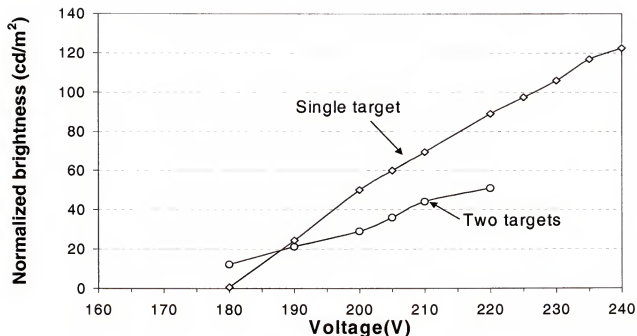
Figure 4.4 Comparison of EL brightness (normalized to a thickness of 1 μm) for films sputter deposited from either a single or from two targets.

4.3.2.2 Thickness change

As will be discussed below, it is believed that negative ion resputtering (NIR) and

damage led to the lower quality of crystallinity in the case of films deposited from two

separate ZnS and TbOF targets. For sputter deposition when NIR effects are negligible,

the center region of the planar magnetron sputter deposited films is thicker than the edge

regions. For a single ZnS:TbOF target, the thickness in the center region (10800Å) is

slightly more than the edge region (10000Å-Table 4-1). If the rate of negative ion

resputtering is significant relative to the deposition rate, the center region will be thinner

than the edge region. When high power (>70W) was applied to the pure TbOF target in a

deposition using two sources, the center of the film was thinner (5800Å) than the edge

region (9050Å), as shown in Table 4.1. This is clear evidence for significant negative ion

resputtering in the case of sputter deposition from two targets, one of them being pure

TbOF.

Table 4.1 Thickness variation in the films deposited from two separate ZnS and TbOF
targets and a single ZnS:TbOF target.

	Thickness in the center	Thickness at the edge
Two target(ZnS and TbOF)	5800Å	9500Å
Single ZnS:TbOF target	10800Å	10000Å

4.3.2.3 XRD

The Full Width Half Maximum (FWHM) of the 28.5° XRD peak was used to

characterize the crystallinity of the ZnS:TbOF thin films. Zinc sulfide has two observed

crystal structures, cubic and hexagonal [99]. The 28.5° XRD peak is an overlapped peak

from the (111) plane of the cubic phase and the (002) plane of the hexagonal phase. The

FWHM value for this peak was 0.51° from films deposited from a single target, and 0.61°

from films deposited from two separate targets. Thus the as-deposited crystallinity of

ZnS:TbOF films from a single target was better than that from two separate targets.

4.3.2.4 TEM

Plane view transmission electron microscopy (TEM) photographs from

ZnS:TbOF films deposited from a single versus two sources are shown in Fig.4.5a and b,

respectively. While the grains in both cases are very indistinct, the microstructure and

grain size is better defined and larger in films from a single versus two targets.

0.1μm

(a)   (b)
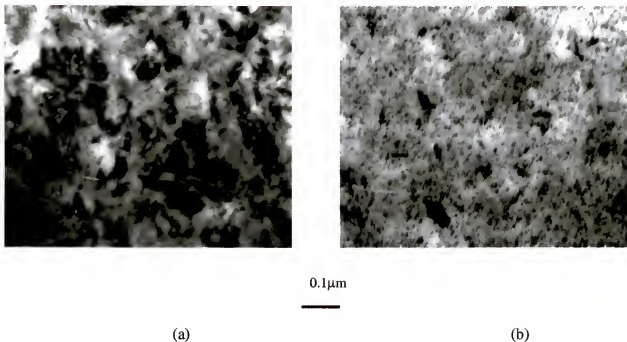
Figure 4.5 Plan-view TEM micrographs of as-deposited ZnS:TbOF thin films from a) a single target, and b) from two targets. Note the more clearly defined microstructure in micrograph a) for the film deposited from a single target.

4.4 Discussion

The better EL brightness of films from a single ZnS:TbOF versus from two

separate ZnS and TbOF targets correlates with better crystallinity and microstructure in

the films. Poor crystallinity and microstructure are known to have negative effects on

electroluminescent properties [99,100]. Reduced brightness is expected since EL

emission results from impact excitation of Tb by ballistic (hot) electrons. Electrons will

lose energy in scattering by microstructural defects and grain boundaries, which will reduce the fraction of electrons with sufficient energy for impact excitation. Therefore, films with good crystal quality generally have hotter electron transport and better electroluminescent brightness and efficiency.

The poor crystallinity of films deposited using two separate ZnS and TbOF sources is probably due to negative ion resputtering (NIR) effects. It has been reported by Honig [101] that negative ions, such as Cl^-, F^-, Br^-, O^-, OH^-, O_2^- and S^- form during sputtering. Hanak et al. [102] reported that in highly ionic materials such as TbF_3 and $TbCl_3$, negative ions not only reduce film deposition rates, but also may lead to substrate etching. Negative ion resputtering occurs when an electron is removed from an electropositive element (at an energy cost of the ionization potential, IP), and then combined with an electronegative element (at an energy gain of the electron affinity, EA) to form a negative ion. Because a negative charge occurs on the target during RF sputtering [101], this negative ion is accelerated towards the substrate and may cause both damage in the depositing film, and even cause resputtering. As discussed below, after acceleration it is possible for the negative ion to be scattered and neutralized. However, the resulting neutral atom (molecule) may retain a large amount of kinetic energy and result in damage or sputtering when it strikes the substrate with a deposited film. Any sputtering will reduce the growth rate for the thin film. If the rate of sputter removal is greater than the deposition rate, etching of the substrate may result.

Cuomo et al. [103] developed a model to predict formation of negative ions. According to this model, negative ion will form if IP-EA is less than 3.4eV. While this simple predictive tool has proven valuable, resputtering has been shown to be affected by

many other sputtering parameters such as the R.F. power, substrate-target distance, total pressure, and sputtering gas composition [104,105]. Therefore for many compounds where IP-EA is larger than 3.4eV, negative ion resputtering has been reported [106,107]. Kester and Messier [105] have discussed modification of the microstructure and film morphology even in the case where the resputter rate is significantly lower than the deposition rate.

In the case of two separate targets, the ionization potential of Tb is 5.98eV and the electron affinity of oxygen and fluorine is 1.47eV and 3.45eV, respectively. Therefore $IP_{Tb} - EA_{O \, or \, F}$ is 4.51eV and 2.53eV for O and F in the TbOF target, respectively. This is much smaller than the value of 7.32eV for Zn (IP = 9.39eV) and S (EA = 2.07eV). Therefore a NIR effect is expected from the TbOF target and not from the ZnS target.

In the case of a single ZnS:TbOF target, the probability of formation of O^- and F^- is mainly dependent on the IP of Zn and EA of O or F because the Tb atomic concentration is so low. The value of $IP_{Zn} - EA_{O \, or \, F}$ is 7.92eV or 5.94eV, respectively. These values are much larger than the values for the TbOF target, which strongly suggests that any NIR effect from the O^- and F^- in single ZnS:TbOF target should be much smaller than NIR from a TbOF target.

Another factor that affects negative ion resputtering is the amount of acceleration experienced by the negative ion (O^- or F^-). To achieve high energy, they must remain ionized over a region where significant voltage drop occurs in the plasma. The amount of acceleration of the negative ion is controlled by the distance between gas phase collisions. In this study, 20mTorr Ar gas was used for sputtering, with the distance between the target and substrate being 5 cm and a substrate temperature of 160°C. Based

on the kinetic theory of gas, the mean free path between Ar-Ar interactions, λ, is about 0.3cm for a temperature of 300K. This value was calculated from $\lambda = 1/\sqrt{2}n\pi d_o^2$ (where n = gas density, and d_o = diameter of Ar molecule = 3.64×10^{-8} cm^2). However, if the sputtered ions have kinetic energy, the mean free path increases. Harper et al. [108] reported that the mean free path of the sputtered ions is over 1cm for energies of about ten electron volts. Therefore the negative ions may be accelerated through the dark space without losing their negative charge [108]. When these negative ions enter the plasma, they lose the attached electrons because of inelastic collisions with other electrons and ions, resulting in a beam of energetic neutrals which may strike the substrate [108] causing damage or sputtering.

4.5 Summary

Thin film ZnS:TbOF electroluminescent (EL) phosphors were R.F. plasma magnetron sputter deposited from either a single pressed powder ZnS:TbOF (1.5 mole % of Tb) target, or two separate sources using a CVD grown, undoped ZnS target and a TbOF pressed powder target. The films deposited from two separate ZnS and TbOF targets exhibited poor crystallinity and smaller grain size versus films from a single target, due to negative ion resputtering (NIR) effect. Thin films deposited from the single ZnS:TbOF target showed much higher brightness (B_{40} = 89 cd/m^2) than thin films deposited from two separate ZnS and TbOF targets (B_{40} = 44 cd/m^2). A concentration of 3~4 mole % Tb^{+3} resulted in the best brightness and the emission spectrum was not significantly changed with increasing Tb^{+3} concentrations.

CHAPTER 5
THE EFFECT OF SPUTTERING GASES ON THE ZnS:Tb THIN FILM DEPOSITION

5.1 The Effect of He Gas

5.1.1 Introduction

It was reported by Okamoto et al. [96] that the He gas added to Ar sputtering gas improve the brightness through improved crystallinity. In contrast, Xian et al. [109] reported that He gas addition to Ar sputtering gas does not significant affect the crystallinity of ZnS:Mn thin film. Therefore, it is still controversial whether He addition in Ar can improve the EL performance. It is already known that improved crystallinty can reduce nonradiative recombination [99,100]. In this section, we will report on the effects of He addition to Ar on the brightness of EL device and the crystallinity of the film.

5.1.2 Experimental

All films were deposited using a single ZnS:TbOF target. Half cell structures were used to compare the EL brightness. All the other experimental parameters are the same as described in chapter 3 except the sputtering gas composition. The total pressure was fixed at 20mTorr. The baseline pressure of the system is 1×10^{-6} Torr. To control the He, the flow rate was adjusted to reach the desired He partial pressure. For example, for 40% He/60% Ar, the He gas flow rate was adjusted to reach 8mTorr which is 40% of the total pressure of 20mTorr. Then using Ar, the total gas pressure was increased from 8mTorr to 20mTorr.

5.1.3 Results

5.1.3.1 Growth rate

The growth rate is affected by changes in the sputtering gases because the sputtering yield is a function of the incident ion mass. According to reference [110], the sputter yield of He is negligible compared to the sputter yield of Ar. Figure 5.1 shows the changes in growth rate as the He/Ar gas ratio changes. Considering the ion mass effect, the growth rate is expected to decrease in proportional to the He gas ratio. Even though the growth rate consistently decreases as the He gas ratio increases, the decrease is just from 114 Å/min to 86 Å/min (about 25%) as the He gas ratio increases from 0% to 70%. In other words, the growth rate was decreased just 25% by a 70% decrease of Ar gas. Clearly this does not agree with ion mass model of sputter yield.

This discrepancy between the decrease of the film growth rate and the decrease of the Ar gas percentage seems to be due to higher secondary electron yield from He ion. The secondary electron yield emitted from the molybdenum target surface when the ionized He and Ar gas hit the target surface is given at figure 5.2 [110]. The data of figure 5.2 shows the coefficient of secondary emission of electrons by helium ions is over 3 times larger than that of Ar ions for molybdenum. The larger secondary electron emission by He ions increases the population of electrons near the target surface and eventually increases the possibility of the ionization of Ar gas. Even though the total amount of Ar gas decreases 70%, the number of total ionized Ar gas and the film growth rate do not decrease as much as the decrease of the total Ar gas.
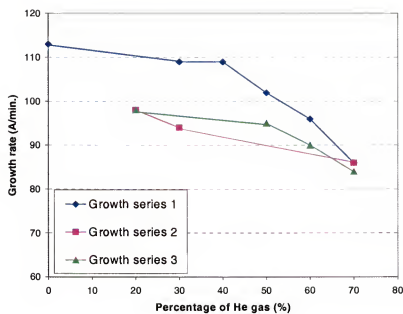
Figure 5.1 Growth rate change as He gas ratio changes
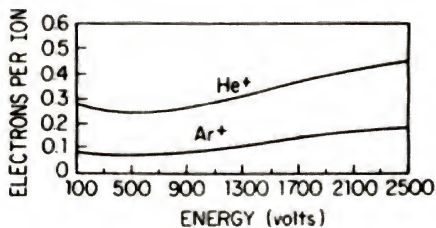
Figure 5.2 Coefficiency of secondary emission of electrons by argon and helium ions for molybdenum [110].

Another possibility is the scattering of sputtered species between the target and substrate. The atomic size of the He is much smaller than the Ar atomic size. Therefore, as the percentage of He gas increases, the scattering possibility of sputtered species decreases. These two factors have positive effects on the film growth rate even though the partial pressure of Ar decreases to 30% of the total gas pressure.

5.1.3.2 XRD analysis
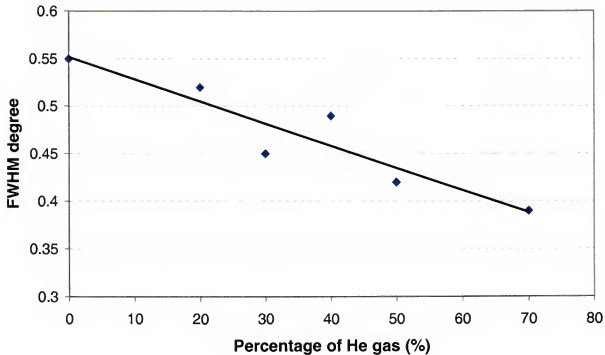
Figure 5.3 FWHM of 28.5° XRD peak (cubic (111) and hexagonal (002) planes) versus the percentage of He gas.

The FWHM change of the 28.5° XRD peak that results from the overlapped peaks from cubic (111) and hexagonal (002) planes as shown in Figure 5.3. The FWHM value

for this peak decreased from 0.55° to 0.39° as the He concentration increased from 0% to 70%, suggesting that the crystallinity of ZnS:TbOF films is improved by increasing the percentage of He gas.

5.1.3.3 EL properties

Figure 5.4 shows the brightness decrease with increasing the percentage of He gas, even though the crystallinity is improved as shown in Figure 5.3. The brightness value decreased from 64 cd/m^2 at 100 % Ar to 45 – 54 cd/m^2 with 40 % Ar. By linear least square fit of the brightness versus percent He gas, the brightness decreased about 30% when the partial pressure of Ar decreases from 100% to 30%.
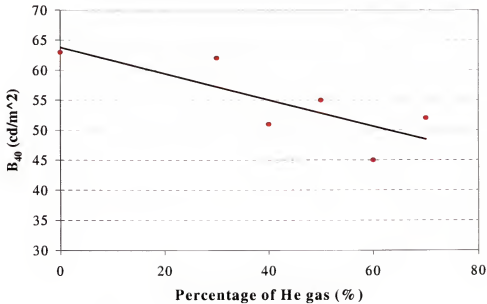
Figure 5.4 The EL brightness versus percentage of He in the Ar/He sputter ambient.

5.1.3.4 SEM and AFM

One of the reasons for the brightness decrease is changes in the surface roughness.

The root mean square (RMS) surface roughness measured by atomic force microscopy

(AFM) was 5.2 – 6.7 nm for films deposited with 0 to 50% He, but this roughness

decreased to 4.2 – 4.6 nm for films deposited with 60 –70 % He, as shown in figure 5.5

and 5.6. As discussed in section 2.3.5, a rougher surface has a better outcoupling

efficiency. The films deposited with 60 –70 % He gas has a smoother surface. Figure 5.5

shows an AFM line scan of film surfaces deposited with different sputtering gas

composition. These line scans show that surface roughness decreases as the He

concentration increases. A plot of RMS surface roughness versus the He concentration is

given at figure 5.6.

He 0% : R_{ms} -- 6.7nm   He 20% : R_{ms} -- 6.2nm

He 60% : R_{ms} -- 4.7nm   He 70% : R_{ms} -- 4.3nm
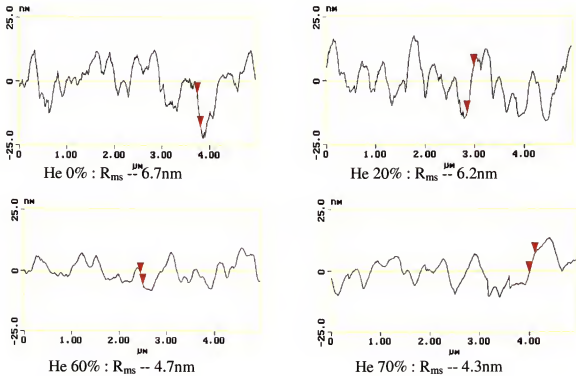
Figure 5.5 AFM line profile of the surface of ZnS:TbOF deposited with various
concentrations of He and Ar. The RMS roughness for the surface is also shown.
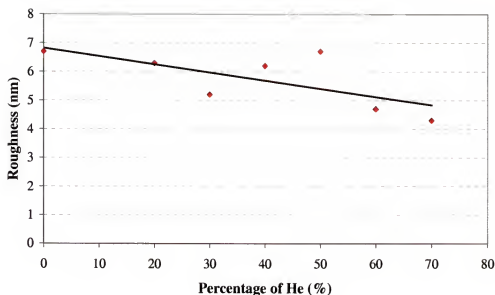
Figure 5.6 RMS surface roughness from AFM versus percentage of He in the Ar/He sputter gas (The straight line is a linear least squares fit).

      This decreased surface roughness as the percentage of He increases is also evident from SEM photomicrographs of the films. Contrast in SEM micrographs results from variation in the secondary electron emission of the surface. Therefore as the surface becomes smoother, the contrast in SEM is weaker. As shown in Figure 5.7, the surface morphology contrast of the film deposited with 70% He is weaker than the film deposited with 0% He.

He : 0%

He : 40%

He : 60%

He : 70%
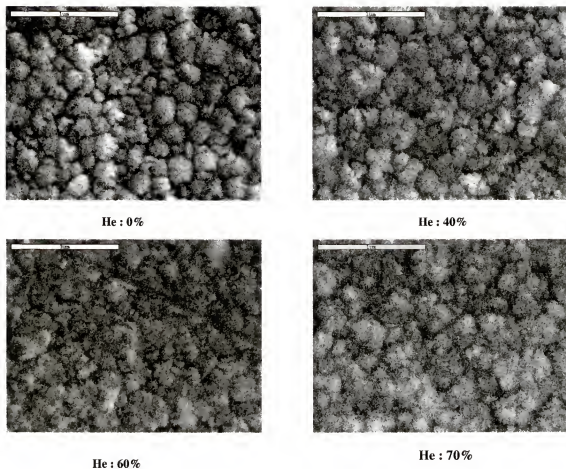
Figure 5.7 SEM photomicrographs showing the surface morphology of films deposited using various concentrations of He in the He/Ar sputter gas. Note the apparent reduction of roughness at higher He concentrations, in agreement with AFM data.

5.1.3.5 Dielectric constant

The dielectric constant of the ZnS film also increased from values of 12 to 15 for

0 to 50 % He, to values of 16 to 19 for 60 to 70 % He (figure 5.8). This dielectric

constant change also affects the device performance as discussed in Section 2.5.2.1.

Because the actual voltage dropped across the phosphor layer, from the equivalent circuit,

is expressed by:

$$V_{EL,f} = \frac{C_I}{C_I + C_{EL}} V_{th} \cdot$$ (4-1)

The voltage across the phosphor layer (V_{EL}) decreases as the capacitance of the phosphor layer (C_{EL}) increases. The same total voltage is applied.
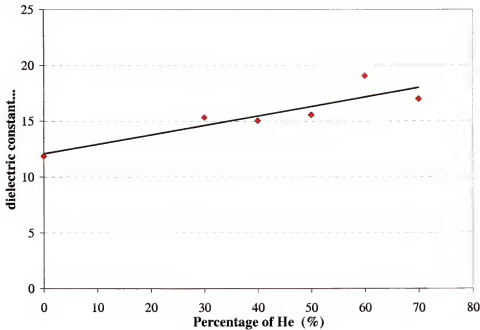
Figure 5.8 Dielectric constant of as-deposited film versus % He in sputter gas.

5.1.4 Discussion

As shown in Figure 5.2, the crystallinity of ZnS:TbOF film deposited at higher He concentrations in a He/Ar mixture is improved. 'Crystallinity' is a general term which indicates the degree of orderly atomic arrangement, and better crystallinity is presumed to correlate with less nonradiative recombination. Therefore, all factors, such as point defects, dislocation, twins, and grain boundaries reduce orderliness of the atomic

arrangement in the lattice and deteriorate crystallinity. The crystallinity improvement by adding He gas to the sputtering gas can be understood in terms of the size and mass of He ions. As described in section 5.1.3.1, even though He gas is added to Ar, most sputtering will still result from Ar ions because He ions have such small mass that the sputter yield is negligible compared to Ar ion [110]. The variation of sputtering yield with atomic number of the bombarding ion for 45keV bombardment of copper, silver, and tantalum targets is shown in figure 5.9. It shows clearly that the noble ions give the highest sputtering yields while elements from the center columns of the periodic chart (Al, Ti, Si, Zr) have the lowest yields and the elements which are lighter than carbon have almost negligible sputtering yield.
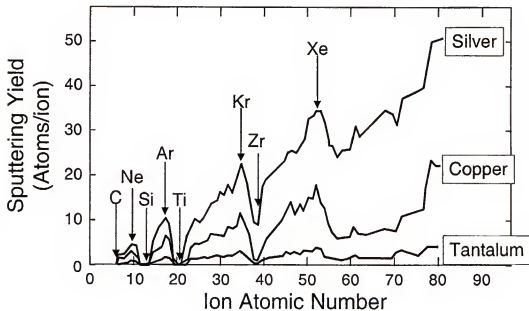
Figure 5.9 Variation of sputtering yield with atomic number of the bombarding ion for 45KeV bombardment of copper, silver, and tantalum targets [110].

Therefore, it can be assumed that the kinetic energy of sputtered species such as Zn, S or their clusters is independent on the gas composition because most of the sputtered species are sputtered by Ar ions. However, considering the kinetic factors of scattering, energy is transferred between the two particles. The energy transfer or kinematics in elastic collisions between two isolated particles can be solved by applying the principles of conservation of energy and momentum. For an incident energetic particle of mass M_1, the values of the velocity and energy are v and E_o ($E_o = \frac{1}{2} M_1 v^2$) while the target atom of mass M_2 is at rest. After the collision, the values of the velocities v_1 and v_2 and energies E_1 and E_2 of the projectile and target atoms are determined by the scattering angle θ and recoil angle ϕ. (Figure 5.10)
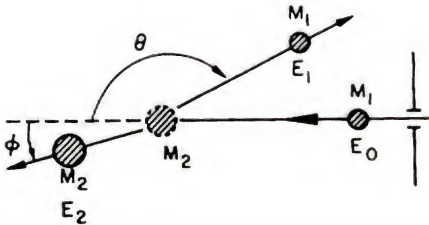
Figure 5.10 Schematic representation of an elastic collision between a projectile of mass M_1, velocity v, and energy E_o and a target mass M_2 which is initially at rest [111].

The energy transferred to the stationary atom (E_2) is described by

$$\frac{E_2}{E_1} = \frac{4M_1M_2}{(M_1 + M_2)^2} \cos^2\varphi \qquad (4\text{-}2)$$

As the atomic mass of the sputtering gas is increased, the energy loss of the sputtered species is larger. Therefore, sputtered species such as Zn ion or S ion lose more energy by a gas phase collision with Ar than He gas. Under the same gas pressure, the number of gas molecules is the same in spite of different gas composition, and the total collision probability between the sputtered species such as Zn ion or S ion and sputtering gas such as Ar or He is also the same. However, as the percentage of Ar decreases and the percentage of He increases, the collision probability between the sputtered species and Ar gas decreases and the collision probability between the sputtered species and He gas increases. Therefore, the sputtered species can arrive at the substrate with higher kinetic energy as the percentage of He increases. High kinetic energy for the incident ion flux results in high mobility when they arrive on the substrate resulting in motion on the substrate surface to find a more stable position. This will improve the crystallinity, and reduce surface roughness of the deposited films.

As mentioned already, poor crystallinity and microstructure are known to have negative effects on electroluminescent properties [99, 100] by reducing the brightness of ACTFEL devices by reduced impact excitation of Tb by cooler ballistic electrons. Electrons will lose energy in collisions with microstructural defects and grain boundaries, which will reduce the fraction of electrons with sufficient energy for impact excitation. Therefore, improved crystallinity should improve the excitation efficiency. In addition, radiative emission efficiency will also be improved by the better crystallinity because the defect energy levels can act as non-radiative emission paths. But, the actual brightness of EL device decreased as the He gas content increased. With respect to the effect of He

sputtering gas, the outcoupling efficiency depends on the amount of light generated in the phosphor layer which escape from the film. This amount is dependent on the surface roughness and reflective index of phosphor layer. In this study, it is assumed that the critical escape angle is same for all the films because the composition is the same. As shown in section 5.1.3.4, the surface roughness decreased as the He gas content increases. Figure 5.6 shows that the surface roughness decreased 30% as He increased from 0 to 70%. This should reduce outcoupling and reduce the EL brightness [112-118].

Another factor in EL brightness is excitation efficiency. The excitation efficiency depends mainly on the fraction of electrons that have enough energy to impact excite the luminescent center. The fraction of hot electrons is critically dependent on acceleration field in the phosphor layer, which can be understood by the simple equivalent circuit of an EL device as shown in Figure 2.11b.

The total applied electrical potential (V_a) is divided between the EL device and dielectric layer. The electric field on the EL phosphor (V_{EL}) and the electric field on the dielectric layer (V_l) are divided by the ratio of the capacitance of each layer as follows:

$$V_{EL} = \frac{C_l}{C_l + C_{EL}} V_a (under\ V_{th}) \qquad (4-3)$$

$$V_{EL.f} = \frac{C_l}{C_l + C_{EL}} V_{th}\ (over\ V_{th}) \qquad (4-4)$$

C_{EL} represents the capacitance of the phosphor layer and C_l represents the capacitance of the dielectric layer. According to this equation, an increase of the capacitance of phosphor layer decreases the voltage across the phosphor layer. From the simple mathematical calculation, it is possible to predict the actual voltage across each layer. First, the capacitance value can be calculated from

$$C = \frac{\varepsilon_0 \varepsilon_r A}{d} \qquad (4\text{-}5)$$

ε_0: the dielectric constant of vacuum (8.854×10^{-14} F/cm), ε_r: the relative

dielectric constant, A : the area of the dot contact (0.079 cm^2), d the thickness of the

phosphor layer (1μm) and dielectric film (0.2 μm).

The relative dielectric constant of the dielectric layer is about 18, as is known

from the literature [15], and the relative dielectric constant of the measured phosphor

layer ranges from 12 to 17. Therefore, the capacitances of each layer are as follows (for

the range of phosphor dielectric constant):

$$C_{ATO} = 6.3 \text{ nF } (\varepsilon_r = 18) \qquad (4\text{-}6)$$

$$C_{phos} = 0.84 \text{ nF } (\varepsilon_r = 12) \qquad (4\text{-}7)$$

$$C_{phos} = 1.19 \text{ nF } (\varepsilon_r = 17). \qquad (4\text{-}8)$$

From equation (4-4), the range of voltage across the phosphor layer at a typical

threshold voltage (160V) is

$$V_{EL} = 141 \text{ V } (\varepsilon_r = 12) \qquad (4\text{-}9)$$

$$V_{EL} = 135 \text{ V } (\varepsilon_r = 17). \qquad (4\text{-}10)$$

This calculation shows that for an external voltage of 200V, the actual voltage

across the phosphor layer is just 135V to 141V depending on the dielectric constant of

the phosphor layer. Another example of the capacitance effect on the EL brightness is the

addition of an external capacitance that limits the applied voltage on the phosphor layer.

The capacitance of two capacitors connected in series is

$$C_{tot} = \frac{C_{bottom} \times C_{top}}{C_{bottom} + C_{top}} \qquad (4\text{-}11)$$

where C_{bottom} is the capacitance of the bottom dielectric layer (6.3 nF), and C_{top} is the capacitance of the additional external capacitor. Figure 5.11 shows the EL brightness decrease versus the external capacitor value.
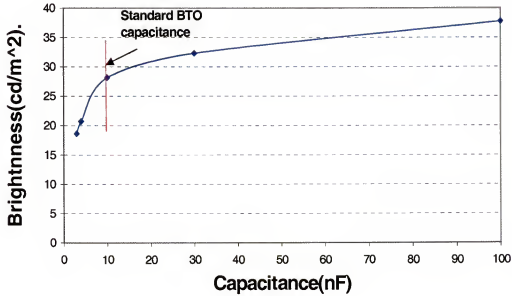
Figure 5.11 The effect of external capacitor device brightness.

5.1.5 Summary

ZnS:TbOF ACTFEL devices were also sputter-deposited from a single pressed powder ZnS:TbOF (1.5 mole % of Tb) target using a Ar + He mixed gas (The He gas concentration was changed from 0% to 70%) and annealed at 500°C for 60 minutes under a N_2 gas atmosphere. From X-ray diffraction, the FWHM of the cubic (111)/hexagonal (0002) plane in deposited films decreased from 0.55° (for Ar 100%) to 0.39° (for Ar 30

% + He 70 %) and the growth rate decreased about 25% as the He ratio increases from 0 to 70%. In spite of the improved crystallinity as indicated by the decreased FWHM degree, the brightness of the device decreases from 64 cd/m^2 for a pure Ar atmosphere to 45-54 cd/m^2 at 60-70% He gas concentrations. This brightness decrease is attributed to an increased dielectric constant (from 12 for pure Ar to 17 at 70 % He) and decreased RMS surface roughness (from 6.7 nm for pure Ar to 4.3 nm at 70 % He) of the deposited film.

5.2 The Effect of Oxygen Gas

5.2.1 Introduction

Okamoto et al. [95] studied the effect of oxygen doping in ZnS:TbF$_x$ thin film electroluminescent (EL) devices. They obtained the highest brightness when S/Zn, F/Tb, and O/Tb atomic ratios were around unity. From this analysis, they suggested that the Tb and O acted as substitutional impurities with the Tb assuming Zn sites, O assuming S sites in the ZnS lattice, and F occupied the interstitial site to form TbF complex. The Tb-O-F complex center was reported to yield high EL efficiency.

Noma et al. [119] reported that the oxygen doping in the ZnS:TbOF prepared by electron beam evaporation also improves the luminescence of EL devices and crystallinity of phosphor film. Bossche et al. [120] reported X-ray photoelectron spectroscopy (XPS) spectra of ZnS:TbF$_3$ and ZnS:TbOF thin films. There are two main peaks at about 1242 and 1277 eV originated from Tb^{+3} 3d$_{5/2}$ and 3d$_{3/2}$ energy levels, respectively, in TbF$_3$ powder (Figure 5.12).

These main peaks are accompanied by two small peaks situated at approximately 10 eV higher binding energy. They showed the possibility that Tb^{+4} is incorporated into

the ZnS layer. But it was reported by Wang et al. [121] that higher oxygen content in the ZnS:TbOF phosphor film (O/Tb > 1) reduced the brightness of the EL device. They showed that excess oxygen content could create deep hole traps which were detected by Deep Level Transient Spectroscopy (DLTS) (Figure 5.13). Also, a stronger H-O-H vibration peak from Fourier Transform Infrared Spectroscopy (FTIR) implies that there is a higher oxygen content in the phosphor layer, presumably from absorption of moisture which reduces luminescent brightness.
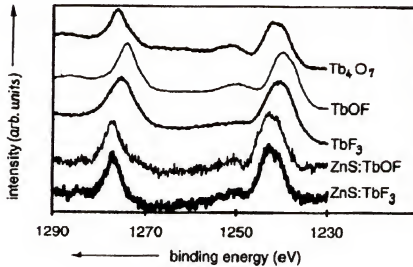
Figure 5.12 XPS spectra (Tb (3d) electrons) from powder Tb_4O_7, TbOF, TbF_3, and thin films of ZnS:TbOF and ZnS:TbF_3 [120].

In this section, the change of brightness of films deposited from a ZnS:TbF_3 target in Ar + O_2 atmospheres will be measured and discussed.

5.2.2 Experimental

Both a ZnS:TbOF (1.5 mole %) target and a ZnS:TbF$_3$ (1.5 mole %) target are used in this study. The oxygen concentration in the ZnS:Tb films is controlled by the oxygen partial pressure. The ultimate base pressure of sputtering system is $< 3.0 \times 10^{-6}$ Torr and the oxygen partial pressure is controlled from 6.0×10^{-6} Torr to 1.6×10^{-5} Torr.
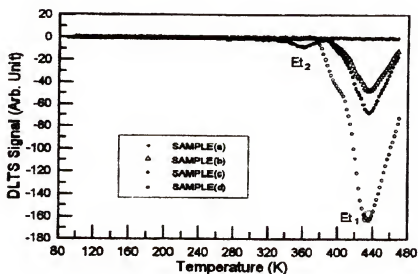
Figure 5.13 DLTS signals of different oxygen doping in ZnS:TbOF phosphor layer. The O/Tb ratio for samples a), b), c) and d) are 1.0, 1.2, 1.5 and 2.8 respectively [121].

5.2.3 Results

5.2.3.1 EL properties of ZnS:TbF$_3$

The EL brightness of films deposited from a ZnS:TbF$_3$ target (1.5 mole %) shows lower brightness than films deposited from the ZnS:TbOF (1.5 mole %) target in the as-deposited condition. Typically the as-deposited B$_{40}$ of films from a ZnS:TbF$_3$ target is 40 – 50 cd/m^2 compared to 60 – 70 cd/m^2 for films deposited from a ZnS:TbOF (1.5 mole %) target. However, the brightness after annealing is comparable for films from either a

ZnS:TbF$_3$ target or a ZnS:TbOF target. The highest B$_{40}$ of an annealed ZnS:TbF$_3$ film is

84 - 93 cd/m^2 after annealing for 60 minutes at 400°C. In the case of films deposited from

the ZnS:TbOF target, the highest B$_{40}$ is obtained after annealing for 60 minutes at 500°C

and the typical brightness is 70 – 90 cd/m^2. Figure 5.14 shows the brightness change

versus annealing temperature from ZnS:TbF$_3$ films. Annealed films deposited from

ZnS:TbF$_3$ target gives about 100% improvement in brightness compared to about 20 –

30% improvement in brightness for annealing of films deposited from ZnS:TbOF target.
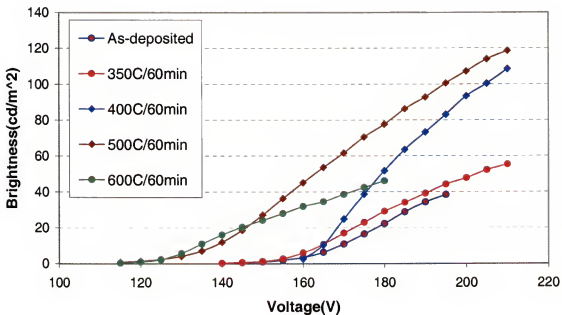
Figure 5.14 Brightness versus voltage for various annealing temperature of films
deposited from a ZnS:TbF$_3$ target.

5.2.3.2 EL properties of ZnS:TbF$_3$ with O$_2$ addition to the sputtering gas

Addition of a small amount of oxygen during sputter deposition of a ZnS:TbF$_3$

thin film affects the brightness after annealing for 60 minutes at 400°C. The brightness

versus oxygen concentration in the film is plotted in Figure 5.15 The relative oxygen

concentration was calculated from the intensity of ^{18}O and ^{96}ZnS in SIMS analysis. This plot shows clearly that the brightness depends on the oxygen concentration. The oxygen concentration in the brightest films was measured by Auger electron spectroscopy (AES) to be ≈ 3.6 at. %.
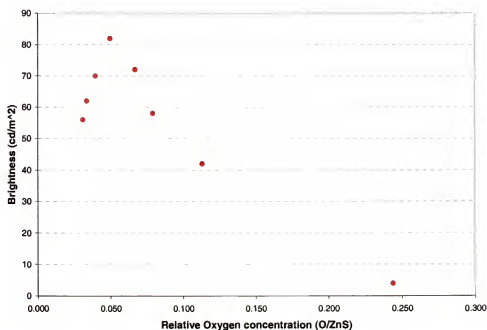
Figure 5.15 The brightness versus oxygen concentration in ZnS:TbF$_3$ thin films after annealing for 60minutes at 400°C.

The relative AES peak intensity of O/ZnS in the ZnS:TbOF film was $\approx 0.08 - 0.1$ range. This relative oxygen peak intensity is higher than the optimum oxygen level as shown in figure 5.15. However, the actual brightness is much higher from ZnS:TbOF films than from ZnS:TbF$_3$ film that has similar oxygen concentrations. This means that the oxygen incorporation from targets doped with TbOF in deposited films is more effective in improving the EL brightness than is the use of oxygen background gas and a ZnS:TbF$_3$ target. In addition, additional oxygen incorporation from residual contaminant

gas during deposition must be avoided for the best brightness, because the amount of oxygen in the film from a TbOF target is normally above the optimum level. As shown in figure 5.15, for a comparable oxygen concentration range in films deposited from ZnS:TbOF targets, the brightness are about 30 – 50% below the maximum brightness.

5.2.3.3 XRD

The FWHM analysis and peak position shift of the 28.5° XRD peak that is an overlap peak from the c(111) plane and the h(002) plane versus oxygen concentration is shown in Figure 5.16. The relative peak intensity of oxygen (m/e = 18) versus ZnS (m/e = 96) peaks from SIMS analysis was normalized by the actual concentration measured by AES to obtain real oxygen concentration. The FWHM does not show much change from 0 to ≈ 8 at % in oxygen. However, it increases to 0.64° at 17.6 at % oxygen. A large FWHM generally indicates poor crystallinity. However, based on the lack of a clear trend to improved crystallinity over the range of O concentration where EL brightness changes dramatically, it is concluded that crystallinity improvement is not the main reason for brightness improvement with oxygen incorporation. Peak position for the c(111)/h(0001) peak is also shown in figure 5.16. The position shifts to higher angle when the oxygen concentration of the film increases. This means that the (111)/(0001) interplanar spacing is contracted by substitution of a small oxygen ion (ionic radius of 1.32 Å) onto the larger sulfur ion site (ionic radius of 1.84 Å).

5.2.3.4 PL emission

It was reported that the PL emission peak of $^5D_4 \rightarrow {}^7F_5$ has double peaks according to the crystal field around the Tb^{+3} ion [81]. Okamoto et al. [81] reported that the PL emission peak from TbF_3 powder has a maximum at 544nm while the emission peak from ZnS:Tb crystal was maximum at 552nm.
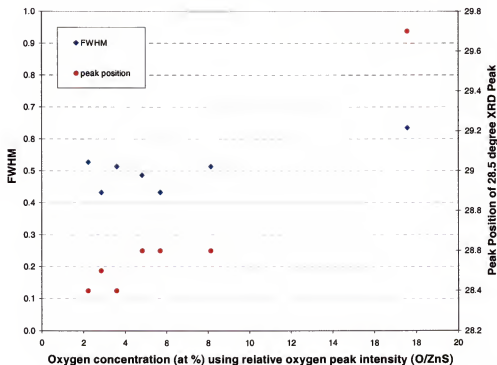
Figure 5.16 FWHM (left ordinate) and Bragg peak position (right ordinate) of the 28.5° XRD peak versus oxygen concentration from sputter deposition in Ar + O_2.

The PL spectra of the film deposited from ZnS:TbOF target, shown in Figure 5.17, has strong intensities at both 552nm and 544nm, but the intensity of 544nm is about 90% of the intensity of the 552nm peak. Double peaks are also observed in the PL spectrum from films deposited from a ZnS:TbF$_3$ target with O_2 in the sputter gas, and the 544nm peak is more intense than the 552nm peaks at all oxygen concentrations. (Figure 5.17).
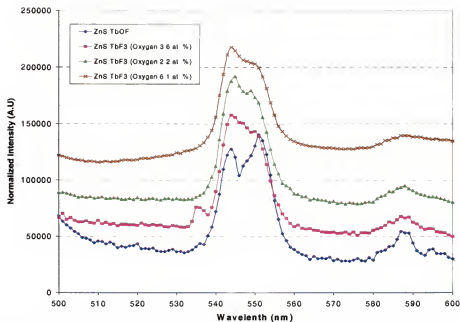
Figure 5.17 PL spectra of a film deposited from a ZnS:TbOF target, and from films deposited from a ZnS:TbF₃ target with different oxygen sputter gas concentrations.

The double PL peak shape from films deposited from a ZnS:TbOF or ZnS:TbF₃ target is similar to those shown in figure 2.24c and b. As described in section 2.6.2, the separation of $^5D_4 \rightarrow {}^7F_5$ transition peak into two peaks results from the crystal field around the Tb^{+3} ion. When the Tb ions are shielded by F ions, the peak at 544nm is stronger than the peak at 552nm. When Tb ions are affected by the crystal field of the ZnS lattice, the peak at 552nm is stronger than the peak at 544nm [79]. Therefore, crystal field effects on the Tb ions with F ions shielding is different when the films are deposited from ZnS:TbOF target versus ZnS:TbF₃ targets. Even when the films are deposited from a ZnS:TbF₃ target with an oxygen sputter gas, the shielding effect by the F ion does not change, even after annealing at 400°C.

5.2.3.5 Electrical and optical characterization

As shown figure 5.15, the EL brightness is significantly affected by the oxygen concentration in the deposited film. The oxygen concentration and the EL brightness are summarized at Table 5.1.

Table 5.1 EL brightness vs. oxygen concentration in films deposited from a $ZnS:TbF_3$ target with an oxygen partial pressure in the sputter gas.

Oxygen concentration (at. %)	B_{40} (cd/m^2)
2.2	**56**
2.4	62
2.9	70
3.6	**82**
4.8	72
5.7	58
8.1	**42**
17.6	4

To understand the effects of oxygen codoping on ZnS:Tb phosphors, it is necessary to characterize the factors that affect to the EL emission. These include the amount of conduction charge, excitation efficiency, radiative efficiency and outcoupling efficiency [40]. The three samples in table 5.1 whose data are reported with bold character are chosen for electrical characterization. These samples are 2.2 at. % (doped below the maximum; $B_{40} = 56$ cd/m^2), 3.6 at. % (optimum; $B_{40} = 82$ cd/m^2), and 8.1 at. % (excess doped; $B_{40} = 42$ cd/m^2) oxygen codoped film. The external conduction charge is

measured by Q-V data, and the internal charge is equal to the stored charge from Q(t) curves, at the point where the applied voltage is 0V due to rapid discharge of the device capacitance at the end of pulse. The definition of the excitation efficiency and radiative efficiency is given by Mach et al. [46] and described in detail in section 2.5.1.4.

5.2.3.5.1 Q-V Curves and External Conduction Charge

The Q-V curve of the oxygen codoped films are shown in figure 5.19 at V_{40}. Their external conduction charge is summarized in table 5.2.
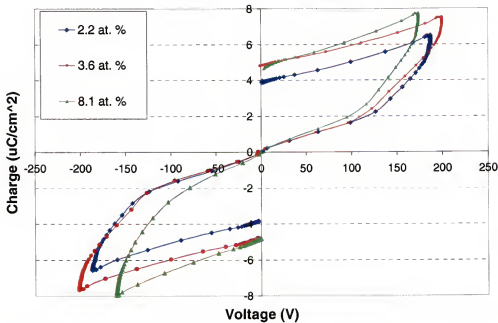
Figure 5.18 Q-V curve at V_{40} from oxygen codoped film with different oxygen concentrations.

Table 5.2 External conduction charge versus voltage above threshold for different oxygen concentrations.

Conduction charge Voltage	Q_{ext} (2.2 at.% O)	Q_{ext} (3.6 at.% O)	Q_{ext} (8.1 at.% O)
V_{10}	0.6 (μC/cm^2)	2.0 (μC/cm^2)	1.4 (μC/cm^2)
V_{20}	1.3	3.3	2.5
V_{30}	2.9	4.5	4.3
V_{40}	4.5	5.6	5.2

As shown in figure 5.18 and table 5.2, the ZnS:TbF$_3$ film with low oxygen concentration (2.2 at.%) shows significantly lower conduction charge density as compared to the other two films. In comparison to the film with 2.2 at.% oxygen, the film with 3.6 at.% oxygen concentration film shows 55% and 24% larger conduction charge density at V_{30} and V_{40}, respectively.

5.2.3.5.2 Internal Charge from Q(t) Curves

The evaluation of internal charge, Q_{int}, from a plot of external charge, Q_{ext}, versus time is illustrated in figure 5.19. The internal charge for ZnS:TbF$_3$ films with different oxygen concentration are listed in Table 5.3. Each value is averaged for Al+ and Al-polarity since the variation with polarity is less than ±5%. The internal charge shown in table 5.3 displays the same trend as external charge as reported in the previous section. The internal charge for film with 3.6 at.% oxygen is 53% and 24% larger than for film with 2.2 at.% oxygen at V_{30} and V_{40}.
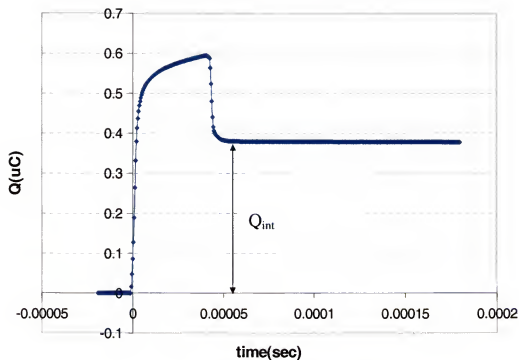
Figure 5.19 Determination of Q_{int} from Q_{ext} vs time data.

Table 5.3 Internal charge versus voltage above threshold for films with different oxygen concentrations.

Conduction charge Voltage	Q_{int} (2.2 at.% O)	Q_{int} (3.6 at % O)	Q_{int} (8.1 at % O)
V_{10}	0.050 (µC)	0.152 (µC)	0.14 (µC)
V_{20}	0.109	0.235	0.220
V_{30}	0.205	0.313	0.299
V_{40}	0.306	0.380	0.374

5.2.3.5.3 Excitation Efficiency

The excitation efficiency can be calculated from the maximum brightness in EL emission decay curves divided by the internal charge given at table 5.3. The calculated excitation efficiencies are given in table 5.4.

Table 5.4 Excitation efficiency of $ZnS:TbF_3$ films versus voltage above threshold with different oxygen concentrations.

Excitation Efficiency (A.U) Voltage	Q_{int} (2.2 at.% O)		Q_{int} (3.6 at % O)		Q_{int} (8.1 at % O)	
	Al+	Al-	Al+	Al-	Al+	Al-
V_{10}	0.031	0.019	0.025	0.022	0.026	0.006
V_{20}	0.029	0.023	0.024	0.021	0.021	0.008
V_{30}	**0.025**	**0.019**	**0.021**	**0.019**	**0.019**	**0.01**
V_{40}	**0.020**	**0.017**	**0.018**	**0.018**	**0.017**	**0.01**

In spite of the variation in excitation efficiency dependent upon the polarity of the voltage, the overall trend is that the excitation efficiency decreases at high oxygen concentration. There is no significant difference in excitation efficiency for 2.2 at. % versus 3.6 at. % oxygen films. Films with 8.1 at.% oxygen show a significant decrease in excitation efficiency.

5.2.3.5.4 Radiative Efficiency

Figure 5.20 shows EL emission decay curves, normalized for Al+ polarity, from three films with different oxygen concentrations. The radiative efficiencies are summarized in table 5.5 by integrating the EL emission intensity for each polarity.
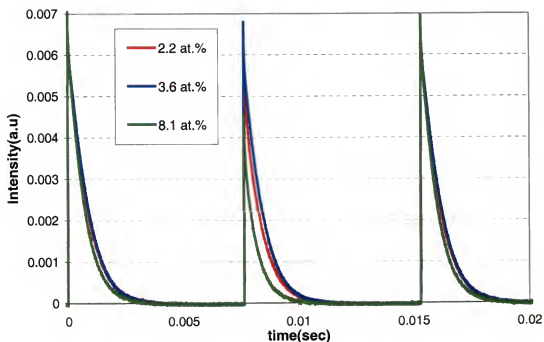
Figure 5.20 The EL emission decay curve of three different oxygen concentration films.

Table 5.5 Radiative efficiency of ZnS:TbF$_3$ films having different oxygen concentrations.

Oxygen concentration polarity	2.2 at.% O	3.6 at.% O	8.1 at.% O
Al+	0.50 (a.u)	0.51	0.43
Al-	0.42	0.45	0.31

As shown in table 5.5, the radiative efficiency of films with 2.2 at. % and 3.6 at.% oxygen are similar. However, the film with 8.1 at.% oxygen shows a significantly lower radiative emission efficiency. This decrease of radiative emission efficiency of highly oxygen doped film is due to the relatively fast emission decay as shown at figure 5.21.
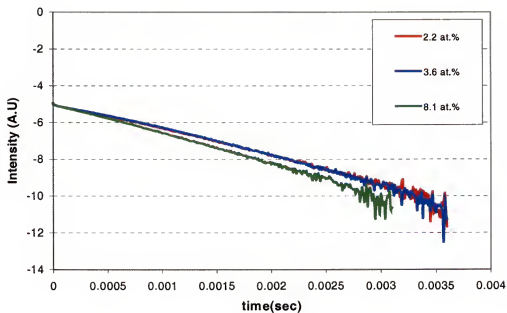
a)
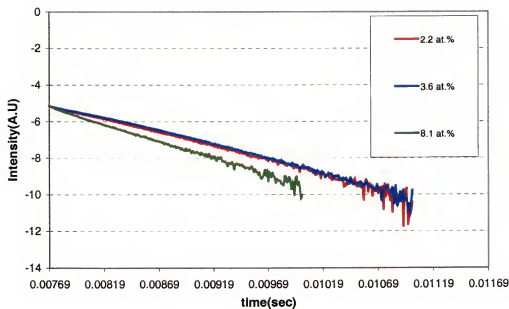
b)

Figure 5.21 EL emission intensity versus time after application of the voltage pulse for different oxygen concentrations in the films. a) Al+ polarity, and b) Al- polarity.

The characteristic time constants for an exponential fit to the time-resolved intensity data shown in figure 5.21 are shown in table 5.6. The decay constant for the film with 8.1 at.% O is $0.54 - 0.55$ms. For Al+ and Al- polarities, respectively, these decay constants are much small than the 0.68-0.75 ms and 0.71- 0.78 ms for films with 2.2 at.% and 3.6 at. % O.

Table 5.6 Characteristic emission decay time constant for films with different oxygen concentrations and voltage polarity.

Oxygen concentration polarity	2.2 at.% O	3.6 at.% O	8.1 at.% O
Al+	0.75 (ms)	0.78	0.54
Al-	0.68	0.71	0.55

5.2.4 Discussion

The presence of oxygen in the ZnS:Tb ACTFEL device is known to be an important factor that affects the device performance. However, the mechanism for the oxygen codoping effect was not known. In this study, the important physical processes of EL emission were evaluated by conduction charge, excitation of luminescent center, radiative emission of excited luminescent (see section 2.3). Data were reported above which allow an evaluation of these various factors in EL emission.

At 3.6 at.% oxygen, the amount of conduction charge is larger (53-55% at V_{30} and 24% at V_{40}) than for 3.6 at. % oxygen in the film. Since the B_{40} of 3.6 at. % film is 46% higher than the B_{40} of film with 2.2 at. % O, the increase of the conduction charge with an increase in oxygen is the main reason for improved brightness. However, the excitation and radiative efficiency do not increase as the oxygen content is increased

(table 5.4 and table 5.5). Therefore the increased conduction charge with increased oxygen suggests that the interface state densities between the bottom dielectric and the phosphor are increased by oxygen. One possible explanation for such an observation is that oxygen in the sputter gas may be ionized and accelerated to the substrate. The increased fluence of ionized oxygen on the interface could introduce more defect state that act as a source for conduction charge. On the other hand, excess oxygen codoping decreases the device brightness even though the conduction charge did not change significantly, as shown in table 5.3. Instead, both the excitation (28% at V_{30} and 23% at V_{40}) and radiative (24% at V_{40}) efficiencies were lower for film with 8.1 at.% O, and the B_{40} of the film with 8.1 at.% oxygen is 49% less that of the film with 3.6 at. % oxygen (42 cd/m^2 versus 82 cd/m^2). This 49% decrease in brightness is consistent with the 23%decrease in excitation efficiency and 24% decrease in radiative efficiency.

Even though the FWHM from XRD from the oxygen codoped films do not show significant change over the oxygen concentration range of 0 to 8%, the large FWHM value for 17.6 at.% oxygen indicates that codoping may affect the crystallinity of the ZnS:Tb film. In addition, the increase in the Bragg angle for the 28.5° XRD peak with an increase of oxygen (figure 5.16) indicates lattice distortion of ZnS because the ionic size of O^{-2} (1.32 Å) is much smaller than for S^{-2} (1.84 Å). Therefore, the lattice distortion caused by incorporation of smaller oxygen ion can introduce point defects such as vacancy or interstitial atoms. These defects can be responsible for the decreased excitation and radiative efficiencies.

5.2.5 Summary

To investigate the effects of oxygen incorporation in the ZnS:Tb,F, films were deposited from a ZnS:TbF$_3$ target and an oxygen flow was controlled by a leak valve. ZnS:Tb,F films show the best brightness (82 cd/m^2) at 3.6 at.% of oxygen concentration in the deposited film, with a very sharp drop off in brightness from either underdoping (56 cd/m^2 at 2.2 at.% oxygen) or overdoping (42 cd/m^2 at 8.1 at.% oxygen). The conduction charge calculated from charge (Q) versus voltage (V) and charge(Q) versus time(t) data show that the brightness improvement by oxygen incorporation can be attributed to an increased conduction charge. The conduction charge increased about 24% at V$_{40}$ upon increasing the oxygen concentration from 2.2 at. % to 3.6 at. %. The brightness decrease by oxygen overdoping is attributed to both a decreased excitation and a decreased radiative efficiency. The excitation efficiency decreased by 23% while the radiative efficiency decreased by 24% when the oxygen concentration increases from 3.6 at.% to 8.1 at.%.

CHAPTER 6
Ag, Cu, Ag + Cu, Ce CODOPING ON ZnS:TbOF

6.1 Introduction

Even though ZnS:TbOF shows the highest green luminance, its' brightness and efficiency are much lower than yellow emitting ZnS:Mn. So far the best reported brightness and efficiency of yellow EL emission from ZnS:Mn film are 572 cd/m^2 and 2 lm/W (at 60 Hz) [122] compared to 125 cd/m^2 and 0.5 lm/W for ZnS:Tb, O, F. The solubility of Tb^{+3} ion in ZnS is limited due to large ionic size of the Tb^{+3} (0.92Å) compared to Zn^{+2} (0.74Å). In addition, zinc vacancy point defect formation is expected because of the charge mismatch between Tb^{+3} and Zn^{+2}. Therefore, it is thought that the limited solubility of Tb^{+3} ion and point defects due to the charge mismatch between Tb^{+3} and Zn^{+2} limit the brightness and efficiency of ZnS:TbOF film.

In this study, codoping of ZnS:TbOF with Ag, Cu and Ce was investigated. Ag^{+1} and Cu^{+1} were studied for the possibility of acting as a charge compensator for Tb^{+3}, and they were expected to reduce the point defects in the ZnS:TbOF film [123]. In addition to Ag and Cu, Ce^{+3} ion was considered as an energy transfer center to Tb^{+3} ion, which was reported to occur in lamp phosphor such as LaPO$_4$; Ce,Tb [124] or Ce$_{1-x}$Tb$_x$MgAl$_{11}$O$_{19}$ [125]. Also energy transfer was reported from Ce to Er in a SrS lattice [41].

6.2 Experimental

For codoping, a Ag target (99.99% purity), Cu target (99.99% purity) or Ce$_2$O$_3$ (99.99% purity) target was used separately from the ZnS:TbOF (1.5 mole %) target.

ZnS:TbOF films were sputter deposited with a power of 120W in 20 mTorr Ar gas at a substrate temperature of 160°C. During deposition, the substrate was continuously rotated at a speed of about 11second per revolution. The R.F. power supply on the Ag, Cu or Ce_2O_3 target was operated in a pulsed mode with a variable duty cycle to control the doping concentrations. Ag codoping was accomplished at 5W applied peak power with 1 to 30% duty cycle. Cu codoping used 5W of peak power with 10 to 40% duty cycle or 10W with 4 to 32% duty cycle. For Ag + Cu codoping, two separate Cu and Ag targets were used with Ag codoping done at 5W, 2 to 8% duty cycle, and Cu codoping done at 5W, 2 to 20% duty cycle. For Ce codoping, the Ce_2O_3 target was operated at 3 to 5W with a 1 to 16% duty cycle. The ZnS:TbOF layer thickness was kept constant at 1 μm ± 10% for all devices. A 200nm aluminum top electrode was deposited by thermal evaporation onto the phosphor layer. All deposited films were annealed at 500°C for 60 minutes in N_2 gas ambient as described in section 3.

6.3 Results

6.3.1 EL Brightness Change by Cu, Ag, Cu + Ag, Ce Codoping

The EL brightness changes caused by Ag, Cu, Ag + Cu or Ce codoping are shown in figures 6.1a, b, c and d, respectively. Brightness versus voltage (B-V) data from uncodoped ZnS:TbOF films are plotted in each of these figures for a reference. Uncodoped ZnS:TbOF showed a brightness at 40V above threshold, B_{40}, and threshold voltage, V_{th}, which increased from 75 cd/m^2 to 86 cd/m^2 and decreased from 185 V to 170 V, respectively, for as-deposited versus films annealed at 500°C for 60 minutes.

Undoped ZnS:TbOF
as- deposited - B40 : 75 cd/m2
Undoped ZnS:TbOF
annealed (500C/60min.) - B40 : 86 cd/m2
ZnS:TbOF, Ag
as- deposited - B40 : 75 cd/m2
ZnS:TbOF, Ag
annealed (500C/60min.) - B40 : 55 cd/m2

a)

Undoped ZnS:TbOF
as-deposited - B40 : 75 cd/m2
Undoped ZnS:TbOF
annealed (500C/60min) - B40 : 86 cd/m2
ZnS:TbOF, Cu
as-deposited - B40 : 64 cd/m2
ZnS:TbOF, Cu
annealed (500C/60min) - B40 : 71 cd/m2
ZnS:TbOF, Cu
annealed (850C/5min)

b)

c)

d)
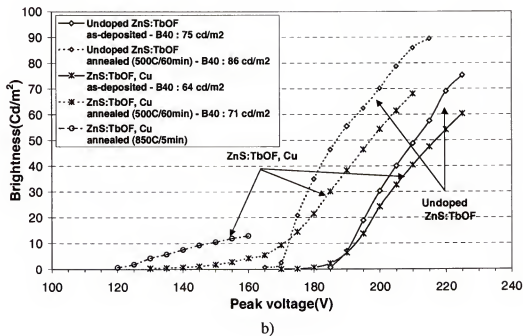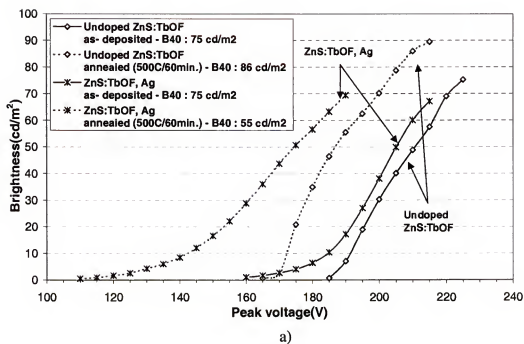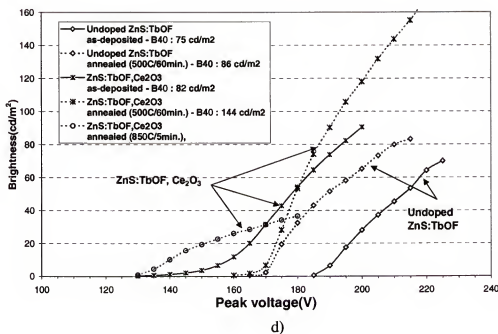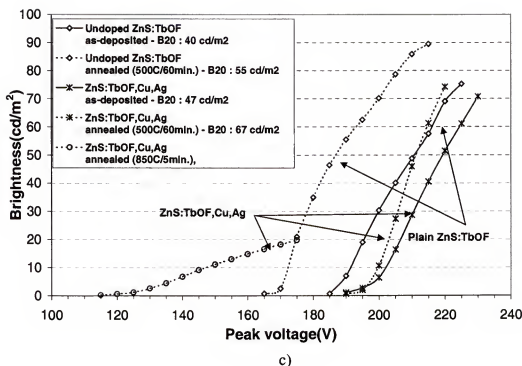
Figure 6.1 Brightness vs. voltage data from uncodoped ZnS:TbOF film and a) Ag codoped ZnS:TbOF, b) Cu codoped ZnS:TbOF, c) Ag + Cu codoped ZnS:TbOF, and d) Ce_2O_3 codoped ZnS:TbOF. Data both from as-deposited and annealed films are shown.
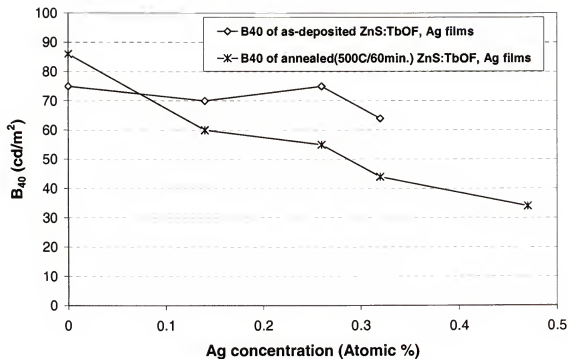
a)
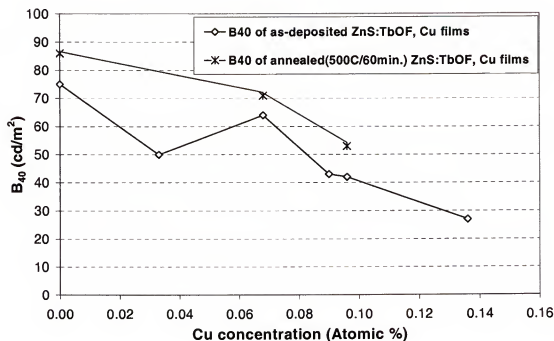
b)

Figure 6.2 Brightness (B_{40}) versus a) Ag concentration, or b) Cu concentration for as-deposited and annealed films.

Codoping with Ag did not significantly affect B_{40} or V_{th} for as-deposited film (B_{40} of 75 cd/m^2 and V_{th} of 180V, Figure 6.1a). After annealing at 500°C for 60 minutes, the brightness of the Ag codoped ZnS:TbOF film decreased from 75 cd/m^2 to 55 cd/m^2. The slope of the B-V curve at turn-on voltage also became lower, indicating a more "leaky" turn-on behavior as compared to uncodoped ZnS:TbOF film. The Ag concentration was increased from 0.14 at.% to 0.47 at.% by increasing the duty cycle of the Ag source from 1% to 30% at 5W. While the B_{40} of the as-deposited films remained constant within experimental error, the B_{40} of annealed (500°C for 60 minutes) films decreased from 86 cd/m^2 to 34 cd/m^2 as the Ag concentration increased from 0% to 0.47% (Figure 6.2a).

For the Cu codoped ZnS:TbOF films, the B_{40} increased and V_{th} decreased upon annealing at 500°C for 60 minutes, similar to uncodoped ZnS:TbOF films. As shown in Figure 6.2b, the B_{40} decreased from 86 cd/m^2 to 58 cd/m^2 and from 75 cd/m^2 to 28 cd/m^2 as the Cu concentration was increased from 0% to 0.14% for the as-deposited film or annealed films, respectively.

Although Ag or Cu codoping alone did not improve the EL brightness of the ZnS:TbOF thin films, the combination of Ag and Cu codoping did improve the brightness of both as-deposited films and annealed films. As shown in Figure 6.1c, B_{20} value of as-deposited or annealed (500°C for 60 minutes) films increased from 40 cd/m^2 to 47 cd/m^2 and from 55 cd/m^2 to 67 cd/m^2, respectively. In the Ag + Cu codoped ZnS:TbOF films, B_{20} is reported instead of B_{40} because half cell devices burned out prior to reaching B_{40}. The Ag concentration was varied from 0.14 at.% to 0.3 at.% and the Cu concentration was varied from 0.02 at.% to 0.05 at.% for the Ag + Cu codoped ZnS:TbOF films. These

concentrations ranges were chosen to be similar to those of Cu (between 0.03 at.% and 0.14 at.%) or Ag (0.14 at.% and 0.47 at.%) alone.

Ce codoping of ZnS:TbOF thin films did not significantly change the brightness of as-deposited film (75 cd/m^2 for uncodoped ZnS:TbOF film, 82 cd/m^2 for ZnS:TbOF, Ce film). However, after annealing at 500°C for 60 minutes, the brightness of Ce codoped films increased from 86 cd/m^2 to 144 cd/m^2, as shown in Figure 6.1d. The optimum Ce concentrations estimated from SIMS data was 1 - 10 ppm (parts per million).

6.3.2 XRD Analysis

The Full Width Half Maximum (FWHM) of the 28.5° XRD peak was used to help characterize the crystallinity of ZnS:TbOF thin films. The results are summarized in Table 6.1. For all films, XRD measurements were repeated two to four times, and the values in Table 6.1 are the average. The variation of FWHM for the same film was typically about ± 0.01°. The FWHM for uncodoped ZnS:TbOF films annealed at 500°C for 60 minutes is 0.42° and this value decreases from 0.42° to 0.37° as Ag concentration increases from 0.12 at % to 0.32 at %. To the contrary, Cu codoped ZnS:TbOF films show the same FWHM value as undoped ZnS:TbOF films after annealing for the concentration range used in this study. Therefore, only additions of Ag lead to improved crystallinity in Ag and in Ag + Cu codoped ZnS:TbOF film.

Table 6.1 Full Width Half Maximum (FWHM) of XRD peak at $2\theta=28.5^\circ$ for undoped, Ag codoped, Cu codoped, Ag + Cu codoped, and Ce_2O_3 codoped ZnS:TbOF films.

	As-deposited	Annealed (500°C, 60 min.)
Undoped ZnS:TbOF	0.46°	0.42°
Ag codoped ZnS:TbOF (0.12 at %)	0.51°	0.42°
Ag codoped ZnS:TbOF (0.22 at %)	0.46°	0.39°
Ag codoped ZnS:TbOF (0.32 at %)	0.50°	0.37°
Cu codoped ZnS:TbOF (0.06 at %)	0.46°	0.42°
Ag (0.26 at %)+ Cu (0.02 at %) codoped ZnS:TbOF	0.47°	0.38°
Ce codoped ZnS:TbOF	0.47°	0.42°

(unit : degree, variation for each film : ± 0.01°)

The XRD FWHM values for Ce codoped ZnS:TbOF (0.42°) is same as undoped ZnS:TbOF(0.42°) after annealing at 500°C for 60 minutes (Table 6.1). Therefore the crystallinity of ZnS:TbOF film was not improved by Ce doping.

6.3.3 SEM

Figure 6.3 shows SEM images for as-deposited and annealed (500°C for 60 minutes) samples. The images from uncodoped ZnS:TbOF films are shown in Figure 6.3a

and b, and from as-deposited and annealed (500°C for 60 minutes) Ag codoped

ZnS:TbOF film in Figures 6.3c and d, respectively. The surface particle size of Ag

codoped ZnS:TbOF film was about 0.25 μm as compared to about 0.15 μm for

uncodoped ZnS:TbOF film. Cu codoped ZnS:TbOF film also showed a larger surface

particle size (almost the same as Ag codoped ZnS:TbOF films) as compared to

uncodoped ZnS:TbOF films (see figure 6.3e and f). SEM photomicrographs of

ZnS:TbOF, Ag, Cu films annealed at 500°C for 60 minutes and as-deposited films also

did not show any significant change compared to Ag codoped ZnS:TbOF films, as shown

in Figure6.3g and h. But film annealed at 850°C for 5 minutes showed much smaller

surface particle size than film annealed at 500°C for 60 minutes, as shown at Figure 6.3i.

SEM photomicrographs for as-deposited and annealed (500°C for 60 minutes) Ce

codoped ZnS:TbOF films were shown in Figure 6.3j, k and l, respectively. The surface

particle size of uncodoped and Ce doped ZnS:TbOF film was the same for as-deposited

and annealed (500°C for 60 minutes) films.

6.3.4 TEM

Cross sectional transmission electron microscope (XTEM) photomicrographs of

Cu codoped ZnS:TbOF films show a constant grain size and crystallinity of the as

deposited (Figure 6.4a) versus films annealed at 500°C for 60 minutes (Figure 6.4b). The

Cu codoped ZnS:TbOF film annealed at 850°C for 5 minutes (Figure 6.4c) exhibited 10 ~

20nm precipitates in the lattice. While these precipitates were too small to analyze by

TEM diffraction, they are likely to be a Cu-rich sulfide phase because Cu^{+1} (0.96Å) is

much larger than Zn^{+2} (0.74Å), and the Cu^{+1} ion solubility in the ZnS is lower than the doping level in this study [126].
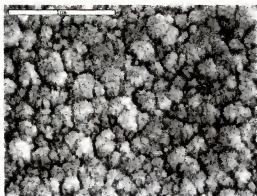
a) Plain ZnS:TbOF (as-dep)
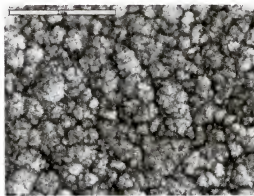
b) Plain ZnS:TbOF (500C/60min annealing)
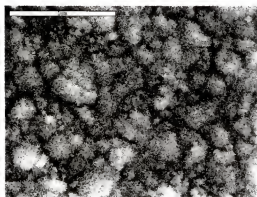
c) ZnS:TbOF, Ag (as-dep)
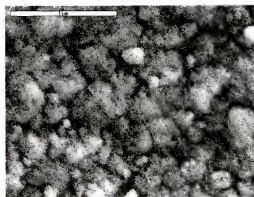
d) ZnS:TbOF, Ag (500C/60min annealing)
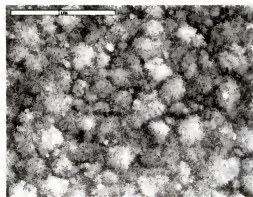
e) ZnS:TbOF, Cu (as-dep)
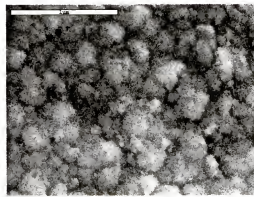
f) ZnS:TbOF, Cu (500C/60min annealing)
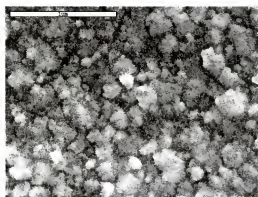
g) ZnS:TbOF, Cu, Ag (as-dep)
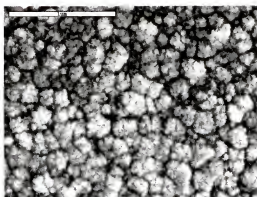
j) ZnS:TbOF, Ce₂O₃ (as-dep)
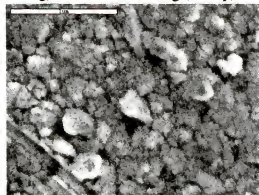
h) ZnS:TbOF, Cu, Ag (500C/60min)
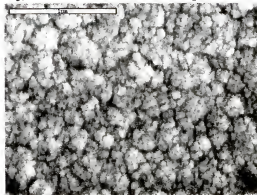
k) ZnS:TbOF, Ce₂O₃ (500C/60min)
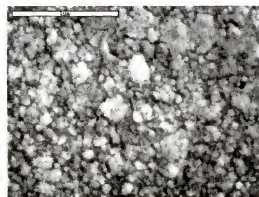
i) ZnS:TbOF, Cu, Ag (850C/5min)
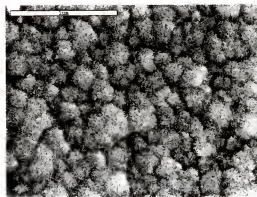
l) ZnS:TbOF, Ce₂O₃ (850C/5min)

Figure 6.3 SEM photographs of a) ~ b) undoped, c) ~ d) Ag doped, e) ~ f) Cu doped, g) ~ i) Ag + Cu codoped, j) ~ l) Ce₂O₃ doped ZnS:TbOF film.

a)   0.1 μm   b)

c)
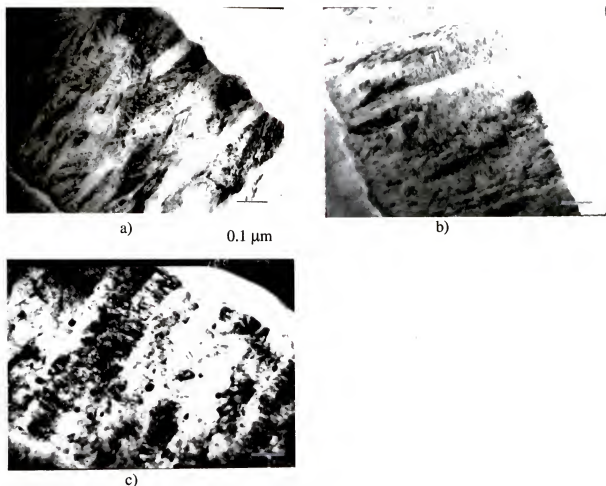
Figure 6.4 Transmission electron microscope (TEM) photographs of Cu codoped ZnS:TbOF films a) as-deposited, b) annealed at 500°C for 60 minutes, and c) annealed at 850°C for 5 minutes.

Even though the surface morphology from SEM micrographs did not show any significant change between the as-deposited and annealed (at 500°C for 60 minutes) Ag + Cu codoped ZnS:TbOF, cross sectional TEM photographs show that the grain size of ZnS:TbOF, Ag, Cu films annealed at 500°C for 60 minutes (Figure 6.5b) was about 100

nm vs. 50 nm for as-deposited films (Figure 6.5a). This suggests that grain growth could lead to improved crystallinity of ZnS:TbOF, Ag, Cu.

a)

0.1 μm

b)
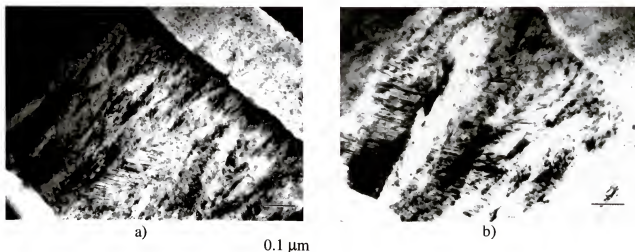
Figure 6.5 Transmission electron microscope (TEM) photographs of Ag + Cu codoped ZnS:TbOF film a) as-deposited, and b) annealed at 500°C for 60 minutes.

6.3.5 AFM

Surface roughness of EL phosphor films can significantly affect the outcoupling efficiency of the device. AFM is used to quantitatively analyze the surface roughness in this study. The RMS surface roughness was 6~ 7 nm versus 6 ~ 9 nm for Ag codoped versus uncodoped ZnS:TbOF films, respectively (Table 6.2). The RMS roughness was 8 ~ 10 nm for Cu codoped films, similar to uncodoped or Ag codoped films. However, the RMS roughness of ZnS:TbOF, Ag, Cu was about 12 nm and 15 nm for as-deposited and films annealed at 500°C for 60 minutes, respectively (Table 6.2). These values were

significantly larger than the roughness value (6 – 10nm) of the uncodoped, Ag or Cu

singly codoped ZnS:TbOF films (Table 6.2). The RMS (root mean square) roughness of

Ce doped ZnS:TbOF films were in the range of 7 – 9 nm.

Table 6.2 Surface roughness measured by AFM for uncodoped, Ag codoped, Cu codoped, Ag + Cu codoped, and Ce_2O_3 codoped ZnS:TbOF films.

	As-dep.	Annealed (500°C, 60 min.)	Annealed (850°C, 5 min.)
Undoped ZnS:TbOF	9	6	-
Ag codoped ZnS:TbOF	6	7	-
Cu codoped ZnS:TbOF	10	8	8
Ag + Cu codoped ZnS:TbOF	12	15	6
Ce codoped ZnS:TbOF	9	7	9

(unit : nm)

Figure 6.6 shows the actual surface morphology from AFM for undoped (a and

b), Ag + Cu codoped (c and d), and Ce_2O_3 codoped (e and f), and ZnS:TbOF films. These

AFM images show significantly larger surface roughness for annealed Ag + Cu codoped

ZnS:TbOF film.
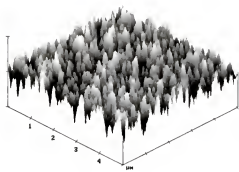
a) Uncodoped ZnS:TbOF (as-dep.)
   RMS = 9nm
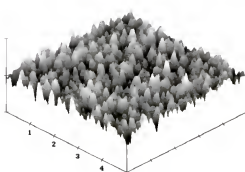
b) Uncodoped ZnS:TbOF (500°C/60min. annealing)
   RMS = 6 nm
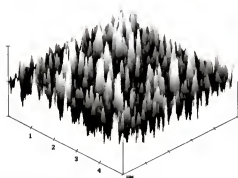
c) ZnS:TbOF, Cu, Ag (as-dep.)
   : 12nm
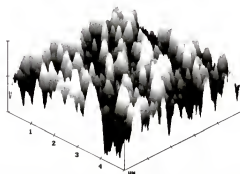
d) ZnS:TbOF, Cu, Ag (500°C/60min. annealing)
   : 15nm
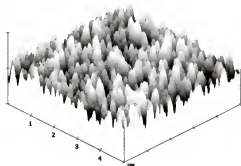
e) ZnS:TbOF, Ce_2O_3 (as-dep.)
   : 9nm
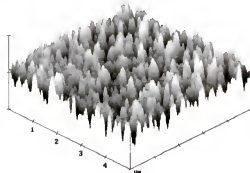
f) ZnS:TbOF, Ce_2O_3 (500°C/60min. annealing)
   : 7nm

Figure 6.6 AFM surface morphologies of a) and b) uncodoped, c) and d) Ag + Cu codoped, and e) and f) Ce_2O_3 codoped ZnS:TbOF film.

6.3.6 SIMS

The SIMS data in Figure 6.7 show that the Ag concentration in the interface region of annealed ZnS:TbOF, Ag films was much higher than in the middle of the film, whereas the concentration was uniform in as-deposited films. This indicates that Ag segregated out of the ZnS:TbOF lattice at 500°C, consistent with relatively low solubility of Ag in ZnS. This is not surprising since the Ag^{+1} ionic size of 1.26Å is much larger than Zn^{+2}(0.74Å). Based upon this large size difference, segregation of Ag to the grain boundaries would also be expected. Leaky "turn-on" behavior and low threshold voltages of annealed Ag codoped ZnS:TbOF films can be attributed to Ag segregation and precipitation in the grain boundary after annealing.
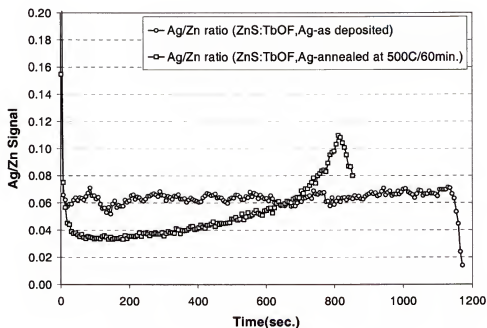
Figure 6.7 Ag^+/Zn^+ secondary ion intensity versus sputter time for Ag codoped ZnS:TbOF film.
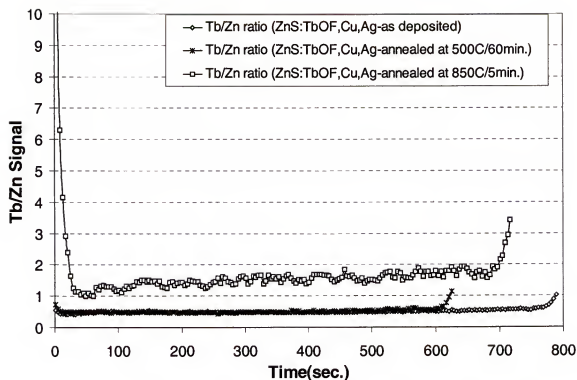
Figure 6.8 Tb$^+$/Zn$^+$ secondary ion intensity versus sputter time for Ag + Cu codoped ZnS:TbOF film.

Ag + Cu codoped ZnS:TbOF films annealed at 850°C for 5 minutes showed much smaller surface particle size than for films annealed at 500°C for 60 minutes, as shown in figure 6.3. These small grains in the surface region seemed to be Tb rich secondary phases. This conclusion is based on the fact that films annealed at 850°C for 5 minutes showed over 20 times higher Tb concentration in the surface region from secondary ion mass spectroscopy (SIMS) depth analysis (Figure 6.8), while Tb concentrations for as-deposited films and films annealed at 500°C for 60 minutes were quite constant throughout the films.
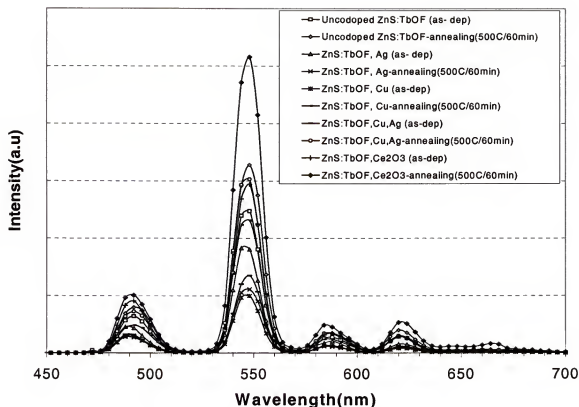
Figure 6.9 Electroluminescent (EL) spectra of uncodoped, Ag, Cu, Ag + Cu and Ce_2O_3 codoped ZnS:TbOF films as-deposited and after annealing at 500°C for 60 minutes.

The electroluminescent (EL) emission spectrum was unchanged by codoping and/or annealing, as shown in Figure 6.9. As shown, emission from terbium in the ZnS host had the typical four main emission peaks at 492nm ($^5D_4 \rightarrow {}^7F_6$), 548nm ($^5D_4 \rightarrow {}^7F_5$), 588nm ($^5D_4 \rightarrow {}^7F_4$) and 620nm ($^5D_4 \rightarrow {}^7F_5$) [4,8].

6.3.8 PL Emission

6.3.8.1 PL emission of target

PL of the targets (ZnS:TbF$_3$ and ZnS:TbOF) show no emission peak from the Tb center. They just show the broad emission band around 470 nm (Figure 6.10). The lack of Tb emission peaks can be understood by the target preparation conditions. In this study, ZnS:TbF$_3$ and ZnS:TbOF targets are made by hot pressing of mixed ZnS and TbOF or TbF$_3$ powder. Therefore, the Tb^{+3} ions may not dissolve into the ZnS matrix and may not be substituted on the Zn^{+2} ion sites. This speculation is based on the fact that the Tb^{+3} ionic size (0.92Å) is much larger than the Zn^{+2} ionic size (0.74Å) and the equilibrium solubility of Tb in ZnS is very low. However, O^{-2} and F^{-1} ions will be more mobile than Tb^{+3} ion because the O^{-2} and F^{-1} ionic sizes are 1.32Å and 1.33Å, both much smaller than the S^{-2} ionic size (1.84Å). The PL peak around 470 nm (Figure 6.10) is assigned to a Zn vacancy – F recombination. It is reported that ZnS phosphor has a self-activated luminescence peak around 470 nm due to Zn^{+2} vacancy acceptor and a Cl^{-1} donor recombination [41]. It is assumed that the F^{-1} ion will also act as a donor, similar to the Cl^{-1} ion. The intensity change between the ZnS:TbF$_3$ and ZnS:TbOF targets may be due to the number of Zn vacancy – F recombination centers because the ZnS:TbF$_3$ target has a higher F^{-1} ion concentration and therefore a larger chance to recombine with a Zn vacancy.

6.3.8.2 PL emission of codoped films

Figure 6.11 shows a comparison of PL and EL emission spectra from ZnS:TbOF films. The photoluminescence emission peaks are in exactly the same position as the electroluminescence peaks and the four main emission peaks can be assigned to the same

Tb transitions. The EL spectrum was measured every 4nm step, while the PL spectrum was measured with 1nm step. The peak doublet structure near 550 nm is only seen in PL due to the step size and energy resolution of the spectrometer.
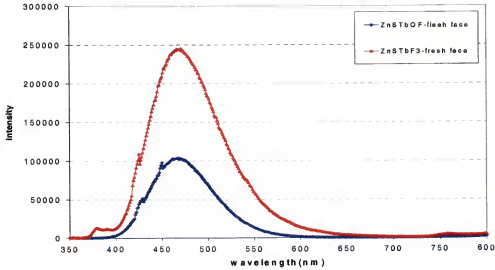
Figure 6.10 The PL emission spectra from ZnS:TbOF or ZnS:TbF$_3$ targets.
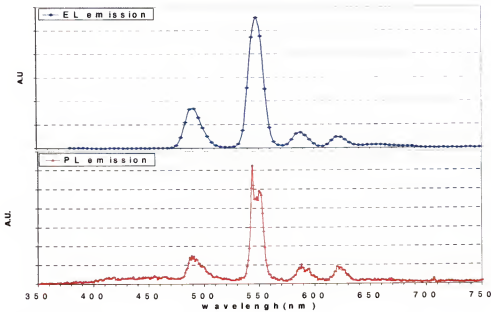
Figure 6.11 a) EL and b) PL emission spectrum of ZnS:TbOF films.
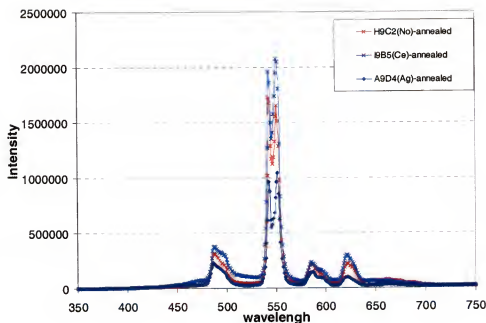
Figure 6.12 PL emission spectrum of Ce and Ag doped ZnS:TbOF compared to undoped ZnS:TbOF films.

The Ce and Ag codoped ZnS:TbOF films do not show any significant differences in the PL emission sprctrum as shown in Figure 6.12. However, Cu doped ZnS:TbOF shows a broad emission peak in the 650 – 670nm ranges corresponding, to the Cu contents. As shown in Figure 6.13, the intensity of the broad peak around 650 – 670nm range depends on the concentration of Cu, and it is known that the Cu forms an acceptor level at 1.25eV above the valence band in the ZnS [41]. Halogen element such as F, Cl, Br, I and elements that have +3 charge, such as Al, Ga, or In, form a donor level in the ZnS. Even though the F acceptor energy level in ZnS have not been reported, it is reasonable to assume that the F acceptor level is similar to the other acceptor levels such as In or Cl, because the F acceptor level in ZnSe is quite comparable to those from In or

Cl [41]. In addition, the Cu to In recombination peak in ZnS was reported around 650nm. Therefore, it is possible to assign this peak to a Cu-F recombination. When 0.033 at % of Cu is added to the ZnS:TbOF film, the intensity of the Cu-F recombination peak (about 650nm) is just one third of the Tb $^5D_4 \rightarrow {}^7F_5$ transition peak. However, as the Cu concentration increases to 0.14 at.%, the intensity of the Cu-F recombination peak (about 650nm) increases by almost same amount as the Tb $^5D_4 \rightarrow {}^7F_5$ transition peak. The PL spectrum of the Cu doped ZnS:TbOF films are significantly different from the EL spectrum of Cu doped ZnS:TbOF films since the latter do not show the emission peak from the Cu to F recombination. This different emission behavior between EL and PL can be explained by the strong electric field applied on the phosphor layer for EL. Under a strong electric field, the electron and hole will quickly be swept to the opposite electrodes, reducing the rate of electron-hole recombination in the phosphor layer. Therefore, donor-acceptor recombination process may not be effective as a direct excitation process in electroluminescence.
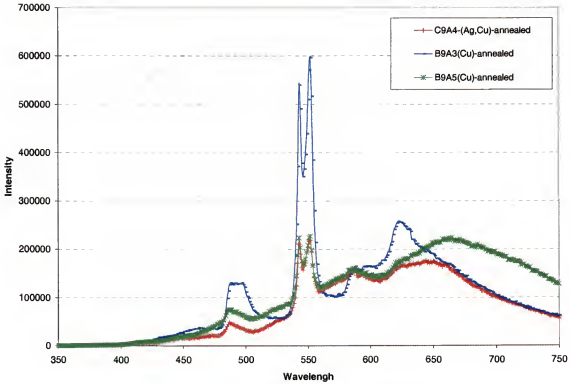
Figure 6.13 The PL emission spectrum of Cu doped ZnS:TbOF films.

6.3.9 Electrical Properties of Ce Codoped ZnS:TbOF

6.3.9.1 Efficiency

The luminous efficiency, η (*lm*/W), of EL devices can be calculated by dividing the luminance of the device, L (cd/m²), by input power density, P_{in} (W/m²), as

$$\eta[lm / W] = \pi \times \frac{L[cd / m^2]}{P_{in}[W / m^2]} .$$

The luminance of the device is directly measured and the input power density can be calculated from the voltage drop across the device, E_{in} and current passing through the device such that

$$P_{in}[W / m^2] = \frac{f[1/ s] \times E_{in}[W \cdot s]}{area[m^2]}$$

where f (Hz) is the alternating current frequency. In this study, all drive frequency is 60 Hz and half cell devices are tested. E_{in} (W·s) is total energy delivered to the pixel per cycle and can be calculated by integrating over time the current multiplied by voltage across the EL devices. Area (m^2) is the pixel area, which is 7.9×10^{-6} m^2. The efficiency of the devices is summarized in table 6.3 for 20V, 40V and 60V above the threshold voltage of both uncodoped and Ce codoped ZnS:TbOF films, which were annealed at 500°C for 60 minutes.

The efficiency of the Ce doped ZnS:TbOF film at 40V above threshold voltage is 0.24 *lm*/W after annealing at 500°C for 60minutes. This value is about 63% higher than the 0.15 *lm*/W of the uncodoped, annealed ZnS:TbOF film.

Table 6.3 The efficiency of uncodoped ZnS:TbOF and Ce doped ZnS:TbOF films after annealing at 500°C for 60 minutes.

	Uncodoped ZnS:TbOF			Ce doped ZnS:TbOF		
Voltage (V) above threshold voltage	20V	40V	60V	20V	40V	60V
Efficiency (lm/W)	0.17	0.15	0.15	0.32	0.24	0.22

<u>6.3.9.2 Excitation efficiency</u>

Excitation efficiency is estimated from the maximum brightness of the time-dependent EL emission (B_{max}) divided by internal charge (Q_{int}) as discussed in section 5.2.3.5.
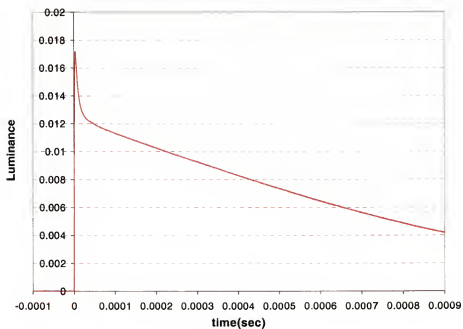
Figure 6.14 Typical EL luminance versus time, L(t), where the front edge of the pulse exciting EL occurred at a time of zero.

a)

b)
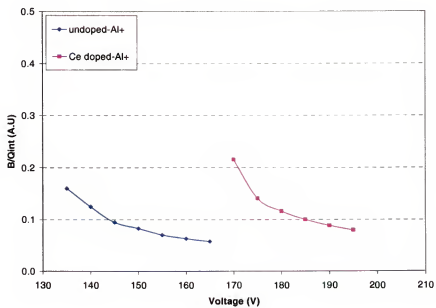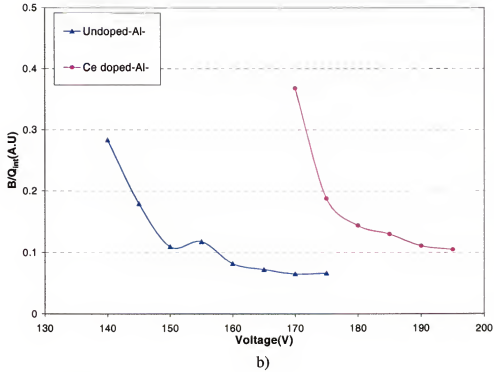
Figure 6.15 Excitation efficiency, (B_{max}/Q_{int}) versus voltage for a) Al+ polarity and b) Al- polarity.

The brightness of the device is measured and displayed on an oscilloscope. Figure 6.14 shows typical EL luminance versus time, L(t). The maximum current value in Figure 6.14 is B_{max}. Internal charge (Q_{int}) was equated to the stored charge when the applied voltage reaches a value of 0V at the end of the pulse, which assumes that the rapid charge relaxation at the end of voltage pulse is simply discharging the device capacitance [40]. For Al- polarity, the excitation efficiencies of uncoded and Ce codoped films are stabilized at 0.07 and 0.11(a.u), respectively, as shown in Figure 6.15a. For the Al+ polarity, the excitation efficiencies of uncoded film and Ce codoped film are 0.06 and 0.08, respectively, as shown in figure 6.15b.

6.3.9.3 Q–V, C-V and Q$_{int}$ - F$_b$ analysis

The significance of and procedure for measuring electrical properties were already discussed in chapter 2 and chapter 3, respectively. The Q-V plots in figure 6.16 show the external charge (Q$_{ext}$) versus applied voltage on the EL device (V$_{EL}$) at 60V above threshold voltage for uncodoped and Ce codoped ZnS:TbOF films after annealing at 500°C for 60 minutes. These Q-V data are for Al + polarity. All measurements were done using 100Ω resistor as the sense element. Corresponding C-V plots for uncodoped film and Ce doped film are given in figure 6.17.
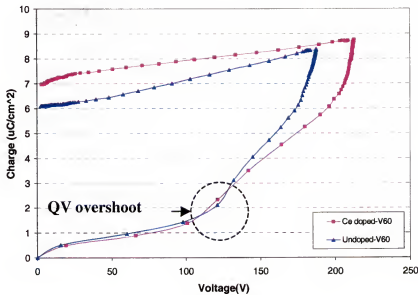
Figure 6.16 External charge (Q) versus applied voltage (V$_{EL}$) up to 60V above threshold voltage for uncodoped and Ce codoped annealed ZnS:TbOF films.
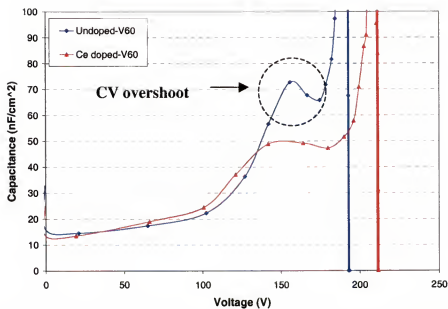
Figure 6.17 Capacitance (C) versus applied voltage (V_{EL}) up to 60V above the threshold voltage for uncodoped and Ce codoped, annealed ZnS:TbOF films.
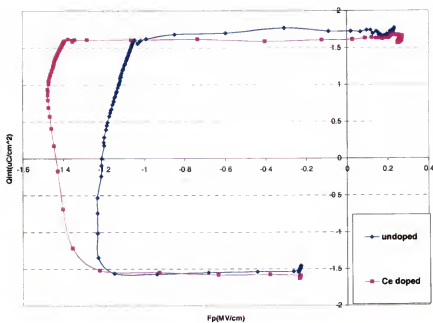
Figure 6.18 Internal charge (Q_{int}) versus phosphor field (F_p) up to 30V above threshold voltage for uncodoped and Ce codoped annealed ZnS:TbOF films.

In the Q-V plot of figure 6.16, both uncodoped and Ce codoped film show the Q-V overshoot (Q-V overshoot means non-linear electrical turn-on behavior as indicated in figure 6.16). This type of Q-V overshoot is known to indicate the existence of dynamic space charge. However, the uncodoped film shows larger overshoot than does the Ce codoped film. This difference is clearer in the C-V plot of figure 6.17. The actual capacitance of the dielectric layers of the device is about 45 nF/cm^2. Figure 6.17 shows that overshoot in the C-V plot of uncodoped film reaches 75 nF/cm^2. This value is much larger than the case of Ce codoped films, which reach only to 50 nF/cm^2. That means that the amount of space charge is reduced by Ce codoping.

As already mentioned in chapter 2, internal and external charge is not separable in the Q-V curve and the voltage is equal to the total voltage across the ACTFEL device. Therefore, internal charge (Q_{int}) versus phosphor field (F_p) data give more direct information about the device physics. Figure 6.18 shows internal charge (Q_{int}) versus phosphor field (F_p) data for uncodoped film and Ce codoped film up to 30V above threshold voltage. To obtain an ideal shape for $Q_{int} - F_P$ data, i.e. horizontal lines between A-B and D-E and vertical lines between B-C of figure 2.19, the phosphor capacitance value was chosen to be 1.2nF for uncodoped film and 0.9nF for Ce codoped film. These values correspond to 15.2nF/cm^2 and 11.4nF/cm^2, respectively. The measured capacitance values were about 12 – 13nF/cm^2. The $Q_{int} - F_p$ data from uncodoped and Ce codoped films show significant differences in their steady state field (F_{SS}) which is much larger in a Ce codoped film (1.45MV/cm) versus an uncodoped film (1.2MV/cm). However, the internal conduction charges (Q_{cond}) are similar in uncodoped (3.2µC/cm^2) and Ce codoped films (3.1µC/cm^2).

For Al- polarity, uncodoped films show early electrical turn-on compared to the Ce codoped film. The electrical turn-on of uncodoped film is 60V in Al- polarity. This is significantly lower than the 120V in Al + polarity (Figure 6.16). For Ce codoped film, the electrical turn-on voltage for the Al- polarity is about 110V, which is almost the same value as for the Al+ polarity. Figure 6.20 shows the internal charge (Q_{int}) versus phosphor field (F_p) data for uncodoped film and Ce codoped film up to 30V above threshold voltage for the Al- polarity. Uncodoped films show onset of internal charge flow at fields of 0.9MV/cm, and the phosphor field increases up to 1.15MV/cm. In contrast to uncodoped films, Ce codoped films show a nearly constant phosphor field of 1.48 MV/cm. In summary, Ce codoping results in several significant changes in the electrical properties as compared to the uncodoped films. Codoping increases the power and the excitation efficiencies of ZnS:TbOF films. Codoping also reduces the static space charge and increases the steady state phosphor field. Finally, codoping increases the threshold voltage, especially for the Al- polarity in the half cell devices.
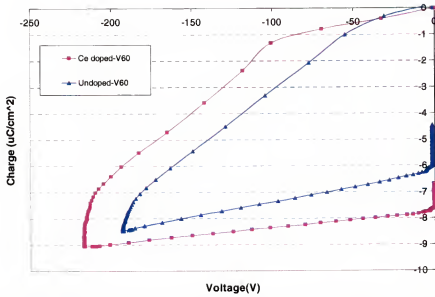
Figure 6.19 Q-V up to 60V above threshold voltage for Al- polarity on annealed, uncodoped and Ce codoped ZnS:TbOF films.
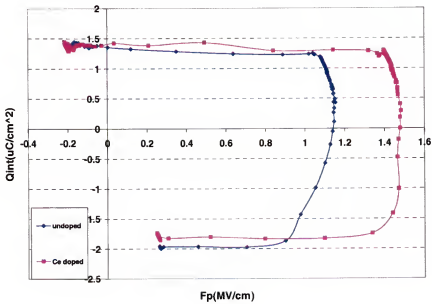
Figure 6-20 The internal charge (Q_{int}) – phosphor field (F_p) plots for uncodoped film and Ce doped film up to 30V above threshold voltage on Al- polarity.

6.3.10 Electrical Properties of Ag, Cu and Ag + Cu Codoped ZnS:TbOF

6.3.10.1 Efficiency

The luminous efficiency, η (lm/W), of the Ag, Cu and Ag + Cu codoped film was measured by the same method described in section 6.3.9.1 and the results are summarized in Table 6.4.

Table 6.4 The power efficiency of uncodoped ZnS:TbOF and Ag, Cu and Ag + Cu codoped ZnS:TbOF films after annealing at 500°C for 60 minutes.

	Efficiency (lm/W)		
Voltage above V_{th}	20V	40V	60V
Uncodoped	0.17	0.15	0.15
Ag doped	0.17	0.17	-
Cu doped	0.15	0.15	-
Ag + Cu doped	0.20 (15V)	-	-

As shown in the table 6.4, the power efficiency was not improved by Ag, Cu and Ag + Cu codoping in ZnS:TbOF film. In the case of Ag + Cu codoped film, the efficiency was measured at 15V above threshold voltage (V_{15}) because the devices burned out at V_{20}. Since the efficiency generally decreases from a maximum at the threshold voltage to lower efficiencies at higher voltages (e.g. V_{20}), it is probable that the efficiency at V_{20} of Ag + Cu codoped film would have been the same as Ag or Cu single codoped films. This decrease in efficiency with increasing voltage explains why the value

for Ag + Cu codoped film at V_{15} is slightly higher than the uncodoped, Cu codoped or Ag codoped films at V_{20}.

6.3.10.2 Excitation efficiency

For Al+ polarity, the excitation efficiencies of the Ag codoped, Cu codoped or uncodoped film are in the range of $0.13 - 0.19$ (a.u.) compared to 0.25(a.u.) for the Ag + Cu codoped film at V_{10}, as shown in figure 6.21a. For the Al- polarity, the Ag codoped, Cu codoped and Ag + Cu codoped films have excitation efficiencies in the range of $0.11 - 0.12$ (a.u.) compared to 0.25 (a.u.) of Ag + Cu codoped films at V_{15}, as shown at figure 6.21b. Therefore, it can be concluded that Ag + Cu codoping significantly improves the excitation efficiencies.
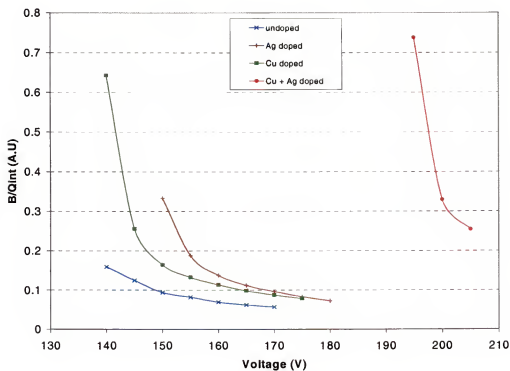
a)
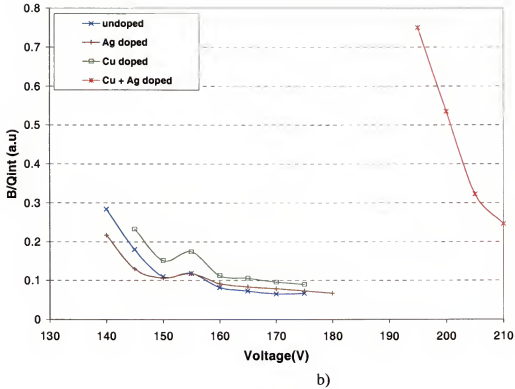
Figure 6.21 Excitation efficiency by B_{max}/Q_{int} versus voltage plot a) Al + polarity and b) Al- polarity.

6.3.10.3 Q–V, C-V and Q_{int} - F_p analysis of Ag codoped film

Electrical properties such as Q-V, C-V and Q_{int} - F_p for uncodoped and Ag codoped ZnS:TbOF films for Al + polarity are given in figure 6.22a, b and c up to 40 volt above threshold. Ag codoped films show significantly decreased overshoot in the Q-V plot and C-V plot versus uncodoped ZnS:TbOF films. In the C-V plot shown in figure 6.22c, uncodoped films show overshoot up to 73 nF/cm^2 compared to 57 nF/cm^2 of Ag codoped film. However, steady state field (F_{ss}) from Q_{int} - F_p data are quite comparable for uncodoped and Ag codoped films. The steady state field (F_{ss}) of the uncodoped films and the Ag codoped film are ≈1.2 MV/cm and ≈1.3 MV/cm, respectively. The

conduction charge (Q_{cond}) of uncodoped films and Ag codoped films up to 40V above

threshold are $\approx 3.8 \ \mu C/cm^2$ and $\approx 3.6 \ \mu C/cm^2$, respectively. And, Ag codoping shows a

decrease in the internal charge (Q_{int}) compared to the uncodoped film from $\approx 4.3 \ \mu C/cm^2$

to $\approx 3.7 \ \mu C/cm^2$. In summary, Ag codoping reduces both space charge and conduction

charges.

a)

b)

c)
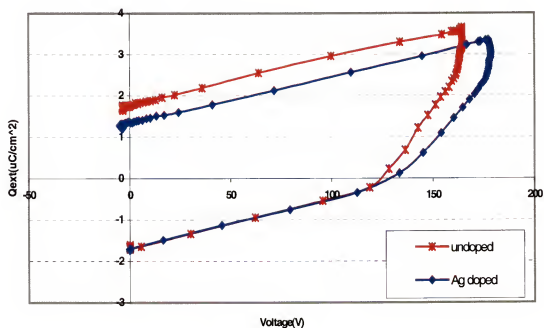
Figure 6.22 a) External charge (Q) versus applied voltage (V_{EL}), b) capacitance (C) versus applied voltage (V_{EL}), c) internal charge (Q_{int}) versus phosphor field (F_p) data up to 40V above threshold for uncodoped and Ag codoped ZnS:TbOF films.

6.3.10.4 Q-V, C-V and Q_{int} - F_p analysis of Cu codoped film

Figure 6.23 shows Q-V, C-V and Q_{int} - F_p data for Cu codoped films. From the Q-V data (Figure 6.23a), the conduction charges for uncodoped films and Cu codoped films are ≈ 3.8 $\mu C/cm^2$ and ≈ 3.5 $\mu C/cm^2$, respectively. Cu codoped films show the Q-V overshoot similar to uncodoped films. However, the amount of the overshoot for Q-V data of Cu codoped films is smaller than for uncodoped films. This difference is clearer in the C-V data shown at Figure 6.23b. The overshoot of uncodoped film (73 nF/cm^2) is larger than that of the Cu codoped films (61 nF/cm^2). This implies that Cu codoping decreases the space charge. Figure 6.23c shows internal charge (Q_{int}) versus phosphor field (F_p) for uncodoped and Cu codoped films. The steady state phosphor fields for uncodoped and Cu co-doped films are both in the range $1.2 - 1.3$ MV/cm. The internal charge for a Cu codoped film is ≈ 3.7 $\mu C/cm^2$, which is slightly lower than the ≈ 4.3 $\mu C/cm^2$ of a uncodoped film. In summary, Cu codoping gives similar effects as Ag codoping, i.e. reduction in space charge and a decrease in the conduction charges (Q_{int}).

a)

b)

c)
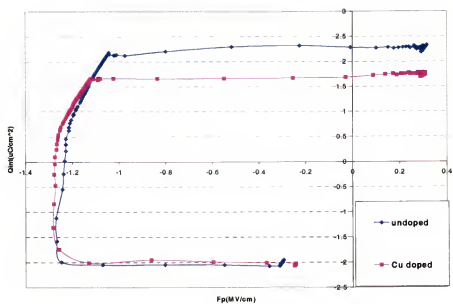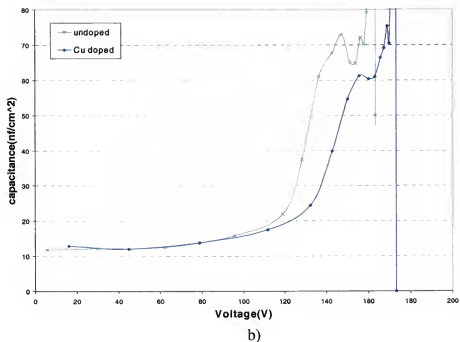
Figure 6.23 a) External charge (Q) versus applied voltage (V_{EL}) data, b) capacitance (C) versus applied voltage (V_{EL}) data, c) internal charge (Q_{int}) versus phosphor field (F_p) data up to 40V above threshold for uncodoped and Cu codoped ZnS:TbOF films.

6.3.10.5 Q-V, C-V and Q_{int} - F_p analysis of Ag + Cu codoped film

Ag + Cu codoped films have significantly higher threshold voltages compared to uncodoped, Ag codoped and Cu codoped films. Half cell Ag + Cu codoped films survived up to 20V above threshold voltage without burnout. Figure 6.24 shows Q-V, C-V and Q_{int} - F_p data for Ag + Cu codoped films up to 10V above threshold. Q-V data of the Ag + Cu codoped films shows two significant changes compared to uncodoped films. First, Ag + Cu codoping results in a big increase in the electrical turn-on voltage. The electrical turn-on voltage of the Ag + Cu codoped film is ≈ 195V, compared to ≈ 130V for the uncodoped film. Second, Ag + Cu codoping results in ≈ 10% decrease in conduction charge. The conduction charge of Ag + Cu codoped films is ≈ 1.0 μC/cm^2 and that of uncodoped film is ≈ 1.1 μC/cm^2. This trend of the conduction charge decrease is consistent with Ag or Cu singly codoped films. Figure 6.24c shows the Q_{int} - F_p data of Ag + Cu codoped and uncodoped films. This Q_{int} - F_p plot shows a big increase in the steady state field (F_{ss}) for Ag + Cu codoping. The F_{ss} of Ag + Cu codoped films is ≈ 1.7 MV/cm, which is significantly higher than is ≈ 1.1 MV/cm of uncodoped films. A second difference is a decrease of internal charge from ≈ 1.1 μC/cm^2 for Ag + Cu codoped films versus ≈ 1.5 μC/cm^2 for uncodoped films. Reduction of space charge can be detected by the reduction of capacitance overshoot evident in C-V plots for Ag + Cu codoped films versus uncodoped films, however this difference is near the noise level for data taken at 10V above threshold. To more clearly demonstrate the reduction of space charge in Ag + Cu codoped films, C-V plot under higher applied field were collected from full stack devices. The data from Ag + Cu codoped and uncodoped films are shown in figure 6.25 up to 60V above threshold voltage. Because of different thickness of the top dielectric

layer, the physical capacitance (C_i^{phys}) of the each plot is different. The thickness of the top dielectric layer for undoped film is $\approx 1400\text{\AA}$ and that of Ag + Cu codoped film is $\approx$ 4300Å. For the uncodoped film, C_i^{phys} is $\approx$ 35 nF/cm^2 and for Ag + Cu codoped film, $\approx$ 19 nF/cm^2. In figure 6.25, uncodoped film shows significant overshoot in C-V plot and a decrease in the physical capacitance value. However, Ag + Cu codoped films do not show any capacitance overshoot and they saturate at $\approx$ 19 nF/cm^2, equal to C_i^{phys}. This indicates that the Ag and Cu codoping suppress the space charge more efficiently than does Ag or Cu alone.
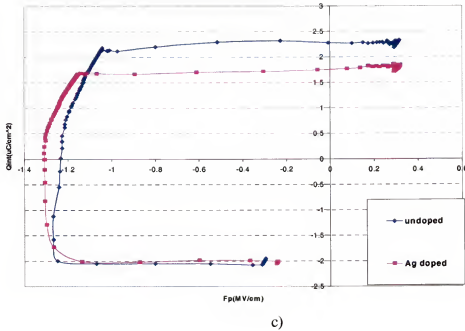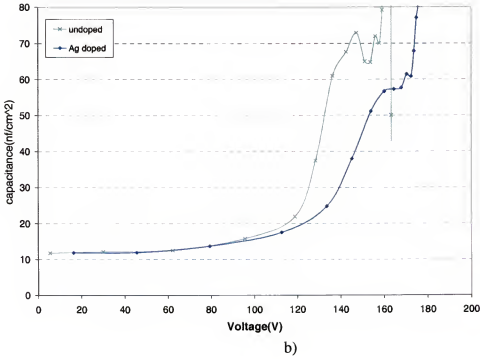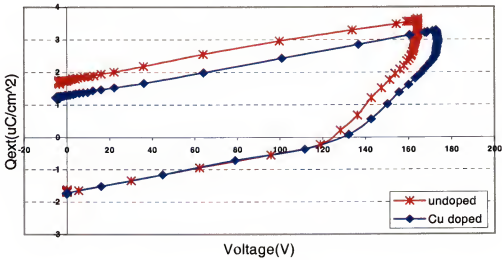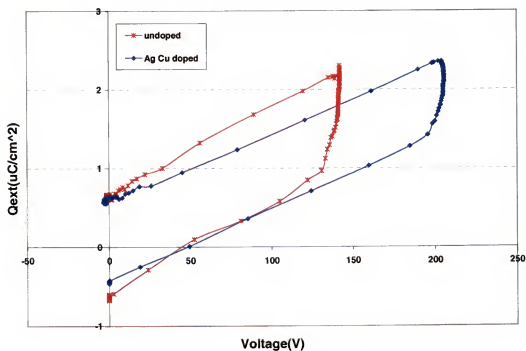

a)
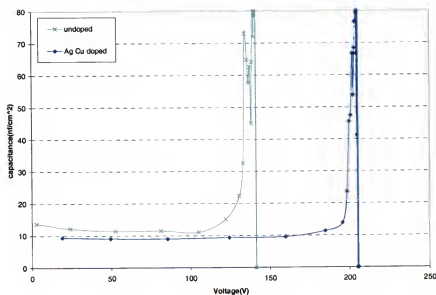
b)
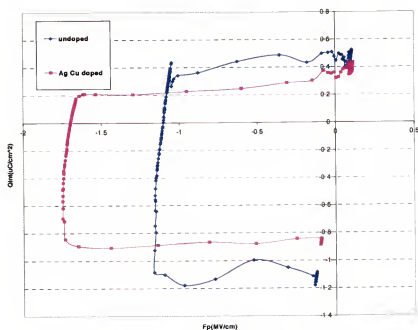
c)

Figure 6.24 a) External charge (Q) versus applied voltage (V_{EL}), b) capacitance (C) versus applied voltage (V_{EL}), c) internal charge (Q_{int}) versus phosphor field (F_p) data up to 10V above threshold for annealed, uncodoped and Ag + Cu codoped ZnS:TbOF films.
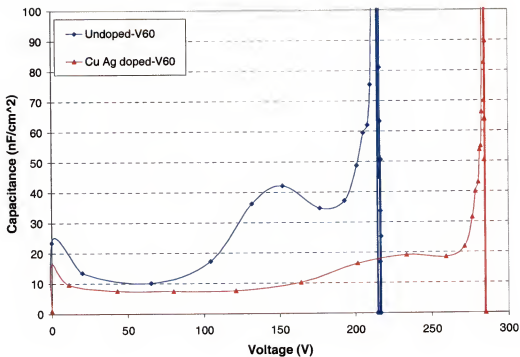
Figure 6.25 Capacitance (C) versus applied voltage (V$_{EL}$) data up to 60V above threshold for annealed, full cell uncodoped and Ag + Cu codoped ZnS:TbOF films.

6.3.11 EL Emission Decay Curve

6.3.11.1 EL emission decay of Ce codoped film

The EL decay curve can be used to compare the radiative efficiency of electroluminescent films when excited by voltage pulses much shorter than the decay time [126]. Figure 6.26 shows the EL decay curves of uncodoped films and Ce codoped films at 20V above threshold voltage, for both positive and negative polarity for the Al electrode. The first curve is for a positive pulse on the Al electrode side (Al+), and the second curve is for negative pulse on the Al electrode side (Al-). These curves were normalized for the Al+ side. As shown in Figure 6.26, there are two significant differences between the uncodoped film and Ce codoped films. First, the relative peak

intensity for the Al- side is ≈ 70% of the Al+. However, for Ce codoped films, the relative peak intensities for Al+ and Al- are almost same. The relative peak intensity for Al- side is ≈ 97% of Al+. Another difference is the decay constant of the EL emission. Figure 6.27 shows the emission decay curve up to 900μs after the electric pulse. This shows a typical emission decay curve, with a sharp decay followed by slower decay region. However, the decay is not characterized by a constant at longer times as shown in figure 6.28. The electroluminescent emission decay curves are plotted in natural log scale for both Al+ and Al- in figure 6.28a and b. For both polarities, the emission decay is much faster in uncoded films than Ce codoped films. The Al- polarity for uncoded films exhibits a first order exponential decay. The Al+ polarity for uncoded films shows first order decay after 1ms. Up to 1ms, the intensity decays a variable rate, changing from a slow to a fast decay. However, for both polarities, the Ce codoped film shows slow decay rates at short times followed by a faster rate at longer times. In general, the decay constant is inversely proportional to the radiative emission efficiency. Therefore, the slow decay rate for Ce codoped films means improved radiative efficiency.
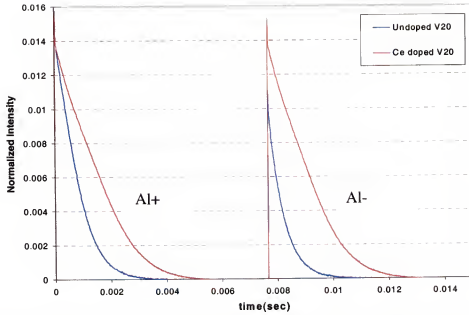
Figure 6.26 EL decay curves of uncodoped film and Ce codoped film at 20V above threshold voltage.
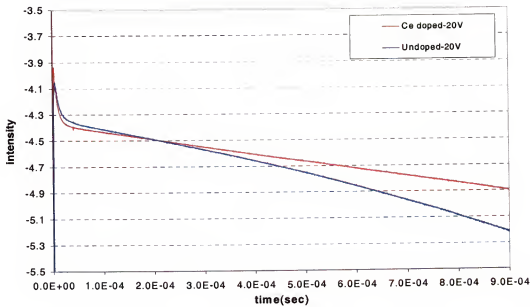
Figure 6.27 The emission decay curve up to 900µs after start of the voltage pulse for Ce codoped ZnS:TbOF film.
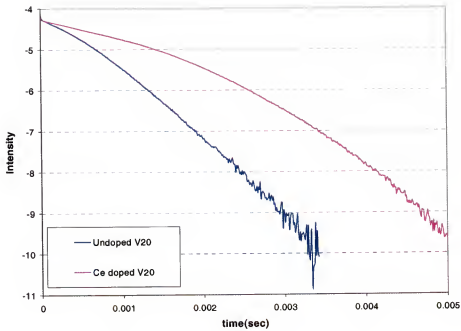
a)
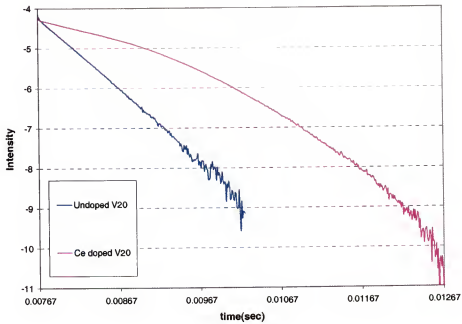
b)

Figure 6.28 The logarithm of electroluminescent intensity versus time for both a) Al+ polarity and b) Al- polarity for uncodoped and Ce codoped ZnS:TbOF.

6.3.11.2 EL emission decay of Ag, Cu and Ag + Cu codoped film

The EL emission decay curve at 10V above threshold voltage for Ag codoped, Cu codoped and Ag + Cu codoped films compared to uncodoped films are shown in figure 6.29. These curves are normalized for the Al+ polarity. The relative intensities of the Al+ and Al- polarities are summarized at table 6.5.
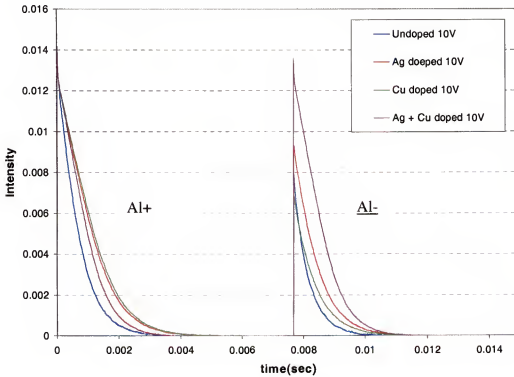
Figure 6.29 EL emission decay curve at 10V above threshold voltage for Ag codoped, Cu codoped and Ag + Cu codoped films compared to uncodoped films.

Table 6.5 Relative peak intensity of Al- polarity over Al+ polarity for Ag, Cu or Ag+Cu codoping.

Codopant	Relative peak intensity of Al- polarity over Al+ polarity (%)
Ag + Cu codoped	97
Ag codoped	66
Cu codoped	49
Uncodoped	56

As shown Table 6.5, the Ag + Cu codoped film does not show big changes in the EL emission intensity between the Al+ and Al- polarity. However, uncodoped, Cu codoped and Ag codoped films show much lower intensity for Al- versus Al+ polarity. The emission decay curves on a natural logarithm scale are shown in figure 6.30. In both polarity, Ag, Cu and Ag + Cu codoped films show slower emission decay behavior than the uncodoped film, but the decay rate of all of these films are faster than the Ce codoped films shown in figure 6.28.
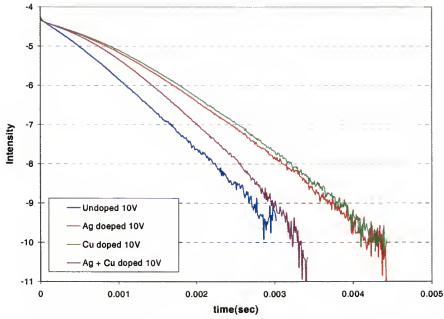
a)
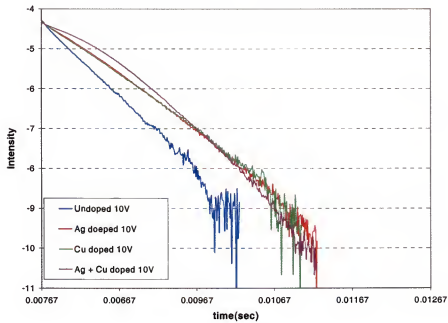
b)

Figure 6.30 The natural logarithm of the electroluminescent emission intensity versus time for both a) Al+ and b) Al- polarity for Ag codoped, Cu codoped, Ag + Cu codoped and uncodoped films.

<div align="center">6.4 Discussions</div>

6.4.1 Ce Codoped ZnS:TbOF Film

As mentioned previously, the Ce codoping in the ZnS:TbOF film improves the EL brightness and efficiency of films after annealing at 500°C for 60 minutes. In the best case, the brightness and the efficiency of the Ce codoped film increased 63% as shown in figure 6.1d and 60% at V_{40} as shown in table 6.3, respectively, as compared to uncodoped film. In this section, the mechanism of the brightness improvement by Ce codoping will be discussed.

From the EL emission process discussed in the section 2.3, the important factors that affect on the device performance are:

- The amount of conduction charge
- Excitation efficiency
- Radiative relaxation efficiency
- Optical outcoupling efficiency

Each of them will be separately discussed in detail.

6.4.1.1 The amount of conduction charge

The amount of the conduction charge is one of the important factors that affect the EL device performance, especially the brightness. As discussed in section 2.3.1, the electrons that impact-excite the luminescent centers are injected from the phosphor/insulator or phosphor/aluminum interfaces and possibly from donor levels in the phosphor layer. The injected electrons can be multiplied by bulk phosphor trap ionization or band to band impact ionization, as discussed in section 2.5.2.2, leading to

larger conduction charge. Increased conduction charge results in an increase in the brightness of the device but requires increased power to do so. Therefore, if the increased brightness results only from the increased conduction charge, the power efficiency of the device will not change.

Table 6.6 The external and internal charge for uncodoped and Ce codoped films (External charge is evaluated at V_{60} (60V above threshold) and internal charge is evaluated at V_{30}, respectively).

		Uncodoped	Ce codoped
External Charge ($\mu C/cm^2$)	Al +	6.3	7.0
	Al -	7.7	7.7
	Average	7.0	7.4
Internal charge ($\mu C/cm^2$)	Al +	3.2	3.3
	Al -	3.2	3.1
	Average	3.2	3.2

The amounts of external and the internal charge were determined from the Q-V and Q_{int}-F_p data for both polarities (Figure 6.16 and figure 6.19). From figure 6.18 and figure 6.20, the internal charge of uncodoped film and Ce codoped film for both polarities can be also obtained. These results, summarized in table 6.6, show that the internal charges of uncodoped and Ce codoped films for both polarities, and the external charge

with Al negative polarity are almost same (3.2 $\mu C/cm^2$ at 30V above threshold). The external charge of Ce codoped film with Al positive polarity is about 10% larger than that of the uncodoped film. However the 10% change in the external conduction is of questionable significance because the improvement in the brightness from Ce codoping is 63% and the efficiency improvement is 60%. Improvement in both parameters shows that the increased conduction charge is not responsible for the brightness improvement since it would not result in improved efficiency.

6.4.1.2 Device efficiency

As reported above and in table 6.3, both device efficiency and brightness improve $\approx 60\%$ for Ce codoped films. As given in section 2.5.1.4, the efficiency of each physical step can be evaluated to develop an understanding of the mechanism responsible for the improvement of the EL device performance.

6.4.1.2.1 Excitation efficiency

The B_{max}/Q_{int} plot for Al – and Al + polarities of uncodoped and Ce codoped film are shown in figure 6.15a and b. The relative excitation efficiency (Figure 6.15a) is equal to B_{max}/Q_{int}, which is 0.06 (a.u) and 0.08 (a.u) for the Al + polarity at 30V above threshold voltage for uncodoped and Ce codoped films. For Al+, the ATO/phosphor interface acts as a cathode, from which electrons are emitted. For the Al – polarity, the B_{max}/Q_{int} value was significantly increased at V_{30} from 0.07 for uncodoped to 0.11 for Ce codoped films, where the phosphor/Al interface acts as a cathode. Therefore, the larger

excitation efficiency by Ce codoping is partially responsible for the improvement in total efficiency.

The excitation efficiency is determined by two important parameters: energy distribution of the injected electrons and excitation cross section. For ZnS:Mn ACTFEL device, several models to predict energy distribution have been developed using Monte Carlo or lucky-drift methods [25], as discussed in section 2.3.2. According to these simulations, the fraction of electrons which acquire sufficient energy to impact excite the Mn^{+2} center is only a few percent. These models have not been applied to ZnS:Tb. However the energy required to excite the Tb^{+3} luminescent center is larger than that to excite the Mn^{+2} center. Assuming the same inelastic scattering rate for Tb as Mn, the fraction of electrons hot enough to excite the Tb^{+3} luminescent center will be lower than that for Mn^{+2} centers. The second important factor for excitation efficiency is the excitation cross section for the luminescent center. The impact cross section of Mn^{+2} ion was estimated to be $1-4 \times 10^{-16}$ cm^2. This value is of the same order as the geometric cross section of a Mn^{+2} ion. Even though the cross section of Tb^{+3} luminescent center has not been determined experimentally, the Tb^{+3} ionic radius (0.923Å) is larger than the Mn^{+2} ionic size (0.80Å) and Tb^{+3} forms Tb-F or Tb-O-F complex center. Therefore it is logical to assume that the Tb luminescent center has a larger impact cross-section than a Mn luminescent center.

As shown in figure 6.15, the Ce codoped film shows higher excitation efficiency for both polarities as compared to undoped films. This high excitation efficiency of Ce codoped film is always correlated with a higher threshold voltage. An increased threshold voltage should result in an increased internal phosphor field as shown at figure 6.18.

Higher internal phosphor fields in Ce codoped film will result in a larger fraction of the electrons with energy sufficient to excite the Tb luminescent centers. The increased threshold voltage is attributed to modification of the space charge as discussed below in section 6.4.2.3. This must explain the higher excitation efficiency since Ce codoping would not change the physical excitation cross section for Tb.

In addition to an increase of the average excitation efficiency (figure 6.15), the excitation efficiency for the Al- polarity is larger than for Al+. For ZnS:Mn ACTFEL devices, it has been reported [46] that the excitation efficiency is higher for the Al-polarity than for the Al+ polarity. This anisotropy was attributed to a non-uniform distribution of active Mn^{+2} centers. However in ZnS:Tb films, the Tb ion distribution is uniform as shown figure 6.8. Therefore, the asymmetry of excitation efficiency may result from the different crystallinity of the phosphor layer or different energy state distribution adjacent to the ITO versus Al electrodes. As shown at figure 6.4, the crystallinity of phosphor layer at the beginning of growth is relatively poor because of random nucleation on the surface. It would therefore be reasonable to postulate that electrons injected from the ATO/phosphor interface exhibit more scattering than electrons injected at the phosphor/metal electrode interface. Therefore, the higher excitation efficiency for the Al- polarity is attributed to better crystallinity of the phosphor layer at the top electrode.

6.4.1.2.2 Outcoupling efficiency

The outcoupling efficiency is the probability that emitted photons will escape the film stack in the direction of viewer. Outcoupling efficiency decreases as the internal

reflection of photons at the top and bottom interfaces increases. Internal reflection is described by the difference and absolute values of the index of refraction of the phosphor and the dielectric layer, as well as the interface roughness (see section 2.3.5). Outcoupling efficiency can be improved by reducing the index of refraction of the phosphor layer, which is normally much larger than the index of the insulating layer. Internal reflection may also be reduced by increased interface roughness. The index of refraction is a material constant. It is assumed that the index of refraction of the phosphor and insulator layer are constant for all films in this study, and is independent of doping and codoping.

With respect to interface roughness, it will be present at the phosphor/insulator, insulator/glass substrate, and glass/air interfaces. However, the glass/air interface is constant and insulators such as Al_2O_3 (n=1.63) or SiO_2 (n=1.46) are better matches to the index of glass (n=1.53). Therefore, variability in internal reflection is most affected by the phosphor/insulator interface. The phosphor surface roughness was measured directly by AFM (atomic force microscopy) as shown in figure 6.6. The surface roughness of uncodoped and Ce codoped films is almost the same for as deposited and annealed films (500°C for 60 minutes). Therefore, the data show that Ce codoping in ZnS:TbOF film does not increase surface roughness and the outcoupling efficiency.

6.4.1.2.3 Radiative efficiency

The excited luminescent centers (Tb^{+3} ion or its' complex in ZnS:TbOF) may relax from the excited state by radiatively or nonradiatively processes. Benoit et al. [126] reported that when the decay is normalized to its maximum value, the integrated intensity

of emission decay is equal to the relative radiative efficiency. The radiative efficiency

was calculated for each polarity by normalizing the maximum brightness and integrating

the plot of luminescence intensity versus time. Figure 6.26 shows the EL emission decay

curve normalized for the Al+ polarity at 20V above the threshold voltage. As shown in

figure 6.26, Ce codoping causes a great difference in the radiative efficiency. The results

are summarized at table 6.7. The Ce codoping increased the radiative efficiency for Al+

and Al- polarities by ≈ 88% and 173%, respectively. The average improvement in the

radiative efficiency is ≈ 130%. Therefore, it can be concluded that better radiative

efficiency is the main contribution from Ce codoping for improved brightness and

efficiency.

Table 6.7 Relative radiative efficiency of Ce codoped film compared to uncodoped
ZnS:TbOF films.

Device	Polarity	Relative luminous efficiency (%)
Ce codoped film compared to uncodoped film	Al +	188 %
	Al -	273 %

The time resolved EL emission intensity from Ce codoped ZnS:Tb films can be

described by two different exponential functions, rather than a single exponential, as

discussed for figure 6.27. The first exponential function fits from time zero to 20μs from

the start of excitation voltage pulse. Over this time, the EL emission shows very fast

decay with a time constant of about 5 μsec (figure 6.27), independent of whether the

films are Ce codoped or uncodoped. This initial fast decay prevents describing the kinetics of de-excitation by a first order process. This fast initial decay has been attributed to a high population of excited states leading to rapid diffusion of excited state energy allowing enhanced non-radiative relaxation [127]. Uncodoped films with an Al-polarity shows nearly ideal first order exponential decays after this fast initial decay. However, as shown in figure 6.28, the decay of Ce codoped films are much slower as compared to the uncodoped films after the fast initial decay. Table 6.8 shows the decay time constants of uncodoped and Ce codoped film for both polarities according to the time after the start of the excitation pulse. From table 6.8, the Ce codoping results in a significant increase in the decay time constant. At 0.5 ms after the excitation pulse, the decay time constant of Ce codoped films is 1.85 – 2.1 ms, compared to 0.55 – 0.84 ms for uncodoped film. However, at 4 ms after the excitation pulse, the decay time constant of the Ce codoped film is 0.59 – 0.63 ms which is close to the 0.54 ms of uncodoped film. Therefore, it can be concluded that Ce codoping increases the radiative efficiency. However, the increase of radiative efficiency is time dependent. At short times for Ce codoping films, the emission decay time is much larger than at long times. This improved radiative emission efficiency is attributed to the Tb^{+3} luminescent center because the emission spectrum of the Ce codoped film is exactly the same as uncodoped film (see figure 6.9).

Table 6.8 The decay time constants of uncodoped and Ce codoped films for both polarities versus time after excitation pulse.

Polarity	Device	Decay time constant (ms) at various times after the start of the excitation pulse		
		0.5 ms	2 ms	4 ms
Al +	Uncodoped	0.84	0.55	-
	Ce codoped	2.1	1.15	0.63
Al -	Uncodoped	0.54	0.54	-
	Ce codoped	1.85	1.06	0.59

A possible mechanism that can improve the emission efficiency is energy transfer between the Ce levels and the Tb centers. Energy transfer between the Ce^{+3} and Tb^{+3} has been reported. Also the higher emitting levels such as $^5D_3$ of Tb^{+3} may transfer their energies to neighboring ions of the same species by the following cross-relaxation:

$$^5D_3 (Tb^{+3}) + {}^7F_6 (Tb^{+3}) \rightarrow {}^5D_4 (Tb^{+3}) + {}^7F_0 (Tb^{+3})$$
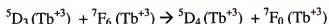
6.4.1.3 Energy transfer between the Ce^{+3} and Tb^{+3}

The excited state of a luminescent center can transfer its energy to another luminescent center of the same species in the ground state when they are located close to each other. They can also transfer energy between different luminescent centers when they have closely matched energy level. The energy transfer between the Ce^{+3} and Tb^{+3} ions has been reported in the green lamp phosphor such as $CeMaAl_{11}O_{19}$-Tb and (La, Ce)PO_4-Tb.
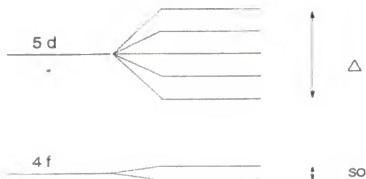
Figure 6.31 The simplified energy level scheme of Ce^{+3} ion $(4f^1)$ [31].

The Ce^{+3} ion $(4f^1)$ has a $4f \rightarrow 5d$ energy transition which is parity and spin-allowed. Therefore, the decay time of the Ce^{+3} emission is 10^{-7} to -10^{-8} s, which is the shortest amongst the lanthanide ions. Figure 6.31 shows the simplified energy level scheme of Ce^{+3} ion [31]. The $4f^1$ ground state yields two level, $^2F_{5/2}$ and $^2F_{7/2}$ by spin orbit coupling. The $5d^1$ configuration is split by the crystal field into 2 to 5 discrete levels. The energy levels of the split $5d^1$ states strongly depend on the structure of the crystal field of the host crystal. Therefore, the emission from the Ce^{+3} ion varies over the range of ultraviolet or blue to green and red depending on the crystal field of the host materials. Figure 6.32 shows the energies of the $5d$ excited level of Ce^{+3} in various crystals. Even though the energy level of Ce^{+3} ion in ZnS host material has not been reported, it is reasonable to assume that the $5d^1$ excited state have a pretty broad energy band covering blue and green region based on the properties of Ce^{+3} in other similar host materials. Therefore, the energy transfer mechanism from Ce^{+3} to Tb^{+3} in ZnS is suggested to be as shown in figure 6.33.
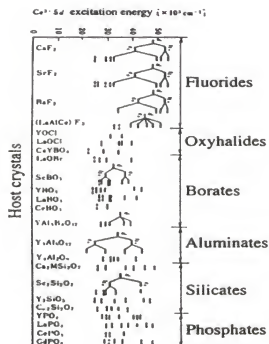
Figure 6.32 Energies of $5d$ excited levels of Ce^{+3} in various host crystals [41].
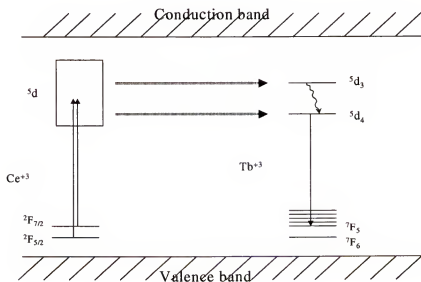
Figure 6.33 Possible energy transfer mechanism from Ce^{+3} to Tb^{+3} in ZnS host materials.

As shown in figure 6.33, there are two possible transfer paths from Ce^{+3} to Tb^{+3} ion. One is that the energy from the excited state of Ce^{+3} ion excites the Tb^{+3} ion from the ground state to the $^5d_3$ state, and this $^5d_3$ state relaxes to the $^5d_4$ state, which recombines radiatively to the ground state. The second possible path is for the excited state energy of Ce^{+3} to transfers directly to the $^5d_4$ state of Tb^{+3} ion and subsequently radiatively decay to the ground state. However, two factors that limit the rate of transfer from the Ce^{+3} to the Tb^{+3} ion are the concentration of Ce^{+3} ion and the tens of nanoseconds decay time of Ce^{+3}. The codoping concentration of Ce^{+3} ion is ~10ppm, and such small concentrations would not normally supply sufficient transfer centers to support the improvement in radiative luminescence efficiency. However, if the energy transfer rate between the Ce^{+3} to Tb^{+3} ion is equal to or shorter than the decay time of Ce^{+3}, then more than one thousand excitations and transfers may take place during the 30μs voltage pulse. If the energy transfer rate is very fast, transfer at the end of the pulse will not lead to the slow Tb^{+3} decay at short times. On the other hand, if the energy transfer between the Ce^{+3} to Tb^{+3} ion is to the $^5d_3$ state of Tb^{+3} which must then relax to the $^5d_4$ state, this could be a slow process and the non-linear decay curves could result.

<u>6.4.2 Ag + Cu Codoped ZnS:TbOF Film</u>

For the Ag, Cu and Ag + Cu codoped ZnS:TbOF film, the same analysis can be applied as for Ce codoped ZnS:TbOF. As shown in figure 6.2, the brightness of Ag or Cu doped ZnS:TbOF ACTFEL device decreases as the concentrations of codopants increases. However, Ag + Cu codoped film show a big increase in brightness and threshold voltage as shown at figure 6.1c. Even though the brightness of Ag + Cu

codoped film increased significantly after annealing (from 47 cd/m^2 for uncodoped film to 67 cd/m^2 for Ag + Cu codoped film at B$_{20}$), the total efficiency of Ag + Cu codoped film did not improve significantly as shown at table 6.4. Possible mechanisms for brightness improvement without improved efficiency for Ag + Cu codoped films will be discussed below, considering each factor in section 6.4.1.

6.4.2.1 The amount of conduction charge

The amount of conduction charge of Cu, Ag and Ag + Cu codoped film was evaluated from Q-V and Q$_{int}$-F$_p$ curves and results were summarized at table 6.9. The external conduction charge measured from the Q-V data and the internal conduction charge measured from Q$_{int}$-F$_p$ data both show decrease upon Ag, Cu and Ag + Cu codoping, even though the decreases are within 10% of the total conduction charges. Therefore, it is concluded that codoping of Ag, Cu or Ag + Cu gives small decreases of conduction charge decrease.

Table 6.9 The external and internal charge evaluated from the Q-V and Q_{int}-F_p analysis
for uncodoped and Ag, Cu and Ag+Cu codoped film.

		Uncodoped (V_{10})	Ag+Cu codoped (V_{10})	Uncodoped (V_{40})	Ag codoped (V_{40})	Cu codoped (V_{40})
External ($\mu C/cm^2$)	Al +	1.1	1.0	3.8	3.6	3.5
	Al -	0.7	0.6	4.2	4.0	4.0
Internal ($\mu C/cm^2$)	Al +	1.5	1.1	4.3	3.7	3.7
	Al -	0.9	0.9	4.3	4.1	-

6.4.2.2 Device efficiency

The overall device efficiency of the Ag, Cu and Ag + Cu codoped films were

given in table 6.4. As discussed at section 6.3.10.1, the total efficiency of the Ag + Cu

codoped film is not improved significantly. If the brightness improvement is

accompanied by the increase in the consumed power density, the total efficiency does not

increase. The efficiency factors discussed at 6.4.1 are separate consideration of each

physical steps-of excitation, relaxation, and optical outcoupling. The effects of the Ag +

Cu codoping on each of these steps will be discussed.

6.4.2.2.1 Excitation efficiency

The excitation efficiency is reported at figure 6.21. The early burnout of the Ag +

Cu codoped film makes exact comparison of Ag + Cu codoped films versus uncodoped

film difficult, and require restricting this comparison to below V_{10} or below because of

burnout. Over this range, the amount of conduction charge is small leading to high noise levels in the excitation efficiency. These observations not withstanding, the average increase in excitation efficiency at V_{10} for Al+ polarity and at V_{15} for Al- polarity is $\approx 100\%$ as compared to uncodoped films. This improvement is attributed to the increased threshold voltage for codoped films. Increased threshold voltage is likely to result from reduced band bending as a result of less positive space charge [40]. The mechanism will be discussed in detail in section 6.4.2.3.

6.4.2.2.2 Outcoupling efficiency

As discussed at section 6.4.2.2.2, the two major factors that affect the outcoupling efficiency are index of refraction and the interface roughness. The index of refraction can be assumed to be the same for uncodoped and Ag, Cu, or Ag + Cu codoped ZnS:TbOF films. Indeed, data in table 6.2 and figure 6.6 show that the Ag + Cu codoped film has a rougher surfaces, (RMS of 12 –15 nm) versus an uncodoped, Ag codoped, or Cu codoped ZnS:TbOF film (RMS of 6 –10 nm). Even though quantitative values are not available, the rougher surface Ag + Cu codoped films will give higher outcoupling efficiency.

6.4.2.2.3 Radiative efficiency

Determination of the radiative efficiency was described in section 6.4.2.1.3. The accumulated emission intensity is given in table 6.10, and the ratio of this integrated emission indicates the relative radiative efficiency. Even though there are some variations according to polarity of the Al electrode on Ag, Cu and Ag+Cu codoped films, the average radiative efficiency of these codoped films are almost the same and larger than

the uncodoped films. This improved efficiency is attributed to the modification of point

defects by Ag^{+1} or Cu^{+1} ion. These +1 valence ions can reduce the concentration of Zn

vacancies by substituting on the Zn^{+2} site to meet charge balance requirements.

Table 6.10 The radiative efficiency for uncodoped, Ag, Cu and Ag+Cu codoped film (at 10V above threshold voltage).

	Al + (a.u)	Al - (a.u)	Average (a.u)
Ag + Cu codoped	1.18	1.16	1.17
Ag codoped	1.38	1.00	1.19
Cu codoped	1.44	0.89	1.17
uncodoped	0.88	0.63	0.76

Even though the radiative efficiency is improved, the degree is the same as that of

Ag or Cu codoped film. Therefore, the relatively high brightness of Ag+Cu codoped film

compared to Ag or Cu codoped film is mainly attributed to excitation efficiency and

outcoupling efficiency improvement, not to changes in radiative efficiencies.

6.4.2.3 The mechanisms to improve the brightness of Ag + Cu codoped film

In summary, Cu, Ag and Ag + Cu codoping show several common changes

compared to uncodoped films. That is

1. Decrease in conduction charge

2. Decrease in space charge

3. Improvement in radiation efficiency.

However, Ag+Cu codoped film shows additional significant change compared to Ag or Cu codoped films, such as

1. Much more suppression of space charge as compared to Ag or Cu singly codoped films

2. Further increase of surface roughness.

Based on these results, it is concluded that the combination of Ag^{+1} and Cu^{+1} better reduces the Zn vacancy concentrations caused by the Tb^{+3} ion incorporation, and this reduction results in less space charge. Actually, the point defect structure of Ag or Cu codoped ZnS:TbOF film is quite complicated because several different charged elements, such as Ag^{+1}, Tb^{+3} and F^1 are involved. However, if Tb^{+3} ion is not fully charge compensated by F^1 ions, Zn vacancies will be required for charge neutrality. Zn vacancies can be compensated by +1 ions as shown schematically at figure 6.34.
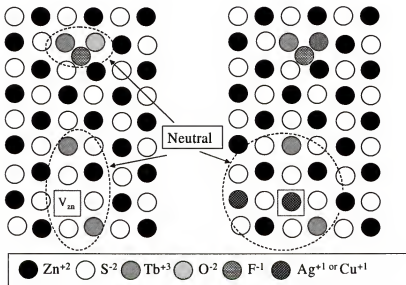
Figure 6.34 Schematic representation of point defect modification in ZnS:TbOF codoped by Cu^{+1} or Ag^{+1}.

(a)   (b)
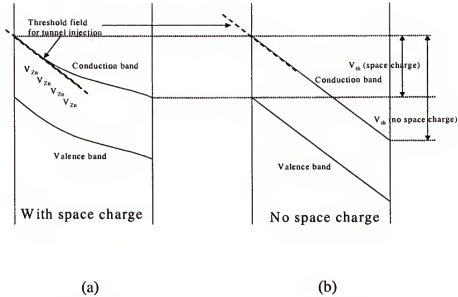
Figure 6.35 Modification of energy band diagram by reducing positive space charge [40].

This modified point charge mechanism can explain the Ag, Cu and Ag + Cu codoping effects. First, the decrease of the conduction charge can be explained by the Ag^{+1} or Cu^{+1} ions acting as acceptor in ZnS. Even though the degree of the conduction charge is ~5%, the decrease is consistent for Ag or Cu codoped film. Secondly, the positive space charge from V_{zn} modifies the electronic band in the phosphor layer as shown in figure 6.35 [40]. The reduced C-V overshoot shown in figure 6.22b, 6.23b and 6.25 support that the space charge is reduced by codoping with Ag, Cu or Ag + Cu.

Modification of the electronic band bending by space charge has been discussed by many authors [128-132]. The effect is shown in figure 6.35 (J. Lewis [40]). Reduced space charge leads to less band bending and higher threshold voltages. According to this model, it is assumed that the band bending near the interface required for electron

tunneling is the same for uncodoped films and Ag, Cu and Ag+Cu codoped films. In this case, the space charge acts to bend the electronic band as shown at 6.35a. With high positive space charge trapping, the electric field at the cathode side increases compared to the anode side. Because of the strong band bending near the cathode, electrons tunnel and light is emitted at lower applied voltages. If space charge caused by Zn vacancies is compensated by codoped Ag^{+1} or Cu^{+1}, band bending will be reduced or totally suppressed as shown at figure 6.35b. To reach the threshold voltage for tunnel emission of electron, the average field across the phosphor layer must be larger leading to higher threshold voltages. These larger electric fields increase the excitation efficiency of the ACTFEL device because the excitation efficiency is defined as the number of excited centers per transferred electrons. The higher electron acceleration caused by these fields increase the excitation efficiency.

The improved radiative efficiency of Ag, Cu and Ag + Cu codoped films compared to uncodoped films can also be explained by the point defect modification. Reduction of the Zn vacancy concentration by codoping of Ag^{+1} or Cu^{+1} in the ZnS:Tb ACTFEL phosphor could reduce the non-radiative recombination rates.

However, Ag + Cu codoped films show significant increase in brightness and threshold voltage even compared to Ag or Cu singly codoped films. These changes are accompanied by nearly total suppression of space charge and by increased surface roughness. The data in figure 6.25 shows no C-V overshoot, consistent with near elimination of space charge in the ZnS:Tb phosphor layer. The more effective suppression of space charge by Ag + Cu codoping than the Ag or Cu singly codoping may be attributed to improved solubility or reduced segregation of Ag^{+1} and Cu^{+1} in Ag +

Cu codoped films. The Ag codoped film shows leaky turn-on behavior as discussed in section 6.3.1, and this leaky turn-on behavior is attributed to Ag^{+1} segregation to the grain boundary. Even Cu^{+1} doped film shows relatively leaky turn-on compared to Ag + Cu codoped films. As shown in figure 6.4, Cu codoped films annealed at 850°C for 5 minutes show precipitates that are assumed to be a Cu rich sulfide. That indicates that even annealing at 500°C for 60 minutes can result in segregation of Cu ion to the grain boundaries which can be responsible for leaky turn-on behavior. However, Ag + Cu codoped film does not show this kind of leaky turn-on behavior. That suggests that Ag + Cu codoping suppresses Ag and Cu segregation.

Another significant change by the Ag + Cu codoping is the increased surface roughness. The surface roughness in Ag + Cu codoped films significantly larger from the AFM image. This rough surface may also be responsible for the early burnout of Ag + Cu codoped film.

6.5 Summary

ZnS:TbOF ACTFEL devices were codoped with Ag, Cu, Ag + Cu, Ce by R.F. magnetron sputtering using separate Ag, Cu and Ce_2O_3 targets. In the best case, Ce codoping increased the brightness at 40V above threshold voltage (V_{40}) to 144 cd/m^2 compared to 86 cd/m^2 of uncoped ZnS:TbOF film after annealing at 500°C for 60 minutes. This brightness improvement (67%) is attributed to increased radiative efficiency. At V_{20}, the radiative efficiency of Ce codoped films is improved $\approx$ 130%. The non-linear exponential decay of electroluminescent emission for Ce codoped films is attributed to energy transfer from Ce^{+3} to Tb^{+3} luminescent centers. The excitation

efficiency is also increased due to reduced space charge. However, the increase of excitation efficiency is relatively small compared to the increase of radiative efficiency, which is the dominant mechanism for improvement by Ce codoping.

Ag + Cu codoped ZnS:TbOF thin film phosphor also showed increased brightness at 20V above threshold (B_{20} of 67 cd/m^2 compared to 55 cd/m^2 for uncodoped ZnS:TbOF film after annealing at 500°C for 60 minutes). The increased brightness for Cu +Ag codoped ZnS:TbOF film is attributed to increased surface roughness and improved excitation efficiency caused by reduced space charge as compared to single Ag^{+1} or Cu^{+1} codoping.

CHAPTER 7
CONCLUSIONS

The effects of deposition parameters and codoping on electroluminescent ZnS:Tb,F film deposited by R. F. magnetron sputtering were investigated to improve the electroluminescence (EL) brightness and efficiency.

Thin film of ZnS:TbOF were R.F. plasma magnetron sputter deposited from either a single pressed powder ZnS:TbOF (1.5 mole % of Tb) target, or two separate sputter sources consisting of a CVD grown, undoped ZnS target and a TbOF pressed powder target. The films deposited from the two separate ZnS and TbOF targets exhibited poor crystallinity and smaller grain size versus films from a single target, due to negative ion resputtering (NIR) effects. Thin films deposited from the single ZnS:TbOF target showed much higher brightness ($B_{40} = 89$ cd/m^2) than thin films deposited from two separate ZnS and TbOF targets ($B_{40} = 44$ cd/m^2). A concentration of 3~4 mole % Tb^{+3} resulted in the best brightness and the emission spectrum was not significantly changed with increasing Tb^{+3} concentrations.

ZnS:TbOF ACTFEL devices were also sputter-deposited from a single pressed powder ZnS:TbOF (1.5 mole % of Tb) target using an Ar + He mixed gas (He gas concentration was changed from 0% to 70%). The films were annealed at 500°C for 600 minutes under a N$_2$ gas atmosphere. From X-ray diffraction, the FWHM of the cubic (111)/hexagonal (0002) plane in deposited films decreased from 0.55° (for Ar 100%) to 0.39° (for Ar 30 % + He 70 %) and the growth rate decreased about 25% as the He ratio increases from 0 to 70%. In spite of the improved crystallinity as indicated by the

decreased FWHM, the brightness of the device decreases from 64 cd/m^2 for a pure Ar atmosphere to 45-54 cd/m^2 at 60-70% He gas concentrations. This brightness decrease is attributed to an increased dielectric constant (from 12 for pure Ar to 17 at 70 % He) and decreased RMS surface roughness (from 6.7 nm for pure Ar to 4.3 nm at 70 % He) of the deposited film.

To investigate the effects of oxygen incorporation in ZnS:Tb,F, films were deposited from a ZnS:TbF$_3$ target using an oxygen flow controlled by a leak valve. ZnS:Tb,F films show the best brightness (82 cd/m^2) at 3.6 at. % of oxygen concentration in the deposited film, with a very sharp drop off in brightness from either underdoping (56 cd/m^2 at 2.2 at. % oxygen) or overdoping (42 cd/m^2 at 8.1 at. % oxygen). The conduction charge calculated from charge (Q) versus voltage (V) and the charge (Q) versus time (t) data show that the brightness improvement can be attributed to 24% increase in conduction charge when the oxygen concentration increases from 2.2 at. % to 3.6 at. %. The brightness decreases with oxygen overdoping, which is attributed to both a decreased excitation and a decreased radiative efficiency. The excitation efficiency decreased by 23% while the radiative efficiency decreased by 24% when the oxygen concentration increases from 3.6 at .% to 8.1 at. %.

ZnS:TbOF ACTFEL devices were codoped with Ag, Cu, Ag + Cu and Ce by R.F. magnetron sputtering using separate Ag, Cu and Ce$_2$O$_3$ targets. In the best case, Ce codoping increases the brightness at 40V above threshold voltage (V$_{40}$) to 144 cd/m^2 compared to 86 cd/m^2 for uncodoped ZnS:TbOF film after annealing at 500°C for 60 minutes. This brightness improvement is attributed to an increased radiative efficiency. At V$_{20}$, the radiative efficiency of Ce codoped film is improved ≈ 130% compared to

uncodoped film. The luminescence decay versus time for Ce codoped films was not exponential decay due to energy transfer from Ce^{+3} to Tb^{+3} luminescent centers. The excitation efficiency also increases due to space charge reduction. However, the increase of excitation efficiency is relatively small compared to the increase of radiative efficiency, which is the dominant mechanism for the brightness improvement by Ce codoping.

Ag + Cu codoped ZnS:TbOF thin film phosphors also showed increased brightness at 20V above threshold (B_{20} of 67 cd/m^2 compared to 55 cd/m^2 for uncodoped ZnS:TbOF film after annealing at 500°C for 60 minutes). The increased brightness for Cu +Ag codoped ZnS:TbOF film is attributed to an increased surface roughness and the improved excitation efficiency caused by space charge reduction from Ag^{+1} and Cu^{+1} codoping. In spite of ≈10% decrease in conduction charge by Ag + Cu codoping, the device brightness is improved by increase in excitation efficiency and by a rougher surface (15 nm RMS roughness for Ag + Cu codoped film compared to 6-8 nm for uncodoped, Ag codoped and Cu codoped film after annealing at 500°C for 60 minutes).

LIST OF REFERENCES

1. H. Kobayashi and S. Tanaka, J. SID, 4(3), 157-164 (1996).

2. R. H. Mauch, J. SID, 5(3), 173-178 (1997).

3. P. D. Rack, A. Naman, P. H. Holloway, S. S. Sun and R. T. Tuenge, MRS Bulletin, 21(3), 49-58 (1996).

4. Y. A. Ono, Ann. Rev. Mat. Sci., 27, 283-303 (1997).

5. C. N. King, J. of SID, 4(3), 153-156 (1996).

6. R. Mach and G. O. Mueller, Semicond. Sci. Technol., 6, 305-323 (1991).

7. C. N. King, Mat. Res. Soc. Symp. Proc., 508, 247-258 (1998).

8. P. D. Rack and P. H. Holloway, Materials Science & Engineering, 21(4), 171-219 (1998).

9. C. N. King, J. Vac. Sci. Technol. A, 14(3), 1729-1735, Part 2 (1996).

10. S. Tanaka and H. Kobayashi, The 18th International Display research conference, ASIA DISPLAY '98, 927-932 (1998).

11. R. T. Tuenge, J. SID, 6(1), 57-60 (1998).

12. M. Leskela and L. Niinisto, Materials Chemistry and Physics, 31, 7-11 (1992).

13. K. Okamoto, T. Yoshimi, K. Nakamura, T. Kobayashi, S. Sato and S. Miura, Jpn. J Appl. Phys. Part 1, 28(8), 1378-1384 (1989).

14. A. Mikami, T. Ogura, K. Tanaka, K. Taniguchi and M. Yoshida, J. Appl. Phys., 61(8), 3028-3034 (1987).

15. Y. A. Ono, Electroluminescent Displays, Singapore, World Scientific (1995).

16. H. Guden, R. W. Pohl, Z. F. Physik., 2, 192 (1929).

17. T. Inoguchi, M. Takeda, Y. Kakihara, Y. Nakata and M. Yoshida, Digest of 1974 SID international Symposium, 84 (1974).

18. R. Khormaei, S. Thayer, K. Ping, C. King, G. Dolney, A. Ipri, F. L. Hsueh, R. Stewart, T. Keyser, G. Becker, D. Kagey and M. Spitzer, SID Digest, 137 (1994).

19. P. Bailey, D. Carkner and X. Wu, SID Digest, 484 (1995).

20. P. Balmforth, D. Luke, J. Virginia and D. Carkner, The Extended Abstracts of the 6th International Conference on the Science and Technology of Display Phosphors, 57-60 (2000).

21. M. Godlewski and M. Leskela, Critical Reviews in Solid State and Materials Sciences, 19(4), 199-239 (1994).

22. S. Kobayashi, J. F. Wager and A. Abu-Dayah, EL 92 Proceedings, 234 (1992).

23. R. Mach and G. O. Mueller, J. Crystal Growth, 101, 967-975 (1990).

24. M. Dur, S. Goodnick, S. S. pennathur, J. F. Wager, M. Reigrotzki and R. Redmer, J. Appl. Phys., 83(6), 3176-3185 (1998).

25. E. Bringuier, J. Appl. Phys., 70(8), 4505-4512 (1991).

26. G. A. Baraff, Phys. Rev., 128(6), 2507-2517 (1962).

27. K. Brennan, J. Appl. Phys., 64 (8), 4024-4030 (1988).

28. K. Bhattacharyya, S. M. Goodnick and J. F. Wager, J. Appl. Phys. 73(7), 3390-3395 (1993).

29. E. Bringuier, J. Appl. Phys., 75(9), 4291-4312 (1994).

30. D. C. Krupka, J. Appl. Phys., 43, 476 (1972).

31. G. Blasse, B. C. Grabmaier, Luminescent Materials, Berlin, Springer-Verlag (1994).

32. J. W. Allen, Electroluminescence, Springer Proc. Phys., 38, 10 (1989).

33. S. Tanaka, H. yoshiyama, Y. Mikami, J. Nishiura, S. Ohshio, H. Deguchi and H. Kobayashi, Appl. Phys. Lett., 50, 119 (1987).

34. S. Tanaka, S. Ohshio, J. Nishiura, H. Kawakami, H. Yoshiyama and H. Kobayashi, Appl. Phys. Lett., 52, 2102 (1988).

35. B. S. title, Phys. Rev. Lett., 3, 273 (1959).

36. K. L. Chopra, S. Major and D. K. Pandya, Thin Solid Films, 102, 1 (1983).

37. L. Binet and D. Gourier, J. Solid State Chem., 113, 420-433 (1994).

38. D. Stodika, A. H. Kitai and Z. Huang, SID 00 Digest (2000).

39. S. Poort, D. Cetin, A. Meijerink and G. Blasse, J. Electrochem. Soc., 144(6), 2179-2183 (1997).

40. J. S. Lewis, Ph. D Dissertation, Alternating-current thin film electroluminescence, Materials Science and Engineering, University of Florida (2000).

41. S. Shogeo and M. Y. William, Phosphor Handbook, Boca Raton, CRC Press (1998).

42. S. Tanaka, H. Deguchi, Y. Mikami, M. Shiiki and H. Kobayashi, Digest of 1985 SID international Symposium, 29 (1986).

43. G. Harlognen, K. Harkonen and R. Tornqvist, Digest of 1990 International Symposium, 232 (1990).

44. T. Ogura, A. Mikami, K. Tanaka, K. Taniguchi, M. Yoshida and S. Nakajima, Appl. Phys. Lett., 48, 1570 (1986).

45. Shoichi Matsumoto, Electronic Display Devices, Chichester, John Wiley & Sons (1990).

46. R. Mach, G. O. Mueller, Phys. Stat. Sol. (a), 81, 609-623 (1984).

47. A. Zeinert, P. Benalloul, J. Benoit, C. Barthou, J. Dreyhsig and H. E. Gumlich, J. Appl. Phys., 71(6), 2855-2862 (1992).

48. A. Zeinert, P. Benalloul, C. Barthou, J. Benoit, J. Dreyhsig and H. E. Gumlich, J. Crystal Growth, 117, 1016-1020 (1992).

49. D. H. Smith, J. Lumin., 23, 209 (1981).

50. P. M. Alt, Proc. SID, 25, 123-146 (1984).

51. A. A. Douglas, J. F. Wager, D. C. Morton, J. Koh and C. P. Hogh, J. Appl. Phys., 76, 296 (1993).

52. J. F. Wager and P. D. Keir, Annu. Rev. Mater. Sci., 27, 223-248 (1997).

53. J. C. Hitt, J. P. Bender and J. F. Wager, Critical Reviews in Solid State and Materials Sciences, 25(1), 29-85 (2000).

54. L. V. Pham, J. F. Wager, S. S. Sun, E. Dickey, R. T. Tuenge and C. N. King, SPIE, 2174, 190-199 (1994).

55. C. B. Sawyer and C.H. Tower, Physical Review, 35, 269-273 (1930).

56. Y. O. Ono, H. Kawakami, M. Fuyama and K. Onisawa, Jpn. J. Appl. Phys., 26, 1482 (1987).

57. E. Bringuier, J. Appl. Phys., 66, 1316 (1989).

58. R. C. McArthur, J. D. Davidson, J. F. Wager, I. Khomaei and C. N. King, Appl. Phys. Lett., 56, 1889-1891 (1990).

59. J. D. Davidson, J.F. Wager, R. I. Khormaei, C. N. King and R. Williams, IEEE Transactions on Electron Devices, 39(5), 1122-1128 (1992).

60. J. D. Davidson, J. F. Wager and S. Kobayashi, J. Appl. Phys., 71(8), 4040-4048 (1992).

61. S. Shih, P. D. Keir and J. F. Wager, J. Appl. Phys., 78(9), 5775-5781 (1995).

62. A. Abu-Dayah and J. F. Wager, J. Appl. Phys., 75(7), 3593-3598 (1994).

63. A. Abu-Dayah, S. Kobayashi and J. F. Wager, Appl. Phys. Lett., 62(7), 744-746 (1993).

64. A. Abu-Dayah, J. F. Wager and S. Kobayashi, J. Appl. Phys., 74(9), 5575-5581 (1993).

65. K. Ohmi, S. Inoue, S. Tanaka and H. Kobayashi, Appl. Phys. Lett., 64(5), 3464-3466 (1994).

66. W. M. Ang, S. Pennathur, L. Pham, J. F. Wager, S. M. Goodnick and A. A. Douglas, J. Appl. Phys., 77(6), 2719-2724 (1995).

67. S. Shih, P. D. Keir, J. Hitt and J. F. Wager, Appl. Phys. Lett., 69(13), 1921-1923 (1996).

68. J. C. Hitt, P. D. Keir, J. F. Wager and S. S. Sun, J. Appl. Phys., 83(2), 1141-1145 (1998).

69. P. D. Keir, Ph. D Dissertation, Fabrication and characterization of ACTFEL devices, Electrical and Computer Engineering, Oregon State University (2000).

70. B. A. Baukol, J. C. Hitt, P. D. Keir and J. F. Wager, Appl. Phys. Lett., 76(2), 185-187 (2000).

71. D. Kahng, Appl. Phys. Lett., 13, 210 (1968).

72. J. Ohwaki and O. Kogure, Jpn. J. Appl. Phys., 23(12), 1649-1450 (1984).

73. J. Mita, M. Koizumi, H. Kanno, T. Hayashi, Y. Sekido, I. Abiko and K. Nihei, Jpn. J. Appl. Phys., 26(7), L1205-L1207 (1987).

74. H. Ohnishi, M. Watanabe, R. Yamamoto, T. Okuda and S. Ibuki, Proc. SID, 23(3), 223-227 (1991).

75. Y. J. Lin, Y. K. Su and M. Yokoyama, Appl. Phys. Lett., 65/66, 461-464 (1993).

76. V. S. Khomchenko, Y. F. Kononec, N. A. Vlasenko, R. Mach, G. U. Reinsperger, B. Selle and R. Reetz, J. Crystal Growth, 101, 994-998 (1990).

77. S. H. Su, S. X Chen, M. Yokoyama and Y. K. Su, J. SID, 4/4, 315-318 (1996).

78. K. Hirabayashi, H. Kozawaguchi and B. Tsujiyama, Jpn. J. Appl. Phys., 27(4), 587-591 (1988).

79. W. Kong, J. Fogarty and R. Solanski, Appl. Phys. Lett., 65(6), 670-672 (1994).

80. T. Ogura, A. Mikami, K. Tanaka, K. Taniguchi, M. Yoshida and S. Nakajima, Appl. Phys. Lett., 48(23), 1570-1571 (1986).

81. K. Okamoto and K. Watanabe, Appl. Phys. Lett., 49(10), 578-580 (1986).

82. A. Mikami, T. Ogura, K. Tanaka, K. Taniguchi, M. Yoshida and S. Nakajima, J. Appl. Phys., 61(8), 3027-3034 (1987).

83. J. Mita, M. Koizumi, H. Kanno, T. Hayashi, Y. Sekido, I. Abiko and K. Nihei, Jpn. J. Appl. Phys., 26(5), L558-L560 (1987).

84. K. Streicher, T. K. Plant and J. F. Wager, J. Appl. Phys., 78(3), 2102-2104 (1995).

85. V. Marrello, L. Samuelson and A. Onton, J. Appl. Phys., 52(5), 3590-3599 (1981).

86. A. Mikami, T. Ogura, K. Taniguchi, M. Yoshida and S. Nakajima, J. Limin., 40/41, 784-785 (1988).

87. K. Streicher, T. K. Plant and J. F. Wager, J. Appl. Phys., 78(3), 2101-2104 (1995).

88. J. Ohwaki, H. Kozawaguchi and B. Tsujiyama, Jpn. J. Appl. Phys., 22(1), 65-67, (1983).

89. W. Kong and R. Solanki, J. Appl. Phys., 75(7), 3311-3315 (1994).

90. P. Bailey, D. Carkner and X. Wu, J. Appl. Phys., 81(2), 931-936 (1997).

91. N. Miura, H. Matsumoto and R. Nakano, Jpn. J. Appl. Phys. Part 1, 31(2A), 288-294 (1992).

92. R. Nakano, H. Matsumoto, T. Endo, J. Shimada, N. Sakagami and N. Miura, Jpn. J. Appl. Phys., 27(11), L2103-2104 (1988).

93. D. Hommel, H. Hartmann and J. M. Langer, Phys. Stat. Sol., 81, K199-K203 (1984).

94. K. Okamoto and S. Miura, Appl. Phys. Lett., 49(23), 1596-1598 (1986).

95. K. Okamoto, T. Yoshimi and S. Miura, Appl. Phys. Lett., 53(8), 678-680 (1988).

96. K. Okamoto, T. Yoshimi, K. Nakamura, T. Kobayashi, S. Sato and S. Miura, Jpn. J. Appl. Phys., 28(8), 1378-1384 (1989).

97. B. D. Cullity, Elements of X-ray diffraction, Reading, Addison-Wesley (1978).

98. C. R. Brundle, C. A. Evans Jr., S. Wilson, Encyclopedia of Materials Characterization, Boston, Butterworth-Heinemann (1992).

99. J. M. Blackmore and A.G. Cullis, Thin Solid Films, 199, 321 (1991).

100. K. E. Waldrip, M. R. Davidson, J. H. Lee, B. Pathangey, M. Puga-Lambers, K. S. Jones, P. H. Holloway, S. S. Sun and C. N. King, Display and Imaging, S (suppl), 73 (1999).

101. R. E. honig, j. Appl. Phys., 29, 549 (1958).

102. J. J. Hanak and J. P. Pellicane, J. Vac. Sci. Technol., 13(1), 406 (1976).

103. J. J. Cuomo, R. J. Gambino, J. M. E. Harper, J. D. Kuptsis and J. C. Webber, J. Vac. Sci. Technol., 15(2), 281 (1978).

104. Daniel J. Kester and Russell Messier, J. Mater. Res., 8(8), 1928 (1993).

105. Daniel J. Kester and Russell Messier, J. Mater. Res., 8(8), 1938 (1993).

106. Daniel J. Kester and Russell Messier, J. Vac. Sci. Technol., A4(3), 496 (1986).

107. Mark R. Davidson, Balu Pathangey, Paul H. Holloway, Phillip D. Rack, S. S. Sun and C. N. King, J. of Electronic Materials, 26(11), 1355 (1997).

108. J. M. E. Harper, J. J. Cuome, R. J. Gambono, H. R. Kaufman and R. S. Robonson, J. Vac. Sci. Technol., 15(4), 1597 (1978).

109. H. Xian, P.Benalloul, C.Barthou and J.Benoit, Thin Solid Films, 248, 193-198 (1994).

110. L. I. Maissel and R. Glang, Handbook of Thin Film Technology, New York, McGraw-Hill (1970).

111. L.C. Feldmann, J. W. Mayer, Fundamentals of Surface and Thin Film Analysis, New York, North-Holland (1986).

112. K. G. Cho, D. Kumar, S. L. Jones, D. G. Lee, P. H. Holloway, and R. K. Singh, J. Electrochem. Soc. 145, 3456 (1998).

113. A. S. Toporets, Sov. J. Opt. Technol. 46(1), 35-48 (1979).

114. Sean L. Jones, D. Kumar, K. G. Cho, R. Singh, Paul H. Holloway, Display 19, 151-167 (1999).

115. D. Their, R. Wengert, J. Electrochem. Soc.:Solid-State Science and Technology, 132(10), 2507-2510 (1985).

116. H. E. Bennett and J. O. Porteus, J. Opt. Soc. Am. 51(2), 123-129 (1961).

117. A. S. Toporets, Sov. J. Opt. Technol. 46(1), 35-48 (1979).

118. I. Schnitzer, E. Yablonovitch, C. Caneau, T. J. Gmitter, and A. Scherer, Appl. Phys. Lett. 63(16), 2174-2176 (1993).

119. M. Noma, S. Hosomi, S. H. Sohn and Y. Hamakawa, J. Crystal Growth, 117, 1030-1034 (1992).

120. J. Van Den Bossche, K. A. Neyts, P. De Visschere, D. Corlatan, H. Pauwels, R. Vercaemst, L. Fiermans, D. Poelman, R. L. Van Meirhaeghe, W. H. Laflere and F. Cardon, Physica Status Solidi (A) Applied Research, 146(2), k67-k70 (1994).

121. C. W. Wang, T. J. Sheu, Y. K. Su and M. Yokoyama, Proceedings of the International Semiconductor Conference, 175-178 (1996).

122. K. E. Waldrip, J. S. Lewis, Q. Zhai, M. Puga-Lambers, M. R. Davidson, P. H. Holloway and S. S. Sun, J. Appl. Phys., 89(3), 1664-1670 (2001).

123. T. C. Jones, W. Park, and C. J. Summers, Appl. Phys. Lett., 75 (16), 2398 (1999).

124. N. Hashimoto, Y. Takada, K. sato and S. Ibuki, J. Lumin., 48/49, 893-897 (1991).

125. D. Ravichandran, R. Roy, P. Ravindranathan and W. B. White, J. of Am. Ceram. Soc., 82(4), 1082 (1999).

126. K. Lott, M. Raukas, A. Vishnjakov, A. Grebennik, J. Crystal Growth, 197, 489 (1999).

127. C. H. Seager and D. R. Tallant, Proc. of 20th Intl. Display Research Conference, 382-385 (2000).

128. K. A. Neyts, D. Corlatan, P. De Visschere and J. Van Bossche, J. Appl. Phys., 75(10), 5339-5346 (1994).

129. A. A. Douglas, J. F. Wager, D. C. Morton, J. B. Koh and C. P. Hogh, J. Appl. Phys., 73(1), 296-299 (1993).

130. K. A. Neyts and E. Soininen, IEEE Transactions on Electron Devices, 42(6), 1086-1092 (1995).

131. K. Ohmi, K. Ishitani, S. Tanaka and H. Kobayashi, Appl. Phys. Lett., 67(7), 944-946 (1995).

132. J. Beniot, P. Benalloul, C. Barthou, S. Casette and J. C. Soret, Physica Status Solidi (a), 122, 427-438 (1990).

133. P. D. Keir, W. M. Ang and J. F. Wager, J. Appl. Phys., 78(1), 4668-4680 (1995).

BIOGRAPHICAL SKETCH

Jongpyo Kim was born on January 22, 1968, in Teagu, Korea, and grew up there. In March, 1986, he was admitted to the Department of Inorganic Materials Engineering of Seoul National University. He received a B.S degree in February 1990 and joined the graduate school at the same University. For his master's degree, he worked on SiC single crystal growth and also worked as a teaching assistant at the Inter-University Semiconductor Research Center (ISRC). After receiving his M.S degree in February 1992, he worked at Research and Development Center of Oriental Chemical Industry in Inchon, Korea, studying piezoelectric materials in the electronic materials research laboratory. He developed piezoelectric components such as resonators and filters, infrared sensors, piezoelectric transformers, etc. Also he studied on Cu metallization of ceramic substrates by electroless- and electro-plating methods and patterning by photolithography. In August 1997, he received admission to the University of Florida, Department of Materials Science and Engineering. In the spring of 1998, he joined Dr. Holloway's research group and studied electroluminescent thin film phosphors. In December 2001, he completed his Ph.D dissertation under the supervision of Dr. Holloway.

I certify that I have read this study and that in my opinion it conforms to acceptable standards of scholarly presentation and is fully adequate, in scope and quality, as a dissertation for the degree of Doctor of Philosophy.

Paul H. Holloway, Chairman
Professor of Materials Science and
Engineering

I certify that I have read this study and that in my opinion it conforms to acceptable standards of scholarly presentation and is fully adequate, in scope and quality, as a dissertation for the degree of Doctor of Philosophy.
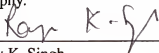
Ralf E. Hummel
Professor of Materials Science and
Engineering

I certify that I have read this study and that in my opinion it conforms to acceptable standards of scholarly presentation and is fully adequate, in scope and quality, as a dissertation for the degree of Doctor of Philosophy.

Cammy R. Abernathy
Professor of Materials Science and
Engineering

I certify that I have read this study and that in my opinion it conforms to acceptable standards of scholarly presentation and is fully adequate, in scope and quality, as a dissertation for the degree of Doctor of Philosophy.

Rajiv K. Singh
Professor of Materials Science and
Engineering

I certify that I have read this study and that in my opinion it conforms to acceptable standards of scholarly presentation and is fully adequate, in scope and quality, as a dissertation for the degree of Doctor of Philosophy.

Timothy J. Anderson
Professor of Chemical Engineering

This dissertation was submitted to the Graduate Faculty of the College of Engineering and to the Graduate School and was accepted as partial fulfillment of the requirements for the degree of Doctor of Philosophy.

December 2001

Pramod P. Khargonekar
Dean, College of Engineering

Winfred M. Phillips
Dean, Graduate School